High-level data analysis in the COMAP intensity mapping experiment

Jowita Borowska

Thesis submitted for the degree of
Master of Science in Astronomy

Institute of Theoretical Astrophysics
University of Oslo

1st June 2021

Cover Image: Open Source Photo by Philippe Donn from www.pexels.com.

Abstract

The CO Mapping Array Pathfinder (COMAP) is an intensity mapping experiment targeting the emission from rotational lines of carbon monoxide, redshifted to the frequency range of $26-34$ GHz. In this first phase of a planned longer-term program, the primary science goal is the detection of CO(1-0) signal, aiming to constrain its power spectrum at the Epoch of Galaxy Assembly ($z = 2.4 - 3.4$). It is, therefore, crucial to devise an efficient method of extracting this signal from the obtained three-dimensional line intensity maps. We also need to make sure that any experimental systematic, giving rise to undesirable signs of excess power, is sufficiently suppressed. In this thesis, we develop an effective approach addressing both of these demands and apply it to analyze the first year of gathered data.

We present how the low-level analysis pipeline converts raw data provided by the telescope into filtered and calibrated temperature sky maps. Then, we design the Feed-feed Pseudo CROSS Spectrum (FPXS) method, the foundation of the high-level data analysis in COMAP. FPXS is used as a principal tool for inferring the signal spectrum from the maps and assessing the quality of the current data set. Moreover, by employing accurate signal simulations, we study and quantify the impact of different effects on the measured signal. The resulting transfer functions are applied to derived spectra in order to correct the bias present in the maps. Specifically, we consider the instrumental beam smoothing the signal on small angular scales, the choice of the spectral resolution of the maps, affecting small scales in the line-of-sight dimension, as well as the attenuation of the signal on large scales, introduced by various procedures performed during the low-level data analysis. We find that the combination of these phenomena limits the sensitivity of the experiment to $k \approx 0.05 - 0.5$ Mpc^{-1} (the clustering component of the power spectrum).

In the considered range of cosmological scales, the results associated with constant elevation scans (CES) indicate that we are effectively suppressing the sources of systematics below the current level of white noise and that the measurement uncertainties integrate down as expected from the radiometer equation. Already at this point (before accumulating enough data to reach a suitable detection sensitivity), the upper limit derived from CES results is excluding the brightest models for the CO signal at 95% confidence. Nevertheless, the data obtained by scanning the sky according to the Lissajous pattern exhibit clear signs of excess power caused by residual systematics. We suspect that these arise due to effects correlated with the pointing of the telescope, requiring a more complicated treatment prior to using Lissajous data in the scientific analysis.

Acknowledgments

First of all, I would like to thank my supervisors, Ingunn and Hans Kristian, for all the help and support, and especially for giving me the possibility of joining the CMB&CO group to work on such an interesting project alongside many great scientists. I would also like to thank Håvard, whose expertise has helped me tremendously with many aspects of this work over the past year. Thank you for your invaluable help, amazing knowledge, and patience. In addition, I would like to thank Duncan, for many very good and useful comments on the thesis, as well as Nils, Jonas, Marie, Maren, and the rest of the fantastic scientists that are part of the COMAP collaboration, for all the help and information you have given me. I would also like to thank everybody that has helped me on my academic path and enabled me to gain more relevant experience. Thank you!

Finally, I would like to thank my friends and family. Thank you, Piotr, for the endless love and support. Thank you, Justyna, Natalia, Jessie, Christina, Ida, Ørjan, Barathy, and Silvia, for always being there for me when I needed a break. And thanks to my sweet Fado, who has brightened up my home office days.

Jowita Borowska

Preamble

The knowledge about the origin and evolution of the Universe has been gradually expanded along with technological advances throughout the history of mankind. From simple telescopes to current-day complex space missions, the field of cosmology has undergone a dramatic development. The great progress in this area would not be possible without the studies of the cosmic microwave background (CMB) and galaxy surveys, gathering an unprecedented wealth of information. The emerging technique of line intensity mapping (LIM) is a complementary tool, addressing some of the important topics that remain unexplored. In this approach, all the integrated emission of spectral lines is measured over large volumes of the Universe. Therefore, the LIM is not biased towards the sources that are bright enough to be resolved individually (like the galaxy surveys) and can access even faint contributions at high redshifts. It is thus able to provide an insight into the periods in the history of the Universe that we know very little of, including the formation of first stars and galaxies or the Epoch of Reionization.

One of the major line intensity mapping experiments is the CO Mapping Array Pathfinder (COMAP), operating between 26 and 34 GHz. It targets primarily the ground state rotational transition of carbon monoxide, CO(1-0), redshifted from the Epoch of Galaxy Assembly ($z = 2.4 - 3.4$), but the frequency range covers also a weaker contribution of CO(2-1) signal from the Epoch of Reionization ($z = 6 - 8$). The observational data have been gathered for over a year now, employing a 10.4 m telescope with 19 detector chains (feeds), located at the Owens Valley Radio Observatory (OVRO) in California, USA. The main science goals associated with this first phase of a longer-term CO mapping program include detecting the CO signal or constraining its power spectrum, as well as placing limits on the CO luminosity function, the molecular gas abundance in the Universe, and the star formation history.

At these early stages of the experiment, we focus on the data selection and effective filtering methods, designed to suppress the contributions of correlated noise and experimental systematics. It is therefore extremely important to assess the final quality of the data set, which should ideally be consistent with random Gaussian noise that integrates down with the observational time until the experiment reaches a suitable detection sensitivity. Moreover, it is crucial to efficiently extract the CO signal from the line intensity maps and study how the data analysis procedures and instrumental effects impact this measurement. In this thesis, we will address all of these issues, developing a high-level data analysis pipeline, based on splitting the data from corresponding feeds with respect to different statistics and cross-correlating the resulting three-dimensional temperature sky maps – the Feed-feed Pseudo CROSS Spectrum (FPXS) method.

Chapter 1 will be devoted to describing the history of astronomy, highlighting some of the most important scientific breakthroughs leading to the birth of modern-day cosmology. We will also present our current state of knowledge about the origin and evolution of the Universe and showcase the experimental endeavors aiming to study different probes. In Chapter 2, we will focus on the field of line intensity mapping, especially its scientific payoff, goals, and targets. After providing such thorough background, we will proceed to Chapter 3, where we describe the COMAP experiment – the instrument, observation strategy, and low-level data analysis pipeline, producing the calibrated sky maps out of raw detector readouts. In Chapter 4, we will explain the methodology associated with the high-level data analysis, developed in this thesis to infer the signal power spectrum out of maps. We will also demonstrate how to quantify the effects altering the signal measurement (transfer functions) using the CO signal simulations. The outcomes connected to these effects will be shown in Chapter 5 and the main scientific results obtained through the FPXS approach will be discussed in Chapter 6. Finally, we will draw conclusions and present the outlook on future work in Chapter 7.

Contents

List of Figures

Part I

Introduction to Cosmology and COMAP

Chapter 1

Scientific Background

Our perception of the Universe and how it evolved

Throughout the history of humankind people have been fascinated by the wonders of night sky - gazing at the stars, seeking the truth about their place in the Universe. Archaeological findings around the world indicate that astronomy was one of the earliest natural sciences to emerge [1]. From ancient cultures observing the positions of celestial bodies to modern-day precision cosmology, our understanding of the Universe has been advanced tremendously by generations of scientists. Standing on the shoulders of giants, we are now able to comprehend the vastness of the Universe and describe it with physical models governing its evolution. As stated by Robert Millikan, the Nobel laureate in Physics (1923), astronomy portrays: "A Universe that knows no caprice, a Universe that behaves in a knowable and predictable way, a Universe that can be counted on."[2]

In this introductory chapter, we will outline some of the most important breakthroughs in the history of astronomy, leading to the birth of modern cosmology. We will also present our current perception of the Universe, supported by the range of experiments acquiring observational data using different probes.

1.1 A Brief History of Astronomy and Cosmology

Unless otherwise referenced, this section is based on *The Universe Today* by Carlos Martins [3] and *A Brief History of Astronomy and Astrophysics* by Kenneth Lang [4].

1.1.1 Universe limited to the Solar System

The origins of observational astronomy reach far back into the cradle of civilization – Mesopotamia – the area where many ancient cultures flourished, including Babylonians and Assyrians. One of the earliest astronomical catalogs, known as the Mul.apin, was developed already in the Assyrian period around 1000 BCE. Since the celestial objects were seen as the embodiment of deities at that time, the astronomical observations were conducted solely by priests. Through recording the periodic motions of heavenly bodies, they gradually gained enough information to be able to predict their future positions on

the sky and foresee astronomical phenomena like eclipses. However, these predictions were purely empirical. Babylonians could calculate the time of certain events, without seeking an explanation or a cause of their occurrence. This had not changed until much later, in ancient Greece. We can therefore state that the birth of astronomy took place in Babylon, yet the earliest ideas associated with the emergence of cosmology stem from Greek philosophers.

The development of philosophy began in the sixth century BCE, raising questions about the origin and the structure of the Universe, as well as the laws that govern the behavior of celestial objects. Excluding divine influences from their explanations of reality, philosophers from the Milesian school, such as Thales, are regarded to be the first scientists. Geometry was no longer used only for practical purposes (like building ships or dividing land), but became an important tool in establishing how the Universe was constructed. The world view had been evolving with more and more contributions to science made by philosophers like Pythagoras (the first one to postulate that Earth was a sphere), Heraclitus ("everything flows"), Plato, and Aristotle. The first model reproducing the observations accurately, including the retrograde motion of Mars, was that of Ptolemy, developed in the second century CE. It was a geocentric model, where all the planets were moving with constant speed around a small circle (epicycle), with a center that was revolving around the Earth along a larger circle (deferent). The predictions of apparent planetary motions based on the Ptolemaic system were precise enough to be still in use over a thousand years later.

The revolution came with Nicolaus Copernicus, who set the Earth, together with five other planets visible with an unaided eye, in a uniform circular motion around a stationary Sun. Although multiple circles were not necessary in his model to explain, for instance, the retrograde motion of Mars, they had to be adopted for better agreement with observations. Copernicus' outlook on cosmology was described in the book *On the revolutions of the celestial orbs*, published in 1543. Nevertheless, without any definitive tests or arguments in favor of the heliocentric theory, it was not widely accepted until the seventeenth century. At that time, the truth about the Universe and its higher complexity became more apparent with the invention of the telescope. Having built his own instrument, Galileo was able to see previously unresolved features on the Moon and stars that constitute the Milky Way. He also made some remarkable discoveries, observing the four largest Jovian moons and phases of Venus (in 1610). Meanwhile, a Danish astronomer, Tycho Brahe, had obtained very precise measurements of planetary motions, especially detailed for the changing position of Mars. Johannes Kepler succeeded in understanding these observations after nearly ten years, formulating his first two laws. He realized that Mars moved along an elliptical orbit with the Sun at one focus and the line between the planet and the Sun swept out equal areas in equal times. A few years later, Kepler extended his studies to other known planets with his third law of planetary motion, described in *Harmony of the World* (1619). It expressed the proportionality between the squares of the orbital periods of the planets and the cubes of their mean distances to the Sun. According to Kepler, planetary motions were governed by the Sun. Although he did not discover the true nature of this force, his work laid the foundations for Newton's theory of universal gravitation.

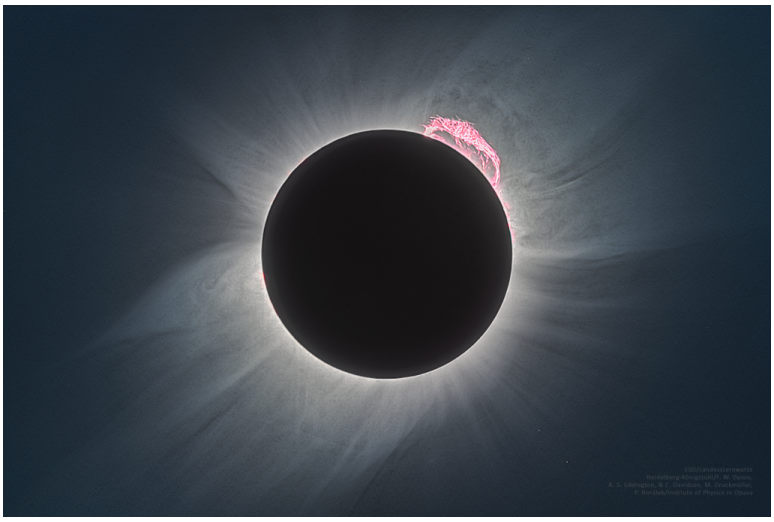

Figure 1.1: Restoration of the picture taken in May 1919. It shows starlight bent under the influence of the Sun's gravity during the total eclipse, as predicted by Einstein's General Theory of Relativity. Credit: ESO/Landessternwarte Heidelberg-Königstuhl/F. W. Dyson, A. S. Eddington and C. Davidson [5].

1.1.2 Discovering the true nature of gravity

Isaac Newton was a very religious man, but it did not have a significant impact on the progress of his work within astronomy. He thought that there was an overlap between cosmology and theology, aiming to understand God – the Creator of the ordered Universe – through science. Newton constructed the first known reflecting telescope, studied the theory of light and colors, developed the laws of motion and gravity. His famous *Mathematical Principles of Natural Philosophy*, more commonly known as *Principia*, from 1687 (first edition) is considered to be one of the greatest and most important scientific publications in history. It consists of three books. The concepts of mass, force, and quantities of motion are introduced in the first book, extending in the second one to the motion in the presence of a resisting medium. The last book, entitled *On the System of the World*, describes the theory of universal gravitation and its consequences for astronomy. Along with the laws of motion, it explains the movement of objects anywhere in the Universe. The force of gravity acts between all bodies, strengthening with their masses and decreasing with the square of the distance between them. It governs the motion of planets around the Sun and keeps the Moon in orbit around the Earth. The validity of Newton's theory was ultimately verified much later. After detecting Uranus in 1781, its path was observed to deviate from the expected one. This indicated the existence of an unknown planet beyond Uranus, whose position was mathematically predicted based on the theory of gravitation, leading to the discovery of Neptune in 1846. However, the triumph of Newton's theory was not the final step in unraveling the truth about the nature of gravity. In 1859 a French astronomer, Urbain Le Verrier,

was the first to describe an unexpected finding – the position of planet Mercury, whose orbit is not a closed ellipse, shifts from the exact starting point after one revolution around the Sun by a slightly larger factor than could be explained with the Newtonian approach. This mystery was unresolved until 1915 when Einstein explained how gravity truly works in his *General Theory of Relativity*.

Newton's laws required amending. He mostly succeeded in explaining how cosmic objects moved under the influence of gravity but not why they moved. It was Albert Einstein who postulated that gravity was not a force but the distortion of spacetime in presence of massive objects. Matter curves spacetime and spacetime controls the motion of matter. The difference between Newton's and Einstein's description of gravity became apparent near very massive bodies so that the observed precession of Mercury's perihelion was finally fully understood. Moreover, Einstein expected that the curvature of spacetime around the Sun would deflect the path of starlight by twice as much as it had been predicted by Newton. This theory was tested during a total solar eclipse in 1919 (see Figure 1.1), making Einstein famous almost overnight. Another prediction of the general theory of relativity was the existence of gravitational waves – the invisible ripples in the fabric of spacetime that stretch and compress the space as they pass by. This subtle effect was indirectly observed for the first time in 1974 by two radio astronomers, Russell A. Hulse and Joseph H. Taylor. They discovered a binary system composed of a neutron star and a pulsar, which were approaching each other at the rate corresponding to the loss of energy if it was carried away by gravitational waves. Nevertheless, they were directly detected only in 2015, by the Laser Interferometer Gravitational-Wave Observatory (LIGO), measuring signals from two black holes in the process of merging (more about that in Section 1.3.2).

1.1.3 The expanding Universe and its beginning

In *Cosmological Considerations of the General Theory of Relativity* from 1917 [6], Einstein presented a model of the Universe that had closed spatial geometry, was static and eternal. In order to achieve the static solution and remain consistent with his theory, it was essential to introduce an additional term to the equations, counteracting the gravitational attraction of matter – the cosmological constant. Shortly after, the Dutch astronomer Willem de Sitter found an alternate solution, applying Einstein's theory of gravity to the Universe with no matter, where the cosmological constant drives the expansion. Eventually, the model that accurately described the real Universe, incorporating both the matter component and the expansion, was introduced by Georges Lemaître in 1927. He combined Einstein's theory with the observed redshifts of spiral nebulae, concluding that they are moving away from one another not due to their motion through the static space, but rather due to the expansion of space itself [7]. Lemaître's work had not been widely noticed until 1929 when Hubble published his famous results. Having used Cepheid variable stars to precisely measure distances of spiral nebulae, he found their relation to radial velocities (provided mostly by Vesto M. Slipher), which also had been theoretically derived by Lemaître two years earlier.

The more distant a galaxy is, the faster it is receding away from us, following the Hubble-Lemaître law,

$$v = H_0 D, \tag{1.1}$$

where v is the velocity of a galaxy at distance D and H_0 is the Hubble constant (value of the Hubble parameter, H, today). This discovery became clear observational evidence for the expansion of the Universe. For that reason, Einstein discarded the concept of cosmological constant and later collaborated with Willem de Sitter to create a model of the expanding Universe without this term.

By inverting Hubble's original estimate of the expansion rate of the Universe, assuming it had always been constant, it could be shown that the Universe started to expand around 1.8 billion years ago (which is known as the Hubble time, H_0^{-1}). This would mean that the Universe was younger than Earth, whose age had been estimated by radioactive decay techniques. The problem lay, however, in a rather poor estimate of the Hubble constant, which was more accurately determined in 1958 by Allan Sandage, correcting the Hubble time to be approximately 13 billion years (as opposed to around 14 billion years, known currently). It became natural to ask what the Universe had expanded from. A backward extrapolation suggested that in the beginning it was much smaller and denser – possibly with "all the energy of the Universe packed in a few or even a unique quantum", as described by Lemaître in 1931 [8]. The important work contributing to a similar vision of Universe's birth was made by George Gamow and his colleagues. They studied the origin of light chemical elements, concluding that they had to be created in the very hot and compact early Universe. The temperature of its radiation would decrease as the Universe expanded, dropping to about 5 kelvins, predicted by Ralph A. Alpher and Robert C. Herman [9] (later measured to be closer to 3 K [10]). Nevertheless, there existed different theories, including the Steady State model, proposed by Herman Bondi, Thomas Gold, and Fred Hoyle in 1948. It described the unchanging Universe with no beginning, where the expansion of space was compensated for by the endless creation of new matter. The definitive reason for refuting this idea came in 1965 with the discovery of the relic radiation, not predicted by the Steady State theory.

The detection of the cosmic microwave background (CMB) became a strong observational proof in favor of the Big Bang theory. It was an unanticipated discovery, made during measurements of extragalactic radio sources at the Bell Telephone Laboratories. Arno A. Penzias and Robert W. Wilson noticed an excess contribution to the antenna temperature from an unknown noise source, regardless of where they pointed their instrument. It was equally strong in all directions and did not depend on the time of the year. After ruling out many possible causes of interference to the telescope, they came across a cosmological explanation due to Robert H. Dicke, who studied the Big Bang theory and was looking for the evidence in its support. The observations of the CMB radiation became more and more precise, with three generations of space-based experiments (see Figure 1.5) dedicated to increasing our knowledge about the early history of the Universe. These studies are complemented by multiple galaxy surveys, aiming to characterize the origin and evolution of galaxies (more on that in Section 1.3.1).

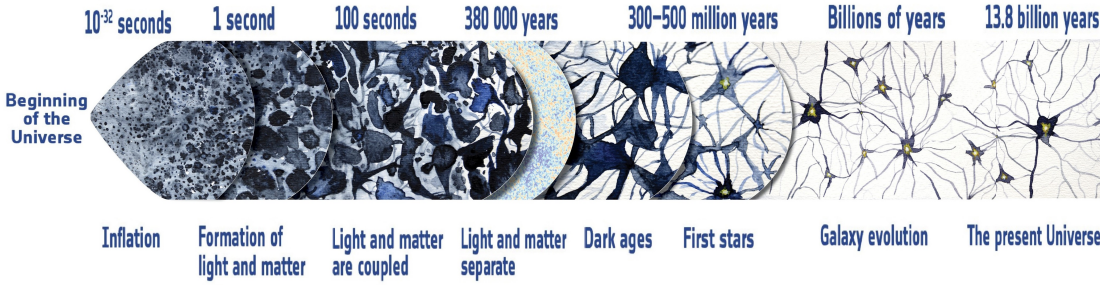

Figure 1.2: Timeline of periods in the history of the Universe. Adapted from ESA [11].

1.2 The known Universe

In the previous section, we outlined the history of cosmology as a science, describing how some important ideas and discoveries led to our current state of understating the Universe. Now, we will present the history of the Universe itself, following our knowledge and conjectures about what has happened from right after the very beginning until present times. The timeline, marking the most important periods chronologically, is shown in Figure 1.2.

1.2.1 When it all began

Unfortunately, the known laws of gravity are not without limitations, making them unable to describe the beginning and the very early Universe, when quantum effects must be taken into account. The absolute threshold beyond which they cannot be applied anymore is called the Planck scale and corresponds to energies higher than $\sim 10^{19}$ GeV or the time before the first 10^{-43} seconds after the Big Bang. When the energy was around three orders of magnitude lower, the conditions were still so extreme that, according to Grand Unified Theory (GUT), the three types of interactions – electromagnetic, weak, strong – merged into one [12].

Around that time, the period of inflation began, lasting from about 10^{-34} to 10^{-32} seconds [13]. It was the phase of very rapid growth, during which the Universe expanded exponentially for over 60 e-folds (factor of $e^{60} \approx 10^{26}$) [14]. Although the inflationary model has not been fully verified, it is successful in explaining the origin of microscopic density fluctuations that later grew to large-scale structures. It also predicts some important cosmological observations, solving three issues with the traditional Big Bang theory. The first one, called the horizon problem, is associated with the fact that the particle horizon at recombination had an angular size of only about one degree, making the causal contact between regions separated by more than that impossible. Then, what is the reason behind the isotropy of the CMB across the entire sky, displaying only small temperature fluctuations ($\Delta T/T \sim 10^{-5}$)? Another question relates to the flatness problem – why is the curvature density parameter, Ω_K, so 'fine-tuned'? To match the current observations of Ω_K being close to zero (implying that the Universe is spatially flat), it must have been even closer to zero at earlier times, with the extreme

precision of 10^{-60} at the Planck scale [12, 13]. Lastly, according to the Big Bang theory, we should be able to observe a high abundance of stable *magnetic monopoles*, created very early in the history of the Universe. Nevertheless, these have not been detected, so even if they do exist, their number is very small [15].

1.2.2 When matter formed and decoupled from radiation

Following the period of inflation, the Universe continued to expand at a slower rate and cool. Initially, there only existed a primordial plasma with all the constituents in equilibrium. Through the process of baryogenesis and leptogenesis, there was a higher abundance of particles (protons, neutrons, electrons) than anti-particles (anti-protons, anti-neutrons, positrons), with exception of neutrinos and anti-neutrinos to which this asymmetry did not apply. Around one second after the Big Bang, the thermal energy of the Universe was close to 1 MeV. In such conditions, neutrinos could decouple from the primordial plasma to stream freely as the Cosmic Neutrino Background (CNB). Roughly half a minute later, the reaction creating photons out of electron-positron pair and the other way around, $e^- + e^+ \leftrightarrow \gamma + \gamma$, became irreversible. Annihilation took over, removing all the positrons but leaving some electrons (one electron per proton), because of the initial imbalance due to leptogenesis [12, 16].

A couple of minutes after the Big Bang, the Universe cooled to around 0.1 MeV and neutrons were able to fuse with protons, forming light atomic nuclei. This period is called the Big Bang Nucleosynthesis (BBN). The vast majority of neutrons became bound first in deuterium, then later transformed into helium. At the end of BBN, helium nuclei constituted about 25% of the baryonic mass in the Universe and hydrogen nuclei (protons) around 75%, in addition to some small fraction of deuterium, helium-3, and lithium-7. This quantitative representation was theoretically predicted by the Big Bang model and subsequently confirmed by observations, which provided yet another evidence in favor of the theory [13].

The Universe was opaque at that time. Since all the atoms were fully ionized, the photons were frequently Thomson scattered by free electrons. As the expansion and cooling continued, the free electrons could combine with free nuclei, forming neutral atoms in the process called recombination. This happened around 380,000 years after the Big Bang, when the temperature dropped to $\sim$ 3000 K. The Universe became transparent to photons, which could decouple from baryonic matter and travel freely from the last-scattering surface until today, being redshifted to the microwave range of the electromagnetic spectrum and observed as the cosmic microwave background (CMB) across the whole sky [13, 14].

1.2.3 When the first stars and galaxies were born

After the recombination, the Universe was filled with the blackbody radiation of the CMB. However, for the temperature around 3000 K, the peak of emission lay in infrared, which only got redshifted as the temperature decreased. Without a significant source

of visible light, the Universe entered the Dark Age, remaining in darkness for millions of years to come. This changed with the formation of first stars (Cosmic Dawn) [17].

According to the cosmological principle, the Universe is spatially homogeneous and isotropic on large scales. Density inhomogeneities are, however, very evident on smaller scales, with massive clusters of galaxies being about 200 times denser than the average in the Universe. The amplitudes of density fluctuations were not that large in the beginning, as indicated by the observed temperature anisotropies in the CMB, which are of order $\sim 10^{-5}$. The density contrast increased over time, due to the stronger gravitational attraction of overdense regions [13]. When masses of dark matter halos became sufficiently large (above the so-called Jeans mass), the baryonic gas could fall into the potential wells created by halos. Additionally, there had to be an efficient cooling mechanism so that the gas could collapse to even higher densities, enabling the subsequent formation of stars and galaxies. The stars composed of this primordial, metal-free gas are called population III stars. They had a big impact on their environment, emitting energetic photons that were able to ionize surrounding hydrogen. These bubbles of ionized gas, centered on halos containing the first stars, were the beginning of the Epoch of Reionization. After some of the population III stars ended their lives, exploding as supernovae, baryonic gas from the hosting halos was blown away, suppressing further star formation. At the same time, the metals produced in the supernova explosions were ejected into the intergalactic medium (IGM), providing a new ingredient for cooling (besides atomic hydrogen) during the collapse of even more massive halos, where the next generation of stars could form. New regions of ionized hydrogen expanded and started to overlap, eventually filling the whole volume of the Universe and marking the end of the reionization period [13, 17]. The Universe continued to expand, as new stars and galaxies formed and evolved to resemble what we can observe today.

1.3 How can we observe the Universe?

Our current state of knowledge about the Universe was achieved through theoretical predictions, consistent with numerous observations that have been conducted using different probes. In this section, we will describe important aspects of observational cosmology and present some selected experiments, aiming to detect electromagnetic radiation, gravitational waves, or neutrinos. The focus will be put on CMB experiments and redshift surveys of galaxies, leaving the complementary line intensity mapping, with its techniques and experimental landscape, to be the topic of the next chapter.

1.3.1 Electromagnetic Radiation

Most of the main methods, which we can use to gather information about the interactions between cosmological objects and the evolution of the Universe, are connected to observations of electromagnetic radiation. These are conducted over the entire range of wavelengths, from highly energetic gamma rays ($\lambda < 10^{-12}$ m) to radio waves ($\lambda > 10^{-1}$ m) [16].

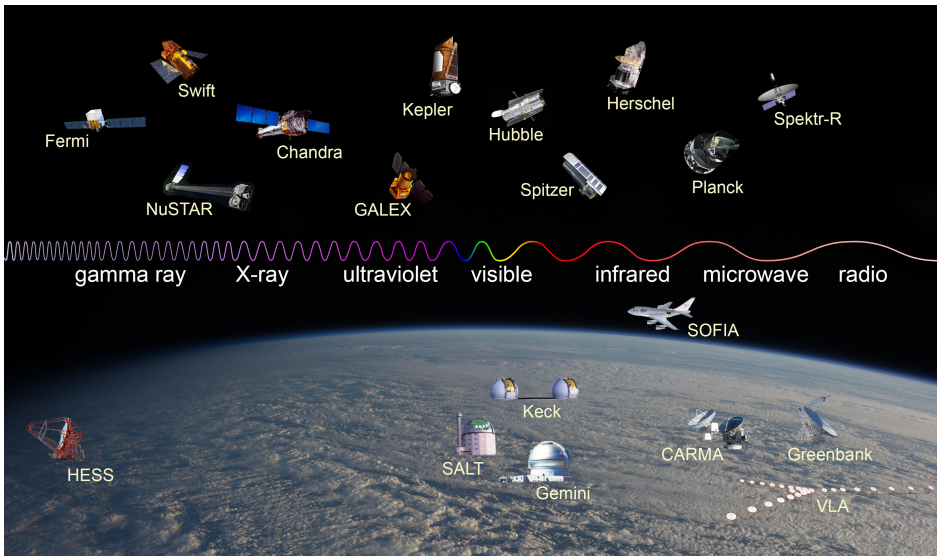

Figure 1.3: Selection of ground-based and space-based experiments operating at different frequencies across the electromagnetic spectrum [18].

Naturally, such a big span of energies requires different construction of telescopes and detectors. Another issue is the opacity of Earth's atmosphere, allowing only some range of electromagnetic spectrum to get through, including visible light and radio waves. This limits the extent of ground-based observations. However, there are indirect measures. For instance, in the case of gamma-ray astronomy, telescopes detect Cherenkov radiation. This is the effect that can be observed when gamma rays enter the Earth's atmosphere and pass their energy on, creating the cascade of particles traveling at speeds faster than the phase velocity of light in air [19]. Nevertheless, in many cases, it is essential or more beneficial to conduct observations from space. Satellite missions are able to avoid limitations due to interference from the atmosphere or light pollution and provide lots of valuable data about different components of the Universe. Figure 1.3 shows some of the experiments observing at different frequencies, placed above or below the associated part of the electromagnetic spectrum.

When the source of radiation is moving with respect to the observer, the wavelength of emitted light, λ_{emit}, is different from the wavelength of observed light, λ_{obs}. This change can be quantified with redshift, z, defined as

$$1 + z \equiv \frac{\lambda_{\text{obs}}}{\lambda_{\text{emit}}}. \tag{1.2}$$

We can observe a negative redshift (blueshift) when the source is approaching, so that $\lambda_{\text{obs}} < \lambda_{\text{emit}}$. In the context of cosmological observations, this applies to rather close sources, such as the Andromeda galaxy. Its peculiar motion overcomes the effect of Universe's expansion, which causes more distant galaxies to move away from us, shifting their light towards longer wavelengths as a consequence (positive redshift) [12].

While space expands, the distance between us and these remote sources increases. This implies that earlier in the history of the Universe we were closer than presently – the physical distance evolves with time and is proportional to the scale factor, a, defined to have the value equal to one today [14]. Its relation to cosmological redshift follows

$$1 + z = \frac{a(t_0)}{a(t_{\text{emit}})} = \frac{1}{a(t_{\text{emit}})}, \tag{1.3}$$

which means that we can relate higher redshifts to photons emitted further back in the past (when $a < 1$) and use it as a reference to the timeline of the Universe. The CMB radiation, originating from the Epoch of Recombination, probes $z \sim 1100$, whereas galaxy surveys are associated with more recent times and mostly limited to redshifts $z \lesssim 1$. However, we know very little about the periods in between, like the Epoch of Reionization. This can change with new insights, provided by the emergence of line intensity mapping [20].

Redshift surveys of galaxies

Small density fluctuations, created during the period of inflation, evolved into the large-scale structures that we can observe today. Therefore, the spatial galaxy distribution, tracing the underlying dark matter, is not uniform. There is a clear correlation between the positions of galaxies as they form groups and clusters, which can be seen in Figure 1.4. It is thus important to quantitatively study these objects and map their three-dimensional distribution on the sky. In order to do this, a galaxy redshift survey can be performed – either photometric or spectroscopic, depending on the method applied to establish redshifts.

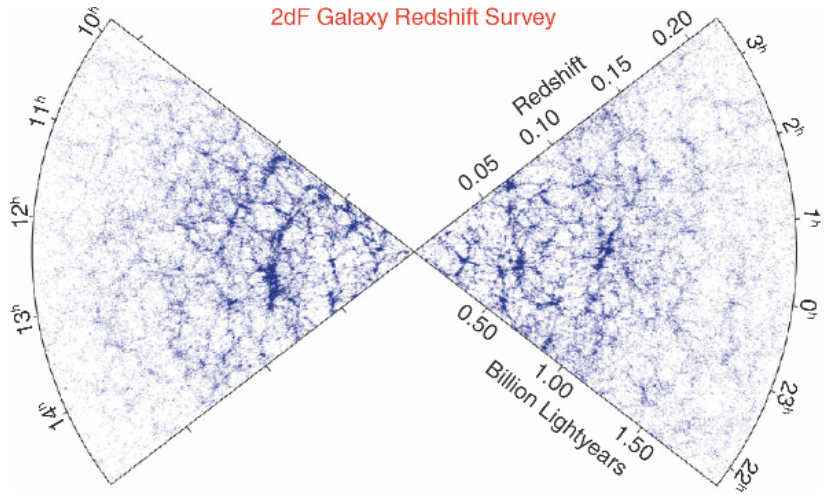

Figure 1.4: Distribution of more than 230 000 galaxies with redshift measurements from the two-degree-Field Galaxy Redshift Survey (2dFGRS). Credit: M. Colless and the 2dFGRS Team [21]

In both cases, the initial stages of an experiment are similar. The first step includes the selection of fields on the sky to examine in the survey. Next, within these two-dimensional patches on the sphere, we need to choose the objects for which a third coordinate will be determined through redshift measurements. Most often the parameter taken into account is brightness so that only sources above a certain threshold are recorded [13]. Thereafter, redshifts can be estimated. As already mentioned, there are two ways to do this.

The first technique is based on observing spectra, with their absorption and emission lines. The wavelength position of these spectral lines is then compared to the spectra of objects with known composition, studied in a laboratory setting. The formula from Equation 1.2 can be used in order to determine redshift. This approach is very accurate, but also costly and time-consuming. All sources must be observed for a sufficiently long time to gather enough light and achieve a high signal-to-noise ratio. Nevertheless, in some cases the lack of clear spectral features can hinder the process of classifying the lines, making such redshift estimates unreliable. We can use another method, which is faster but generally less precise. In the photometric approach, we do not rely on spectrum measurements. Instead, the intensity is recorded, using different filters. For every source, the information from all the frequency bands is then combined, resulting in a very low-resolution spectrum. This can be used for identifying the redshift, for instance through comparison of the broad-band features with some templates [22, 23].

Having measured the two spatial positions of sources on the sky along with the redshift estimates, we need to establish the associated physical distances in order to map the three-dimensional galaxy distribution. For very small redshifts, $z \ll 1$, we can calculate coordinates along the line of sight combining the Hubble law (Equation 1.1) with the Doppler formula, $v \approx zc$ [13]. The process is, however, more complicated in the case of higher redshifts. We will describe the approach we use in the COMAP experiment in this regard in the second part of the thesis (Section 4.3.1).

One of the examples of spectroscopic redshift surveys is the 2 degree Field Galaxy Redshift Survey (2dFGRS), whose results are shown in Figure 1.4. It was carried out between 1997 and 2002, using the Anglo-Australian Telescope, and obtained redshifts for over 230 thousand galaxies, covering an area of about 1500 deg^2. Data from the survey have been used for addressing many problems within cosmology and galaxy formation. This includes, for instance, measuring the power spectrum of galaxy clustering, providing a new upper limit on the total neutrino mass, characterizing the galaxy luminosity function, or determining the values of some important cosmological parameters (in combination with CMB observations) [21].

CMB

It was crucial to conduct more detailed observations of the cosmic microwave background after its discovery in 1965. Especially important became determining whether CMB had a thermal blackbody spectrum (confirming the hot Big Bang theory). Another topic was looking for anisotropies, which should be present in the CMB if today's large-scale structures evolved from tiny primordial density fluctuations. For many years, these

searches were restricted to only detecting the dipole anisotropy (due to our relative motion with respect to the surface of last scattering), which was already found in 1969 by Edward Conklin. Soon after, more experiments followed, introducing new upper limits also on smaller angular scales. Due to interference from Earth's atmosphere, the best precision of measurement could be achieved from space. The first space mission to study CMB was Soviet Relikt-1, launched on board the Prognoz 9 satellite in 1983. Results (including, for instance, constraining the quadrupole) were made public in early 1992, but because of high uncertainty and only one observed frequency (37 GHz) are not mentioned very often [24]. On the other hand, a world-renowned announcement came only a couple of months later, reporting the measurements taken by the Cosmic Background Explorer (COBE).

COBE, launched in 1989, was the first satellite of NASA dedicated to cosmology. It was equipped with three instruments: the Diffuse Infrared Background Experiment (DIRBE), the Differential Microwave Radiometer (DMR), and the Far Infrared Absolute Spectrophotometer (FIRAS). The mission turned out to be a big success, with each instrument making very important contributions to cosmology. FIRAS conducted a precise measurement of the CMB radiation across the whole sky in the frequency range 30 GHz to 2910 GHz, comparing it to a blackbody. It confirmed the hot Big Bang theory, indicating that the CMB spectrum indeed resembles unprecedentedly well the emission of a nearly perfect blackbody with a temperature of 2.725 ± 0.002 K. DMR was designed to detect and measure power differences between two directions in the sky, using horn antennas with 7° fields of view and operating at three different frequencies: 31.5, 53, and 90 GHz. The results revealed anisotropies in the CMB across all observed angular scales, which had a great impact on studies of the early Universe and the structure formation, enabling fast development of theoretical work in these fields.

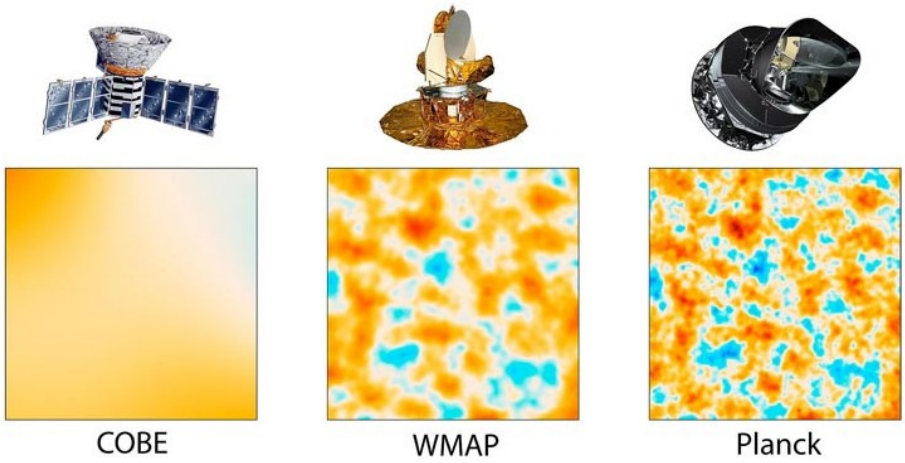

Figure 1.5: Comparison of angular resolution between three space-based CMB experiments. Illustration shows the satellites and 10 deg^2 patches of all-sky maps from COBE-DMR, WMAP, and Planck. Credit: NASA/JPL-Caltech/ESA [25]

The third instrument – DIRBE – was searching for the diffuse cosmic infrared background (CIB). This background radiation consists of emission from numerous objects, like protogalaxies and galaxies, aggregated throughout cosmic history, stretching far back to the time when these sources initially started to form. In addition to redshift due to the expansion of the Universe, dust particles absorb and re-emit the light, so that it is eventually observed in the infrared part of the electromagnetic spectrum. There are many other local contributions to the sky brightness at these wavelengths, making the observations of pure CIB component very challenging. DIRBE carried out measurements in the range from 1.25 to 240 μm, first detecting CIB in the two longest wavelength bands (140 and 240 μm). The experiment obtained a set of brightness maps across the whole sky, providing a unique insight into the role of dust and stellar processes as Universe evolved [10, 26].

The unprecedented richness of cosmological data from COBE motivated further exploration of the cosmic microwave background. The next all-sky experiment was NASA's Wilkinson Microwave Anisotropy Probe (WMAP), launched in 2001. It observed at five frequencies (22, 30, 40, 60, and 90 GHz), had a much better angular resolution (from $\sim 0.23^\circ$ to 0.93°, depending on frequency) compared to COBE-DMR ($\sim 7^\circ$) and took also measurements of polarization. The WMAP mission heralded the onset of precision cosmology and yielded an enormous scientific payoff with its accurate observations of CMB anisotropy. This included putting constraints on cosmological parameters, which contributed to establishing the standard model of cosmology with the spatially flat Universe, dominated by dark energy (71.4%) and dark matter (24%), known as the ΛCDM model [13, 27].

The third generation of space-based experiments measuring anisotropies in the CMB came with ESA's satellite launched in 2009, called Planck. This time the observations were conducted in nine frequency bands, spanning from 30 to 857 GHz, by the Low-Frequency Instrument (LFI) and the High-Frequency Instrument (HFI). Such a wide frequency range proved to be especially important in observing foregrounds contaminating CMB. For the lowest frequencies, these effects include synchrotron radiation, free-free radiation, and emission from spinning dust, whereas at the highest frequencies the main foreground comes from thermal dust emission (mostly in our galaxy, but the CIB is also treated as a part of this component in the Planck analysis). The angular resolution was further improved compared to previous CMB satellite missions, as can be seen in Figure1.5, achieving $\sim 5'$ for the highest frequency bands. After completing many full-sky surveys (HFI scanned the entire sky five times and LFI eight), Planck gathered data that determined the power spectrum of CMB temperature anisotropies with remarkable precision up to the highest multipoles ($\ell \sim 2500$). It put even more stringent constraints on six parameters associated with the ΛCDM model (measuring five of them to better than 1%) and also examined possible deviations from this model. Moreover, it studied gravitational lensing that affects CMB photons and provided polarization power spectra. These measurements were challenging since the polarization signal is much weaker than the temperature signal and the instrumental calibration becomes more difficult [13, 28].

1.3.2 Gravitational Waves

Another way of gaining knowledge about the Universe, particularly about how gravity works, is through gravitational waves. Their existence was predicted by the General Theory of Relativity already in 1915, but the direct observation was made only a hundred years later [29], which we have already mentioned in Section 1.1.2. The first detected signal (GW150914) was generated by the merger of two black holes with masses 36 $M_\odot$ and 29 $M_\odot$, that created a 62 $M_\odot$ black hole, emitting the energy of mass difference (3 $M_\odot c^2$) in the form of gravitational waves. The discovery was made by the Laser Interferometer Gravitational Wave Observatory (LIGO), which operates at two locations in USA – Livingston, Louisiana and Hanford, Washington. The signal was registered by both detectors, with an offset of about 10 ms due to the distance of 3000 km between the two sites. The instruments used by LIGO are Michelson interferometers, with layout illustrated in Figure 1.6 (a). Such a device consists of a laser, producing a monochromatic beam of light that gets separated into two 4 km perpendicular arms by the beam splitter. The beams get reflected back and forth by mirrors (test masses) suspended at the ends of arms. The light travels the exact same distance along both arms and eventually gets combined again, resulting in destructive interference. However, a gravitational wave passing through the instrument induces a relative difference between the length of arms, depending on its strength (so-called gravitational-wave strain). As a result, the combined beams produce an interference pattern, which is registered by the photodetector. Typically, the effective length-change is three orders of magnitude smaller than the diameter of a proton, so an instrument has to be very sensitive in order to make a detection. The data obtained from the experiment may then be compared to

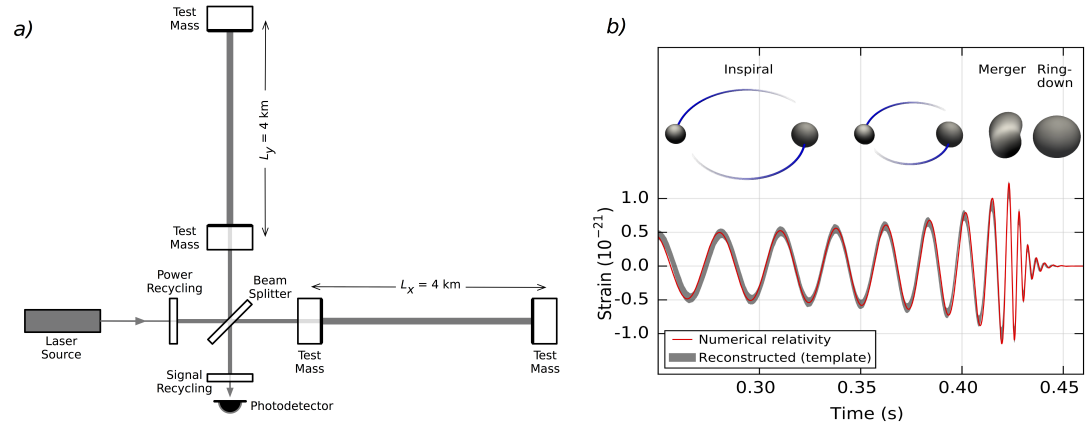

Figure 1.6: a) Schematic diagram of Michelson interferometer used to detect gravitational waves. b) First detected GW signal from a binary black hole merger (GW150914) – three stages of the process, together with gravitational-wave strain results obtained by LIGO-Hanford (grey) compared to theoretically predicted waveform (red). Adapted from LIGO/Virgo [29].

theoretical predictions from general relativity, making it possible to study astrophysical processes that source gravitational waves with a signal strong enough to be detected. This includes, as previously mentioned, binary black hole mergers (see Figure 1.6 (b)), neutron star mergers, or core-collapse supernova explosions (it is important to note that such events also produce counterparts in other forms, like electromagnetic radiation, and can therefore be examined with multiple messengers). Besides LIGO, there are more gravitational-wave observatories, aiming to enrich our knowledge about the nature of gravity and these powerful phenomena in the Universe (like Virgo in Italy or KAGRA in Japan). There are also plans to launch a space-based observatory, called the Laser Interferometer Space Antenna (LISA), that will be highly sensitive, having an arm length of about 2.5 million km [29, 30].

Gravitational waves were also generated during the epoch of cosmic inflation, leaving an imprint in the polarization of the cosmic microwave background. CMB exhibits two types of polarization patterns – the E modes (curl-free component) and B modes (curl component). We know that density fluctuations in the early Universe sourced the former ones, but not the latter. The B modes could not be created by these scalar perturbations (to first order), but only by tensor perturbations – the primordial gravitational waves. Their detection would provide important data to perform tests of inflationary models and increase our knowledge about the conditions at the very beginning of the Universe. Nevertheless, this component is very faint compared to E-modes or foregrounds and, therefore, hard to measure. Moreover, in addition to primordial gravitational waves, there are other effects producing this type of polarization pattern (like gravitational lensing), which have to be identified and separated [31, 32]. The experimental endeavors in this field include missions like the Light satellite for the studies of B mode polarization and Inflation from the cosmic background Radiation Detection (LiteBIRD), the Background Imaging of Cosmic Extragalactic Polarization (BICEP), and many more.

1.3.3 Neutrinos and Cosmic Rays

The next cosmic messengers, used to study the Universe, are neutrinos. According to the Standard Model (SM) of particle physics, they are massless and come in three different flavors – electron, muon, and tau. However, various experiments suggest that neutrinos have, in fact, tiny masses and can oscillate between their flavors, which indicates deviations from SM. Astronomical observations may provide important insights to quantify and explain these phenomena, which is a great example of the interconnection between the smallest sizes of subatomic particles and studies on huge cosmological scales. Neutrinos had an important impact on the evolution of the Universe, especially during the Big Bang Nucleosynthesis (affecting the nuclear reactions and cosmic expansion rate), but also at later times, when the formation of large-scale structures took place [33]. Moreover, they influence the form of the CMB power spectrum, making it possible to provide constraints on the sum of neutrino masses with CMB experiments. The upper limit from the Planck satellite, combined with data from baryon acoustic oscillations (BAO) and gravitational lensing, gives $\sum m_\nu < 0.12$ eV (with 95% CL) [28].

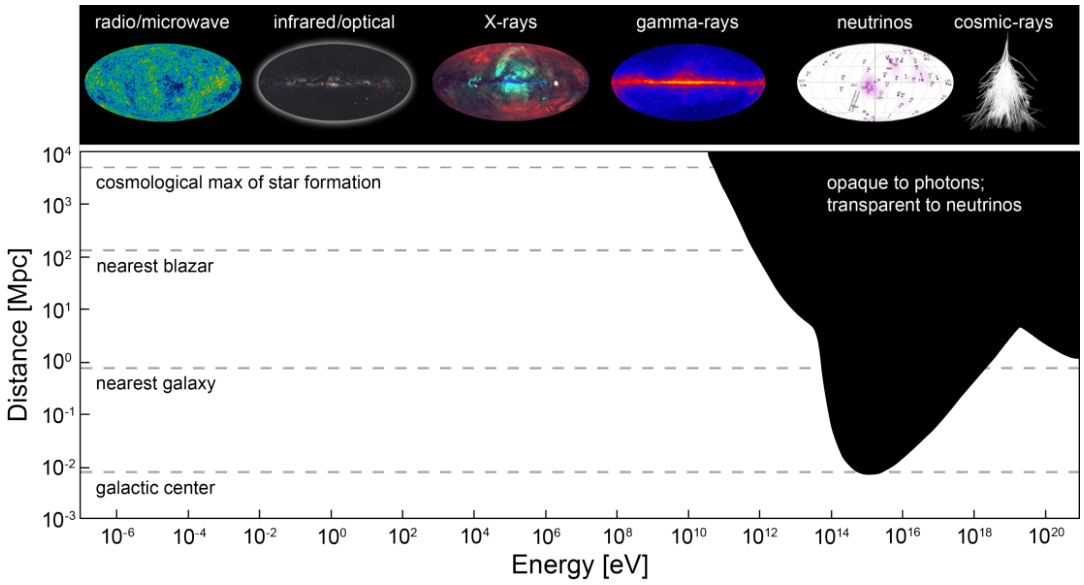

Figure 1.7: Energy of emission and distance to various objects, together with associated parts of the electromagnetic spectrum that can be used to observe these sources. The area of about 20% on the plot cannot be studied with telescopes collecting photons, but this gap can be filled with detections of highly energetic neutrinos and cosmic rays. Credit: IceCube [34].

They are very abundant particle species and come from a variety of sources. First of all, there are relic neutrinos from the Big Bang, that had decoupled from matter even before photons did, constituting the cosmic neutrino background (as mentioned in Section 1.2.2). Some other examples include solar (electron) neutrinos, created during the fusion processes, or neutrinos produced in Earth's atmosphere (about 15 km above the surface) when an energetic cosmic ray passes by. There are also big amounts of neutrinos being released during supernova explosions and from extremely powerful extragalactic sources like active galactic nuclei, gamma-ray bursts, or tidal disruption events (occurring when a star approaches a supermassive black hole and gets torn apart). Finally, we can produce neutrinos, for instance with the beta decay process (neutron transforms into proton, electron, and electron antineutrino) in nuclear reactors, which is very valuable for studying these particles. In fact, the very first detection of neutrino in 1956 happened this way, becoming an important discovery for which the Nobel Prize in Physics was awarded to Frederick Reines and Clyde Cowan [35].

The detection of cosmic neutrinos is very difficult since they rarely interact with other particles. However, neutrinos can provide crucial information about the powerful astrophysical sources emitting in high energy ranges, which cannot be explored using telescopes observing electromagnetic radiation (see Figure 1.7). One of the experiments designed to search for such highly energetic neutrinos is the IceCube, located deep in the ice at the South Pole. The schematic illustration of its construction is shown in

Figure 1.8. On the surface, there is a 1 square kilometer array of 81 stations creating the IceTop, responsible for calibration and detection of particles produced when high-energy cosmic rays hit the atmosphere. The cubic-kilometer detector itself extends from the depth of 1.45 km to 2.45 km in the Antarctic ice and consists of 5160 digital optical modules (DOMs), attached to vertical strings. Some of these have been placed closer together, forming the DeepCore subdetector, which lowers the energy threshold. The observations of neutrinos are indirect – their rare interactions with ice produce charged particles emitting Cherenkov radiation, which is then registered by the IceCube sensors [34]. The first such detection of high-energy neutrinos from astrophysical sources was made in 2013, paving the way for studying the Universe in a completely different manner [33].

At the same time, it enriched the methods of multi-messenger astronomy, which aims to combine observations of electromagnetic radiation, gravitational waves, neutrinos, and cosmic rays. Information about the cosmic objects from multiple messengers is extremely valuable, as they are connected to different astrophysical processes and provide complementary insights that let us characterize the Universe [36].

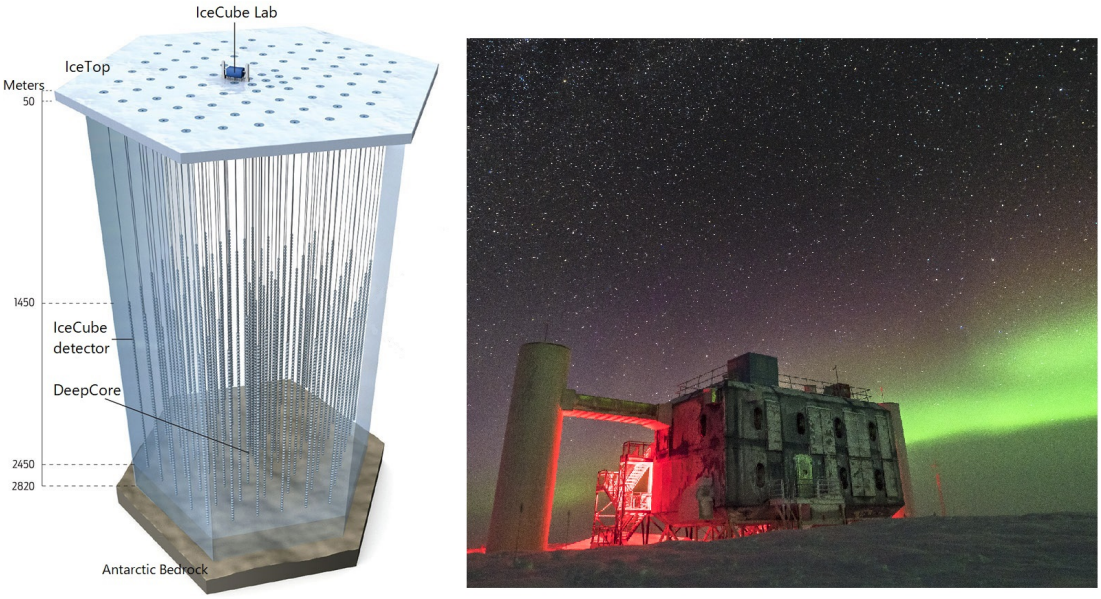

Figure 1.8: IceCube neutrino observatory, located at the South Pole. Illustration of the IceCube detector (burried in ice) is shown on the left. On the right, we include the picture of the IceCube laboratory, placed on the surface together with the IceTop array. Adapted from E. Cooper [37] and IceCube [34].

Chapter 2

Line Intensity Mapping

New insights into unexplored regimes of observational cosmology

Galaxies consist of several components, including dark matter, stars, gas, and dust. One of the most important sources of information about galaxies is their spectral energy distribution (SED). It characterizes the radiation from stars across the electromagnetic spectrum, modified by emission and absorption from the interstellar medium (ISM) [38]. These spectral features trace the composition of gas and are extremely valuable indicators of prevailing physical conditions in galaxies. An illustrative example of a typical SED associated with a star-forming galaxy is shown in Figure 2.1, where we also mark the positions of some carbon monoxide emission lines. The illustration corresponds to redshift $z = 0$, but the entire SED would be shifted towards the longer wavelengths for galaxies at higher redshifts [39]. This effect can be established by measuring the displacement of spectral lines and using Equation 1.2. At the same time, the wavelength dependence enables observing the line-of-sight distribution of emitters, which is the approach used in line intensity mapping (LIM).

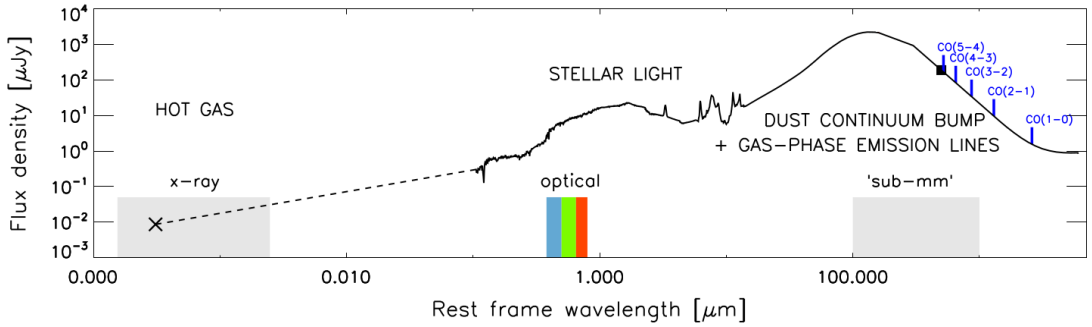

Figure 2.1: Spectral energy distribution (SED) of a typical galaxy with star formation, shown in the rest-frame of the galaxy (at $z = 0$). Illustration points out the emission from different components, together with some spectral lines of carbon monoxide. Adapted from K. Olsen [39].

In this chapter, we will present some main ideas behind LIM, setting COMAP, which we will look closer at throughout the next chapters, in the context of other experiments and the entire field. We will describe how three-dimensional maps of the Universe can be obtained by registering the spectral line emission from atoms and molecules in galaxies and the diffuse intergalactic medium (IGM). The focus will be put on techniques of line intensity mapping, pointing out its advantages and scientific goals, and explaining how the target lines arise as results of quantum phenomena.

2.1 The highlights of Line Intensity Mapping

LIM is an emerging field of experimental astronomy, based on measuring the integrated light from spectral lines over cosmologically large volumes of the Universe. This approach is highly beneficial since we register cumulative emission from all line sources, instead of counting single galaxies that are the brightest. Through mapping intensity fluctuations, we gain information about the underlying large-scale structure and can follow its evolution. Each three-dimensional resolution element of a map obtained in such a way is called a *voxel* (a volumetric pixel). In addition to the contribution from the IGM, it contains several galaxies that might be too faint to be detected individually by galaxy surveys (which usually observe only the ones above a certain threshold, as mentioned in Section 1.3.1) [20, 40]. This is illustrated in Figure 2.2, where we show a 2.5 deg^2 simulated patch of sky with positions of galaxies (a) and the corresponding intensity map of emission from carbon monoxide lines (b). A LIM experiment like COMAP (with one telescope) would spend about 1500 hours observing such an area in order to map fluctuations of CO emission throughout the entire field. Meanwhile, a survey conducted by the Very Large Array (VLA) radio astronomy observatory, employing 27 antennas, would take three times longer. Moreover, its results would include

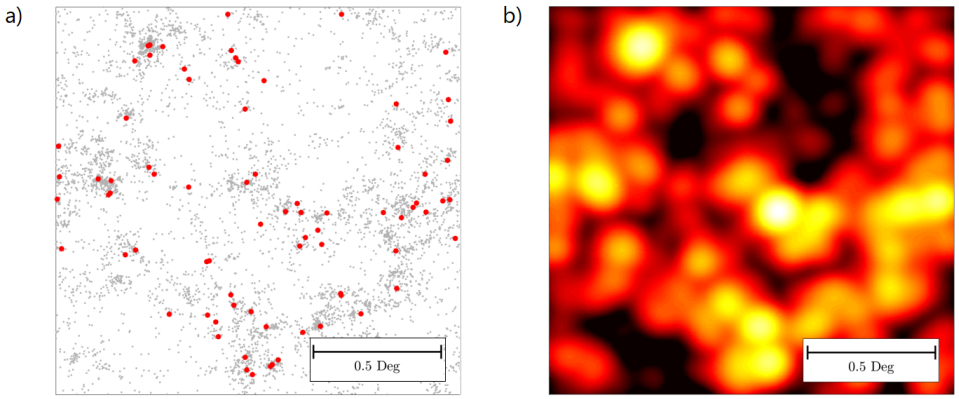

Figure 2.2: Sky patch with an area of 2.5 deg^2, obtained from simulations. a) Positions of galaxies, where red dots indicate the brightest ones, detectable after 1 hour of observations with VLA. b) Map of CO intensity fluctuations. Credit: P. Breysse [41].

only about 1% of galaxy population with CO emitters [41].

In Section 1.3.1, we mentioned that many galaxy surveys are limited to redshifts $z \lesssim 1$. Sources located at higher redshifts are usually below the required brightness threshold and cannot be resolved. However, since LIM is sensitive to all emitters in the line of sight, including the faint ones, it is capable of accessing these high redshifts, providing information about the epochs in the history of the Universe that are clearly under-explored. Besides galaxy surveys, which study more recent times, we have CMB experiments focusing on the relic radiation, dating back to the Epoch of Recombination around $z \sim 1100$. We do not have much data about the periods in between, like the birth and evolution of the first galaxies or the Epoch of Reionization. The new insights provided by research within LIM can advance our knowledge in these areas. The instruments employed in LIM require quite modest angular resolution and can observe large portions of the sky in a relatively short span of time. This is an additional advantage – such experiments are simply more economical [41, 20].

2.2 Science goals

The advancement of LIM techniques offers prospects for improvement in various areas within cosmology and extragalactic astronomy. This potential has been increasingly realized, although initially, the main goal was gaining more information about the reionization of the Universe at $z \sim 10$. We will point out main ideas and fields of science that will certainly benefit from the wealth of data provided by LIM observations. This section will be based on [20, 41], unless referenced otherwise.

2.2.1 Exploring the Epoch of Reionization

As explained in Section 1.2.3, the emergence of the first luminous objects had a big impact on the environment. The star-forming galaxies became the sources of ultraviolet radiation, capable of ionizing the neutral hydrogen gas around them. Because of that process, the intergalactic medium (IGM) could be found in two states (neutral and ionized) until the bubbles of ionized hydrogen expanded to fill the entire Universe. Therefore, it is crucial to study regions in both of these phases in order to understand the physics and progress of reionization. This can be achieved with LIM, where different redshifted lines probe different objects, as can be seen in Figure 2.3. The examples of lines associated with sources of ionizing photons include CO, [CII], as well as Lyα, which also traces areas around the galaxies. On the other hand, the remaining neutral gas can be probed with the 21 cm line. Simultaneous mapping of multiple spectral lines, originating from the Epoch of Reionization, is very beneficial. It provides complementary data, which enable us to study the physical conditions and details of this under-explored period. The especially important topics of research cover understanding how the process of reionization progressed in time (how big part of the IGM was ionized as a function of redshift) and space (how the size of ionized bubbles evolved). In addition, we can gain insights into the formation and characteristics of ionizing sources (like UV emissivity or ionizing efficiency).

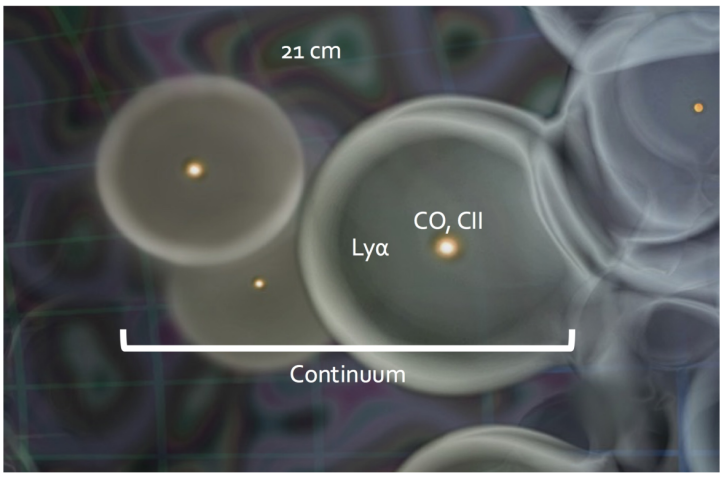

Figure 2.3: Illustration marking various spectral lines, tracing different phases of IGM during the Epoch of Reionization. The neutral gas can be probed with the 21 cm line, whereas the examples of lines mapping the ionizing sources include CO and [CII]. Lyα is associated with the galaxies and halos around them. Credit: Scientific American and P. Breysse [41].

2.2.2 Tracking star formation and evolution of galaxies

Another important application of LIM techniques is studying the history of star formation. Our current state of knowledge in this field is based on measurements of discrete sources that are bright enough to be registered. Such information is clearly insufficient to precisely determine the star formation rate density (SFRD) across cosmic time. This is especially valid for higher redshifts, where contributions from faint sources are significant but very uncertain due to the brightness bias introduced by galaxy surveys. Nevertheless, LIM can improve our understanding of these regimes, providing a statistical description of a huge ensemble of sources, including the ones that are too faint to be resolved individually. Additionally, in order to characterize star formation at high redshifts, present methods rely on observations of light emitted by stars or spectral lines from hot gas in the ISM. LIM, however, offers the advantageous possibility of directly studying the regions of undergoing star formation, probing the cold molecular gas. The emission lines used for this purpose include the ones of carbon monoxide, which is very abundant and resides in quite dense ($\gtrsim 10$ cm^{-3}), cool to warm state of ISM with high metallicity, where stars are effectively born [42]. We can also access other emission lines, for instance [CII], which is a very important source of cooling. Furthermore, the HeII line is a promising tracer of the very oldest stars – Population III. These are extremely massive and luminous objects, forming from metal-free primordial gas at high redshifts (as mentioned in Section 1.2.3).

Different phases of ISM and IGM can be mapped with multiple lines. In order to maximize scientific yield, we can combine information provided by various tracers

and cross-correlate between them. We can, for instance, examine how [CII] and CO luminosities evolve with respect to each other, or employ cross-correlations between isotopologues of molecular lines, like ^{12}CO and (subdominant) ^{13}CO. This approach provides additional information about the distribution of gas and the ratio of isotopes, improving our understanding of the history and physics of star formation, especially at high redshifts.

2.2.3 Probing the ΛCDM model and beyond

Our current state of knowledge indicates that the Universe can be described very well with the ΛCDM model. It is parameterized with six independent quantities, where five of them are already determined with an uncertainty below 1% [28]. This exceptional precision of constraints from cosmological measurements is possible to achieve with CMB experiments, which are complemented by input from galaxy surveys (see Section 1.3.1). The ΛCDM model is extremely consistent with observations across a huge range of cosmological scales and over 10 billion years of cosmic time. Nevertheless, the nature of some essential components, like dark matter or dark energy, is still unknown, which is quite problematic from the perspective of fundamental physics [28]. In addition, the same cosmological observations pinpoint phenomena deviating from expectations of the ΛCDM model. These anomalies may require physical explanations beyond our current state of knowledge. The new insights from LIM can help to unravel some of such mysteries and answer questions related to the nature of the early Universe.

The important features, that make LIM an invaluable tool of cosmology, include its large field of view with a wide range of cosmological scales and its ability to access high redshifts. The emission line sources are said to be biased tracers of the underlying dark matter density fluctuations. Therefore, they are an extremely helpful probe in studies focused on large-scale structures. This opens up many possibilities, including measuring the baryonic acoustic oscillations (BAO), for instance through mapping the intensity of Lyα emission. The BAO are matter density fluctuations, which were created due to sound waves traveling in the primordial fluid, where photons and baryons were still coupled. While the early Universe expanded and cooled down, it eventually reached the Epoch of Recombination. At that time, these acoustic waves were frozen in place, as the sound speed of baryons essentially dropped to zero. They set a specific length scale, which made them a *standard rod*, being a very important tool for measuring distances and constraining related cosmological parameters [13]. In addition to probing the BAO, LIM can contribute to establishing neutrino masses. This task requires observations conducted over large volumes of the Universe, on both large and small scales. Intensity mapping of the 21 cm line has the potential to bring about improvement in this field. Furthermore, there are many applications beyond the ΛCDM model – for instance, studying how the dark-energy equation of state varies with time, which is especially relevant at redshifts $z \gtrsim 2$, where departures from the cosmological constant are most expected.

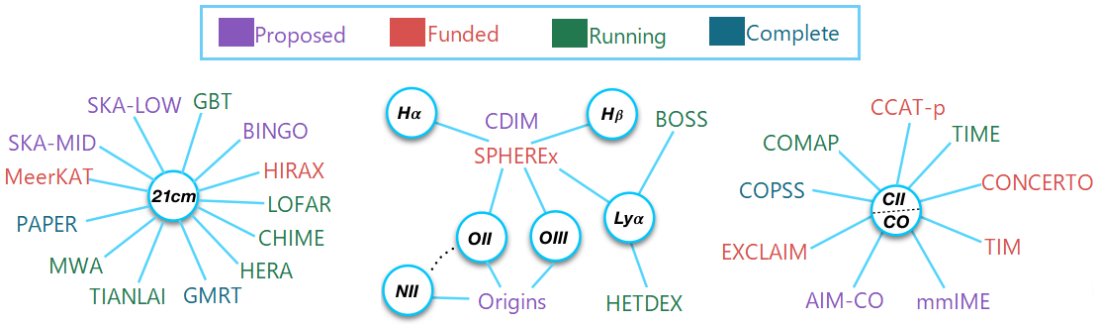

Figure 2.4: Selection of various line intensity mapping experiments, together with the associated spectral lines. Adapted from [20].

2.3 Experimental targets and line emission

Data from spectral line emission might be used to constrain conditions in various astronomical objects. The species of involved tracers indicate the chemical composition of sources and the observed deviation from rest frequency allows estimating redshift. In the previous section, we stated some of the science goals of LIM, giving examples of spectral lines that may be used as targets, as well as their environments and surroundings. Now, we will provide a physical description of these quantum phenomena. We will focus on the emission lines that are crucial for this science field and became targets of many experiments, which we show examples of in Figure 2.4. The CO Mapping Array Pathfinder (COMAP) – the subject of this thesis – is placed here among other instruments of the LIM experimental landscape. It targets the rotational lines of carbon monoxide along with, for instance, the CO Power Spectrum Survey (COPSS) or the ASIAA Intensity Mapping for CO (AIM-CO). There are also projects focusing on studying regions traced by ionized carbon fine structure line, [CII], like the Tomographic Intensity Mapping Experiment (TIME) or The CarbON [CII] line in post-rEionization and ReionizaTiOn epoch project (CONCERTO). Finally, we have a broad range of experiments targeting the 21 cm line, as well as other hydrogen lines, including Lyα, studied by the Spectro-Photometer for the History of the Universe, Epoch of Reionization, and Ices Explorer (SPHEREx) [41].

2.3.1 Hydrogen lines – Lyα and 21 cm

Hydrogen is the lightest and most abundant element in the Universe, constituting a majority of the entire baryonic matter content. Its neutral atom consists of a nucleus with a proton, orbited by a single electron in one of many possible energy states. Only quantized orbitals are allowed, specified by the so-called principal quantum number, n, where n is a natural number. However, the electron can undergo a transition from some

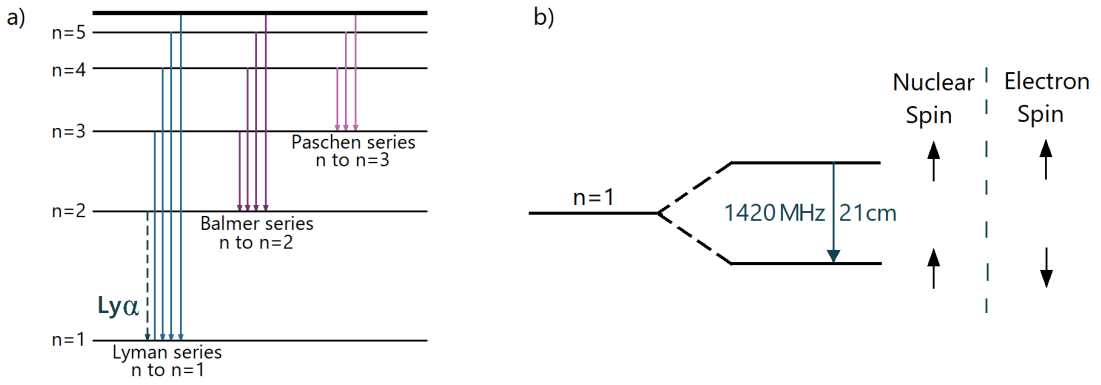

Figure 2.5: Energy-level diagrams of hydrogen atom. a) Spectral series with electron transitions between different energy levels. Lyman-α line, arising from transition between $n = 2$ and $n = 1$, is marked. b) Hyperfine splitting of the ground state ($n = 1$). The spin flip results in realising the energy difference between two states, corresponding to wavelength of 21 cm (or frequency 1420 MHz).

level quantified by $(n + \Delta n)$, to a lower level n. Simultaneously, it radiates away the energy difference between these two states, which can be observed as a spectral line emission. For the hydrogen atom, it is customary to name the transitions to lower states marked by $n = 1, 2, 3$ consecutively Lyman, Balmer, and Paschen series (see Figure 2.5). Moreover, the lines in each series are denoted with Greek letters, depending on the energy difference between levels involved in the transition, so that $\Delta n = 1, 2, 3$ corresponds respectively to α, β, γ [43, 44]. Following this terminology, our Lyman-α (or Lyα) line is created by the transition from the orbital with $n = 2$ to the ground state of the hydrogen atom ($n = 1$). Lyα is a very bright ultraviolet line, with the rest-frame wavelength of 121.6 nm. It is a very promising target for LIM, originally used for probing Lyα emitting (LAE) galaxies at high redshifts [41].

An important quantum effect that needs to be taken into consideration is hyperfine splitting. Each n'th energy level in the atomic hydrogen is split into $2n^2$ discrete states. The factor of 2 comes from both possible configurations of electron spin with respect to the direction of nuclear spin, as shown in Figure 2.5. These two quantum components are associated with somewhat different energies. Their difference is emitted during the change of electron spin from the state with higher energy (parallel spins) to the one with lower energy (antiparallel spins). For the ground state of the hydrogen atom, this transition results in the energy release of about 6 μeV, corresponding to the frequency of 1420 MHz, or the wavelength of 21 cm [44]. This spectral line, originating from neutral intergalactic hydrogen, was the initial motivation for LIM and remains to be one of the most common targets until this day. The first detection of emission from redshifted 21 cm line (at $z \approx 0.8$) has already been made by cross-correlating data from the Green Bank Telescope (GBT) with DEEP2 optical galaxy survey [41].

2.3.2 Ionized Carbon line – [CII]

Another crucial tracer, mentioned in Section 2.2, is the emission line of singly ionized carbon. It is a fine-structure spectral line, arising as a result of the transition from the quantum state $^2P_{3/2}$ to the state $^2P_{1/2}$. In order to understand this terminology, we need to build upon the physical description of atomic structure, limited to the ground state ($n = 1$) in our previous discussion of the 21 cm line. Each electronic energy level, n, has an associated set of possible angular momentum quantum numbers, $\ell = 0, 1, 2, ..., n-1$, defining the shape of orbital. For $n = 2$, we have then two possibilities – labeled either by $\ell = 0$ (corresponding to S) or $\ell = 1$ (corresponding to our case, P). In addition, the electron has spin one-half, which can be found in one of the two quantum states ($+1/2$ or $-1/2$). We can define the total angular momentum quantum number of an electron, j, as a vector sum of its spin and orbital momentum. It takes various values due to described fine splitting, $j = \ell \pm 1/2$. This number gives the right lower index in the state labels, $^2P_{3/2}$ ($j = 1 + 1/2$) and $^2P_{1/2}$ ($j = 1 - 1/2$). The left upper index comes from $n = 2$, which is the associated principal quantum number [45].

The change between the above fine-structure states in singly ionized carbon, CII, has low quantum mechanical transition probability, as indicated by the double square bracket, [CII] [13]. It gives rise to the so-called forbidden emission line at 157.7 μm, which corresponds to the frequency of $\sim$ 1900.5 GHz (far-infrared part of the electromagnetic spectrum). This metal line is very luminous and carbon itself is a highly abundant element in the Universe, residing in various phases of the interstellar medium within the galaxies with undergoing star formation. A big part of the carbon content gets ionized by the ultraviolet light traveling through the ISM. The CII ion can be found surrounded by either ionized or neutral hydrogen gas, due to its relatively low ionization potential, 11.3 eV, compared to hydrogen, 13.6 eV. The [CII] line emission can be therefore used to probe both phases of the gas. It is connected to the star formation and constitutes a very important cooling mechanism for the neutral ISM [39, 41].

2.3.3 Molecular rotational lines – CO

As previously mentioned, the baryonic matter content of the Universe is dominated by hydrogen. It is then natural, that the most common molecule is its diatomic form, H_2. Nevertheless, the spectral lines of H_2 are very difficult to observe. This comes from the fact that symmetric molecules, such as H_2, have no permanent electric dipole moment (so that electric quadrupole transitions are required, which have very low probability). However, the case is different for the molecules with asymmetric electric charge distribution, like carbon monoxide (CO) – the second most abundant molecule in the Universe [39, 43]. The electric dipole moment of CO is nonzero and varies sinusoidally as the molecule rotates, in sync with its angular frequency. Simultaneously, the changes of rotational energy are radiated away, resulting in spectral line emission. These energy transitions and, as a consequence, frequencies of emitted photons are quantized. Therefore, the rotational lines, arising as a result of $J \to J - 1$ transitions (J is the angular momentum quantum number of the higher energy level, $J = 1, 2, ...$), can occur only

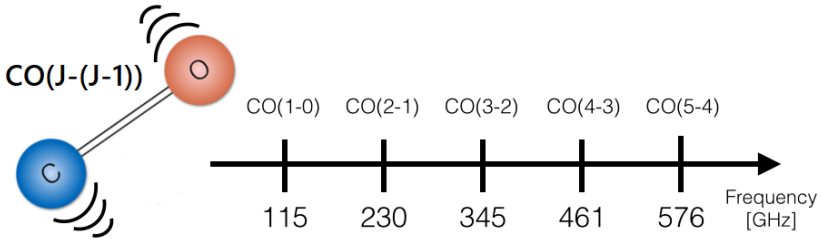

Figure 2.6: Carbon monoxide molecule and the set of first 5 rotational transitions, resulting in emission lines at discrete frequencies. Adapted from K. Olsen [39].

at frequencies with certain allowed values,

$$\nu_{J\to J-1} = \frac{\hbar J}{2\pi m_{\mathrm{CO}} r_e^2}, \tag{2.1}$$

where $\hbar$ is the reduced Planck constant, r_e is the equilibrium distance between carbon and oxygen atom in the CO molecule, and m_{CO} is the reduced mass of the molecule, $m_{\mathrm{CO}} \equiv m_{\mathrm{C}} m_{\mathrm{O}}/(m_{\mathrm{C}} + m_{\mathrm{O}})$. The set of spectral lines, resulting from such transitions, resembles then a ladder, where consecutive frequencies are multiples of the frequency associated with the ground-state transition, $\nu_{J\to J-1} = J\nu_{1\to 0}$ (see Figure 2.6). In the case of the CO molecule, this fundamental transition, CO(1-0), occurs at 115.3 GHz (2.6 mm), which falls into the radio part of the electromagnetic spectrum [43].

Carbon monoxide is a very important tracer of molecular ISM and star formation. The CO-emitting galaxies can usually source multiple rotational lines simultaneously, which is highly advantageous, as it enables cross-correlation and extracting the pure CO signal. Moreover, the observed relative flux of different lines is a great indicator of physical conditions prevailing in gas, such as temperature or density [39, 42].

2.4 Characterization of the signal and observables

The variety of experiments, conducting observations within the field of line intensity mapping, can provide an unprecedented wealth of data from multiple emission lines. It is crucial to know how to use these measurements for extracting valuable information, which can subsequently be compared to theoretical predictions and translated into constraints on astrophysical and cosmological quantities of interest. In order to quantify statistical properties associated with our maps of line intensity fluctuations, we can construct different observables. The most common one remains the power spectrum, which is the Fourier transform of the two-point correlation function. In the case of mapping emission lines at some redshift z, it can be characterized by the following model,

$$P(k,z) = \overline{T}^2(z)\bar{b}^2(z)P_m(k,z) + P_{\mathrm{shot}}(z). \tag{2.2}$$

There are two terms in the above equation – clustering and shot noise. The former one dominates at large scales (lower values of wave number, k) and the scale-independent

contribution from shot noise becomes more significant at small scales (higher values of k), as can be seen in Figure 2.7 (a). This power spectrum model indicates how LIM can provide important insights into the research within both cosmology and astrophysics. The clustering term follows the underlying distribution of dark matter fluctuations, with power spectrum $P_m(k, z)$, which depends on cosmological parameters. Other factors are related to the luminosity of line emission from the entire population of source galaxies, associated with their astrophysical properties. We have the luminosity-weighted bias of the line,

$$\bar{b} = \frac{\int Lb(L)\Phi(L)\,dL}{\int L\Phi(L)}, \tag{2.3}$$

where $\Phi(L)$ is the line luminosity function and $b(L)$ is the bias of some galaxy with luminosity L. The sky-averaged brightness temperature, $\overline{T}$, and the shot noise term in Equation 2.2, $P_{\rm shot}$, are proportional respectively to the first and the second moment of the line luminosity function,

$$\overline{T} \propto \int_0^\infty L\Phi(L)\,dL, \qquad P_{\rm shot} \propto \int_0^\infty L^2\Phi(L)\,dL. \tag{2.4}$$

The power spectrum is a two-point statistic, and is a very important tool used in many different branches of cosmology, like studying the distribution of galaxies or CMB experiments. If the field is Gaussian, the power spectrum contains all the statistical information about it. However, the fluctuations on small scales of our line intensity maps result from highly nonlinear effects and are therefore not expected to be perfectly Gaussian. The power spectrum leaves out these details, hence we want to introduce another method to characterize the field – the voxel intensity distribution (VID), which is a one-point statistic. As illustrated in Figure 2.7, two different line luminosity functions, which have identical power spectra, can still be identified by their VIDs.

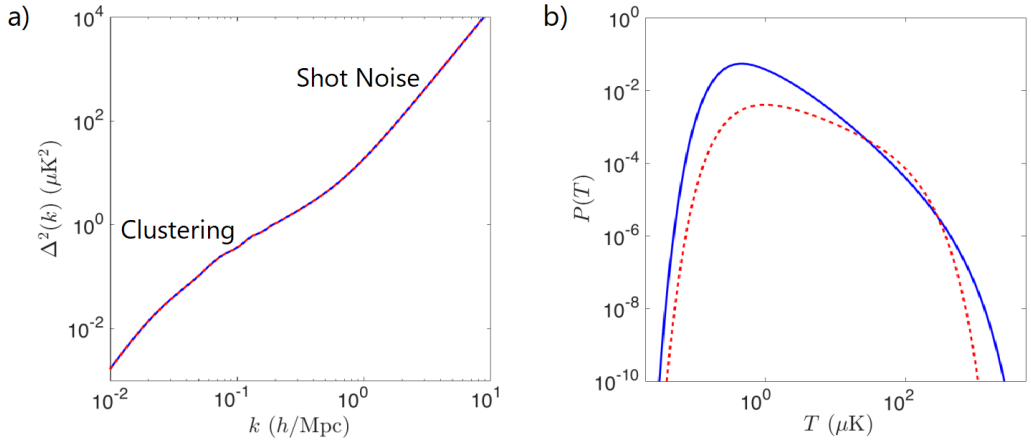

Figure 2.7: Comparison between a) power spectra and b) voxel intensity distributions (VIDs) of two different line luminosity functions (the red dashed curve corresponds to five times fewer emitters than the blue curve). Adapted from P. Breysse [41].

The VID is the probability distribution of brightness temperature in the voxels (resolution elements of 3D line intensity maps), $\mathcal{P}(T)$. The expectation values for the number of voxels with temperatures in range between T_i and T_{i+1} are given by

$$\langle B_i \rangle = N_{\text{vox}} \int_{T_i}^{T_{i+1}} \mathcal{P}(T)\, dT, \tag{2.5}$$

where N_{vox} is the total number of voxels in the map. Such a histogram provides a way of characterizing the entire luminosity function, not just its first two moments (Equation 2.4). The description of observables and discussion in this section so far followed [41, 46, 47].

It is important to note that the power spectrum and voxel intensity distribution are complementary observables. We can combine information provided by both of them into one data vector on the form $d_i = (P_{k_i}, B_i)$. This joint-analysis approach is highly advantageous, as it leads to decreasing the uncertainties on the CO luminosity function by 20–70% (for the COMAP experiment) compared to employing a single statistic. In general, the properties of the signal determine if it is more beneficial to use the VID over the power spectrum. Any effect that elevates the non-gaussianity of the map, increasing the shot noise, will naturally favor VID [48].

Nevertheless, the power spectrum remains the primary observable for many statistical applications, including the field of line intensity mapping. We will further develop a description of signal models and techniques related to the power spectrum in the second part of the thesis (Chapter 4), devoted to the methods of high-level data analysis in COMAP. Specifically, we will focus on the cross spectrum methodology.

Chapter 3

COMAP

The CO Mapping Array Project

The CO Mapping Array Project is a line intensity mapping experiment, targeting rotational lines of carbon monoxide. The project is currently in the first phase – Pathfinder – referred to as COMAP throughout this thesis. The observations are carried out using a single telescope, with the frequency coverage in Ka-band, between 26 and 34 GHz (corresponding to wavelength 11.5 – 8.8 mm). The ground state rotational transition of the CO molecule, CO(1-0), occurring in rest-frame at ∼115 GHz, gets redshifted from the Epoch of Galaxy Assembly ($z = 2.4 - 3.4$) to fall into our frequency range. The goal of the Pathfinder is to test technology, detect this signal, and place limits on the properties of CO-emitting galaxies at that time. There is also a fainter contribution of CO(2-1) signal from a higher redshift slice, $z = 6 - 8$ (as the rest-frame frequency of

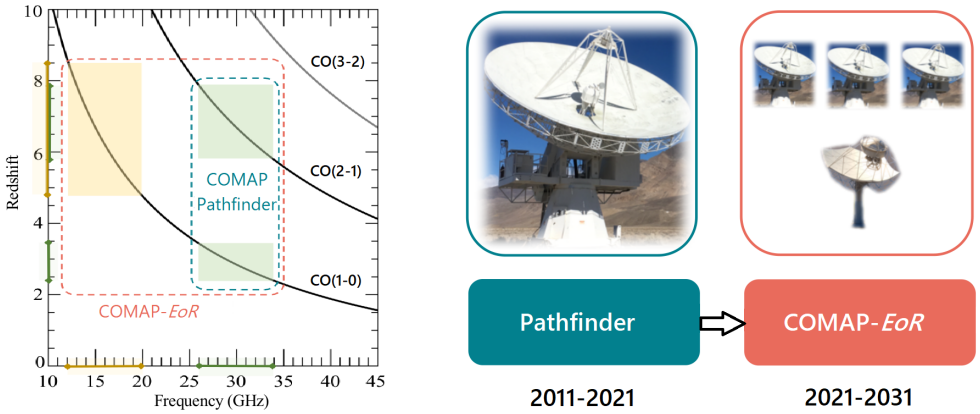

Figure 3.1: Two stages of COMAP, targeting different frequency ranges. Illustration shows the current Pathfinder phase, with a single receiver observing in Ka-band, as well as the planned COMAP-*EoR* phase, with two more Ka receivers and an additional Ku one. Adapted from K. Cleary [49].

this transition is larger). These redshifts correspond to the Epoch of Reionization (EoR), which is, in fact, the aim of the second stage of the experiment, COMAP-*EoR*. In this future phase, we plan to expand the telescope array by adding two extra Ka receivers, as well as one Ku receiver with coverage at lower frequencies, between 12 and 20 GHz (or wavelength 2.5 – 1.5 cm). The Ku-band is sensitive to the CO(1-0) line signal from $z = 5 - 8$, which in cross-correlation with CO(2-1) observations in Ka-band will enable studying the Epoch of Reionization. These plans are illustrated in Figure 3.1.

Many institutions constitute the COMAP collaboration, including Caltech, JPL, Stanford University, University of Manchester, Canadian Institute of Theoretical Astrophysics, Maryland University, Miami University, University of California (Berkeley), Princeton University, and University of Oslo. In this chapter, we will present work led by different groups being a part of the project in its current phase. We will provide a description of the instrument, observations, as well as data analysis. There are two separate teams in COMAP conducting data analysis – one in charge of the main CO science (Oslo) and another one responsible for the Galactic plane observations (Manchester). The focus will be put on the CO science pipeline, with lower level analysis described in this chapter and higher level analysis, whose development is the subject of the thesis, in Part II (Methods). Unless referenced otherwise, we will base our discussion on the selection of memos and presentations acquired from the COMAP Wiki page [49], as well as conversations with members of the collaboration and their work [47, 50, 51, 52].

3.1 Instrument and signal

3.1.1 The antenna

In the first phase of COMAP, we use a 19-element receiver, installed on a 10.4 m telescope located at the Owens Valley Radio Observatory (OVRO) in California, USA. The antenna design was developed over 40 years ago by Robert B. Leighton – a renowned experimental physicist and professor at Caltech. He was able to overcome many structural challenges, including gravity and wind deflections, and construct radio telescopes with very high precision. Originally, six of such telescopes were deployed at OVRO, forming the Millimeter Array (MMA), which made a significant contribution to studies of galaxies and star formation. Thereafter, the antennas were moved and incorporated into the Combined Array for Research in Millimeter-wave Astronomy (CARMA), which was decommissioned in 2015. Most recently, the telescopes came back to OVRO, where some time later one of them could be repurposed for the COMAP experiment [53]. The main science observations started in June of 2019.

The telescope is of Cassegrain type. The primary reflector (concave) has a diameter of 10.4 m, whereas the secondary one (convex) is 1.1 m across (larger than in the original Leighton, which was ~ 0.6 m). The dish consists of 84 hexagonal aluminum panels, mounted on a backup structure – a grid made of high-strength steel triangular frames. The reflecting surface is covered with aluminum sheets, properly attached and deformed to achieve high accuracy and prevent defocusing. The instrument is supported on the alt-azimuth fork mount. This type was selected because of its many advantages,

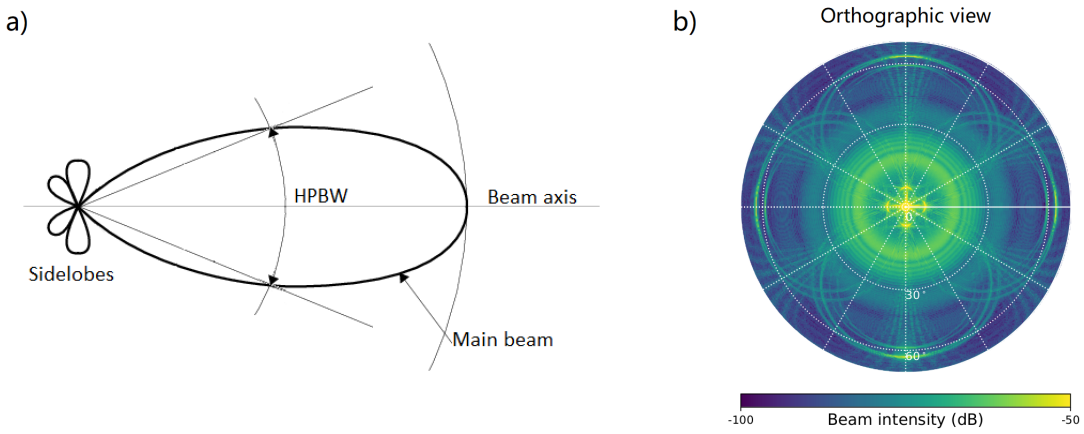

Figure 3.2: a) Sketch of the full beam pattern of the reflector antenna, with half-power beamwidth (HPBW) marked. Adapted from [54]. b) Simulated beam model of the COMAP telescope, showing far sidelobes extending to about 70°. Credit: J. Lamb.

including strength, mobility, and simplicity [55]. It allows repointing the dish along horizontal and vertical axes, respectively changing the azimuth and altitude (elevation) of the telescope's target during observations. Nevertheless, this solution limits the accessible elevation and requires avoiding objects close to the local zenith, as it would drastically increase the azimuth velocity to be beyond the capabilities of the engine [56].

3.1.2 Instrumental beam

The goal of the telescope is to gather electromagnetic radiation from a specific observed direction in the focal point, minimizing the signal contributions from other directions. When an object illuminates the dish, the light gets reflected and forms a wavefront propagating along the axis of the antenna. This outgoing wavefront creates a radiation pattern called a *beam*, which depends on diffraction effects and the parameters of the reflector. The exact shape of the beam has an impact on the observed signal, so it is important to understand its general properties, illustrated in Figure 3.2. As shown, most of the power is concentrated in the sharp maximum along the beam axis – the main beam. In addition, the pattern is affected by contributions from other directions, resulting in sidelobes. They can be caused by light reflection from various parts of the instrument, like the support legs carrying the secondary mirror, and have to be taken into account during the data analysis. A useful parameter, which quantifies this effect, is the *beam efficiency*, $\eta_B = \Omega_M/\Omega_A$, which for COMAP is about 0.7. Here, $\Omega_A = \Omega_M + \Omega_S$ is the solid angle corresponding to the entire beam pattern, which can be separated into the main beam, Ω_M, and the combined sidelobes, Ω_S [56].

Another important parameter of the antenna, characterizing the main beam, is *half-power beamwidth* (HPBW). It corresponds to the angle at which the power level is half

of that on the beam axis, given by

$$\theta_A = 1.22\frac{\lambda}{D}, \tag{3.1}$$

where λ is the wavelength and D is the diameter of the antenna aperture. The HPBW quantifies the angular resolution of the instrument, according to the so-called Rayleigh criterion. When applying Equation 3.1 for the case of COMAP, we get about 4 arcmin in the middle of its frequency range, at 30 GHz ($\lambda \approx 10$ mm, $D = 10.4$ m). Nevertheless, the precise value of angular resolution can slightly vary (altering the constant in Equation 3.1), depending on how the reflector is illuminated. Ideally, the aperture illumination is uniform and falls sharply to zero at the edges. In reality, however, this is not achievable and some fraction of the power will spill over the edges from the ground [56], giving an unwanted contribution to the measured signal, which has to be taken into account during the data analysis.

3.1.3 The receiver and path of the signal

The path of the signal begins with the light being collected by the parabolic dish antenna and directed into the secondary mirror. Thereafter, it gets reflected again to reach the receiver, comprised of an array of 19 feedhorns and the cryostat. Every feedhorn is associated with a specific line of sight in the focal plane and starts an independent detector chain, called *pixel* or *feed*, which processes the signal as shown in Figure 3.3 (a). The light from each feedhorn enters the cryostat, where a low temperature ($\sim$ 20 K) is held to reduce the instrumental noise from electronics located inside. The first step here is the circular polarization of light, with the exact process being slightly different depending on the feed – the majority of them have two-stage polarizers, but two have one-stage polarizers and two have none, as shown in Figure 3.3 (b). This variety of solutions was applied in order to perform engineering tests of the system. It turns out, that data from the feeds with no polarizers (4 and 7) exhibit larger signals from standing waves, occurring between the focal plane and the secondary reflector. Due to this systematic effect, these feeds are currently removed from the subsequent analysis (in addition to feed 6, which experienced other problems). Another component on the path of the signal is a low-noise amplifier (LNA), which (as the name suggests) amplifies its power, without introducing much noise. In addition to 19 LNAs (for each detector chain), there is an extra 20th terminated LNA, which corresponds to a blind feed (as it does not observe the sky). It is naturally also excluded from science data but can prove useful for identifying signals generated inside the system and distinguishing them from external ones.

The polarized and amplified signal moves into the first down converter module (DCM1), located in one of the saddlebags installed next to the receiver. DCM1 lowers the frequency of the signal from the input between 26 and 34 GHz to the output in the 2–10 GHz band. The signal is thereafter sent to the second stage of down-conversion (DCM2), taking place in the telescope side-cabin. This time, the frequency band is split into two parts with 4 GHz bandwidth each – A (2–6 GHz) and B (6–10 GHz).

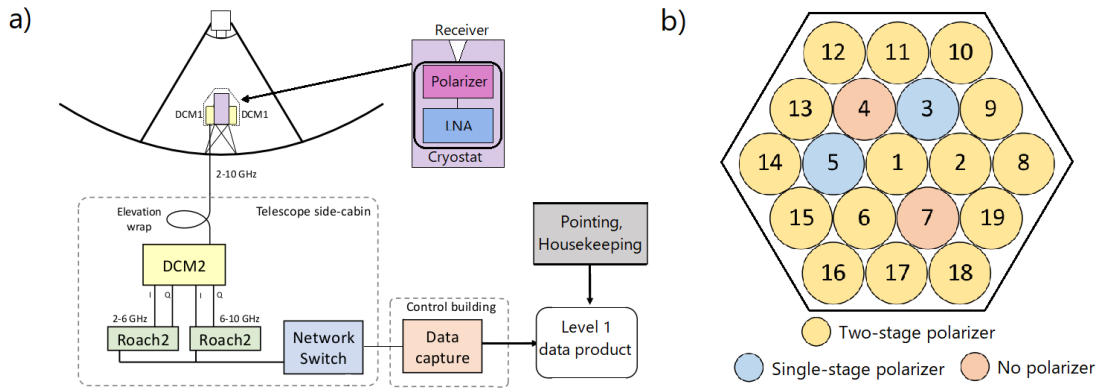

Figure 3.3: Signal processing in COMAP. a) Path of the signal in each feed from the receiver to the final product – level 1 data. b) Array of feeds with different polarizer solutions. Adapted from K. Cleary [49].

The signal in both bands is further decomposed into *in-phase* (I) and *quadrature* (Q) components, which proceed to the *Roach2* spectrometers. Band A and B, independently from each other, are processed by such spectrometers, first going through the analog-to-digital converter (ADC) and then through the Field-programmable gate array (FPGA). The cumulative output of this procedure is four sidebands, labeled as A LSB (26–28 GHz), A USB (28–30 GHz), B LSB (30–32 GHz), and B USB (32–34 GHz). Here, A and B refer to the primary band and LSB or USB stands for lower sideband or upper sideband, respectively. All of them have a width of 2 GHz and are divided into 1024 channels, yielding a $\sim$ 2 MHz spectral resolution. Data at this stage consist of time samples, which are integrated every 20 ms (resulting in the temporal sampling rate of 50 Hz) and sent into the control building in the vicinity of the telescope. After adding the pointing and housekeeping information at Caltech, we get so-called level 1 data, which are subsequently the subject of further analysis in Oslo.

3.1.4 Signal components

Following the path through all of the signal processing stages in the system, the power output for each frequency channel can be modelled as

$$P_{\text{out}} = k_{\text{B}} G \Delta\nu T_{\text{sys}}, \tag{3.2}$$

where k_{B} is the Boltzmann constant, G is the instrumental gain (quantifying the amplification of the signal from the input to the output level), $\Delta\nu$ is the frequency bandwidth, and T_{sys} is the total system temperature, comprised of various components,

$$T_{\text{sys}} = T_{\text{receiver}} + T_{\text{atmosphere}} + T_{\text{ground}} + T_{\text{CMB}} + T_{\text{foregrounds}} + T_{\text{CO}}. \tag{3.3}$$

We need to understand each source in the equation above, in order to extract the CO line emission signal, T_{CO}, which is the main science goal of COMAP. This task is quite

challenging since from theoretical predictions we expect the cosmological CO signal to be very weak (a few microkelvins) compared to the total system temperature, $T_{\rm sys}$, of about 40–45 K. The biggest contribution here is the effective noise temperature of the receiver, $T_{\rm receiver}$, which is estimated to be around 10–30 K for the COMAP instrument. There is also a high noise term from the atmosphere, $T_{\rm atmosphere}$, accounting for 15–25 K. The exact contribution of this term depends on the elevation of the telescope (changing the optical thickness of the atmosphere) and weather conditions, which vary over long time scales. The third factor is the ground contamination, $T_{\rm ground}$, being the result of the beam far sidelobes hitting the ground. This systematic effect adds about 1.5–2 K to the total system temperature and can be quite difficult to handle since it is correlated with the pointing of the telescope. The remaining terms in Equation 3.3, $T_{\rm CMB}$ and $T_{\rm foregrounds}$, correspond respectively to the signal from the CMB (~ 2.7 K) and Galactic continuum foregrounds (~ 1 mK), like free-free or dust emission.

In order to determine the signal of astrophysical origin, we need to separate it from all the noise contributions present in the data. The noise level can either fluctuate randomly or be correlated in time or frequency. The former type is caused mostly by the thermally-induced movement of charged particles, leading to current variations in the electronics of the instrument. This effect is called the Johnson noise and closely depends on the total system temperature, $T_{\rm sys}$. It is associated with the uncertainty of our measurement, having a major contribution to the noise level in each voxel of the final intensity map obtained from the data. As already mentioned, a voxel is a resolution element of the three-dimensional map, where the two angular dimensions correspond to the pixel on the sky and the third line-of-sight dimension is established through frequency dependence. The noise in each voxel (standard deviation of thermal fluctuations) can be described by the so-called radiometer equation,

$$\sigma_N = \frac{T_{\rm sys}}{\sqrt{\tau \Delta\nu}} = \frac{T_{\rm sys}\sqrt{N_{\rm pixels}}}{\sqrt{\tau_{\rm tot}\epsilon_{\rm obs} N_{\rm feeds}\Delta\nu}}, \tag{3.4}$$

where, τ is the observation (or integration) time per pixel on the sky, $\tau_{\rm tot}$ is the total observation time, $N_{\rm feeds}$ and $N_{\rm voxels}$ refer respectively to the number of detector chains in the instrument and the total number of pixels, and $\epsilon_{\rm obs}$ is the integration efficiency (the ratio between desired and observed integration time per pixel). From the above radiometer equation, we can see that in order to minimize the noise level and thereby increase the sensitivity of the experiment, we need to gather more observational data. For the parameters corresponding to the first two years of COMAP's operations, we expect $\sigma_N \approx 11$ μK per voxel, assuming it is uniform over the entire map [48].

Because the random thermal noise, as well as other uncorrelated noise sources, integrates down with observational time, we can just wait for its level to decrease with the accumulation of data. What poses a problem is the presence of temporal and spectral correlations of noise from different sources, which have to be determined and removed in the process of data analysis. The main causes of correlated noise in COMAP are gain fluctuations, atmospheric effects, and standing waves that can occur when an electromagnetic wave gets reflected from various parts of the instrument and interferes with an incident wave.

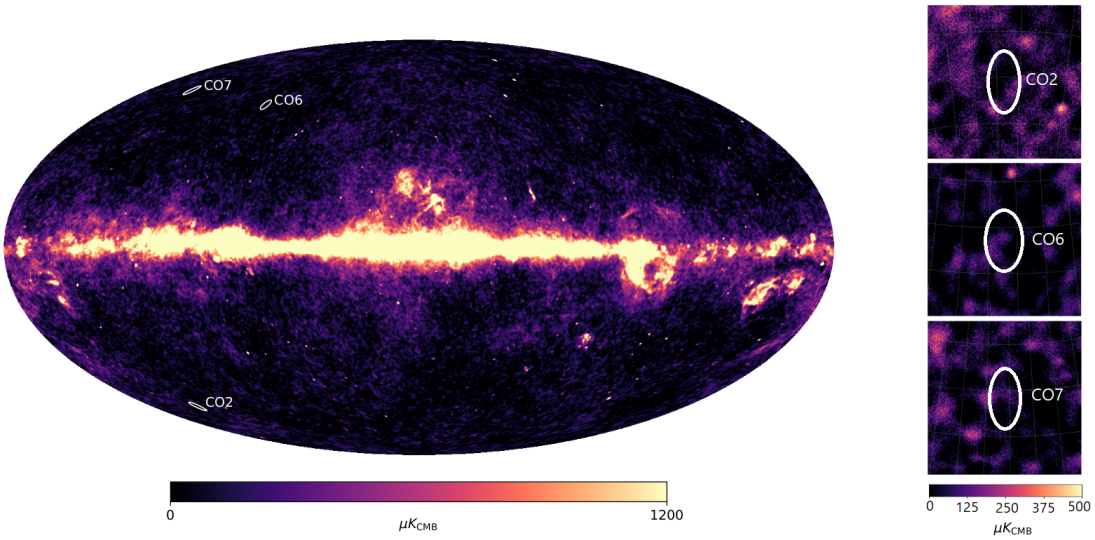

Figure 3.4: Main science fields of COMAP – CO2, CO6, and CO7 – marked by the circles with radius of 2°, plotted on top of the Planck LFI full-mission map of the entire sky (left panel) and the 10° × 10° sky patches enclosing each field (right panel) at 30 GHz. Credit: Planck Collaboration and N. Stutzer [50].

In Section 3.3, we will continue the discussion on the correlated noise and describe different filters that are applied during data processing in order to remove it.

3.2 Observations

3.2.1 Targeted fields

The selection of areas on the sky to be observed by COMAP is influenced by some crucial factors. We want to avoid bright sources in our frequency range and regions where the foreground emission is very strong while retaining a high efficiency of observations. In addition, it is a good idea to choose fields overlapping with the coverage of other related experiments in order to allow for cross-correlation. Line intensity mapping and galaxy surveys provide complementary information about the population of galaxies, making their combination a very powerful tool with high scientific output. LIM gives a statistical description of emitters over a large volume of the Universe, whereas galaxy surveys usually conduct more detailed spectroscopic measurements of the specific targets selected from the preceding wide-field photometric scan. However, we also have another type of spectroscopic surveys, blindly sampling the locations of objects to study. An example of such a survey is the Hobby-Eberly Telescope Dark Energy eXperiment (HETDEX), chosen for cross-correlation with COMAP. Its result will be a catalog of $\sim 10^6$ Lyman-α emitters (LAEs) over ~ 400 deg^2 of the sky and redshift slice $z = 1.9 - 3.5$, possibly accompanied by Lyman-α intensity maps [57]. The main science fields of COMAP, shown in Figure 3.4, were selected in order to overlap with

the regions targeted by HETDEX and take the aforementioned aspects into account. The area called CO2 falls within the HETDEX fall field, CO6 lies outside its main coverage (as it changed since COMAP started observing), and CO7 is inside the spring field. The patches are roughly ~ 4 deg^2 each and are centered at the following positions in Galactic coordinates (longitude, latitude): $(149.0°, -60.3°)$, $(91.35°, 53.22°)$, $(150.64°, 59.53°)$, respectively for CO2, CO6, and CO7. COMAP's strategy is to spend about 1000 hours per year on each science field, assuming that we are observing at an elevation between 30° and 70° (recently corrected to 35°–65°), only during the night and when the Sun or Moon are at least 30° away from the target.

Besides the three main fields, observed in the interest of constraining and detecting the discrete CO line emission, we also conduct continuum observations. A separate data analysis pipeline was developed for this purpose. The program involves the COMAP Galactic Plane Survey (COMAP-GPS), performed between the longitudes 22.5° and 90°, as well as targets like the Andromeda Galaxy (M31) or the Lambda Orionis ring – a region of anomalous microwave emission (AME), which we aim to examine along with other foreground components. We also direct the telescope towards various astrophysical sources with known features that can be studied and used as, for instance, gain or pointing calibrators. This includes Jupiter, the radio galaxy Cygnus A (Cyg A), as well as the supernova remnants Cassiopeia A (Cas A) and Taurus A (Tau A).

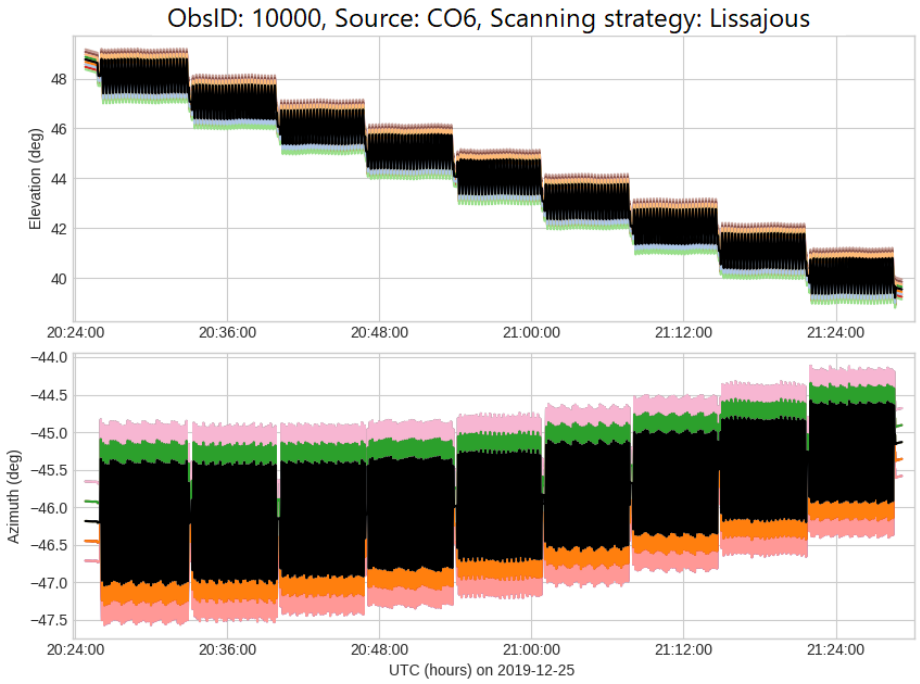

Figure 3.5: Azimuth and elevation as a function of time for an observation of the CO6 field (ObsID 10000), consisting of nine scans during which the telescope is following the Lissajous pattern (each color corresponds to a different feed) [49].

3.2.2 Scanning strategy

After choosing the preferred locations of science fields, it is crucial to determine how the telescope will be scanning these areas of the sky. We define a *scan* as the process taking place between repointing of the dish. Each scan starts with directing the telescope towards the point close to the center of the observed field but located a bit ahead in its path. As the field drifts through, its center approaches and passes this position on the sky. Simultaneously, the telescope is moving in a certain pattern about the originally chosen coordinates (azimuth and elevation). The scan lasts until the field moves past these coordinates (3 to 10 minutes). Thereafter, the dish is repointed to follow the field and the process is repeated, forming a new scan. The sequence of several scans of the same field forms an *observation*, labeled by an identification number called an *ObsID*. An example of an observation consisting of nine scans is shown in Figure 3.5. Every observation contains around one hour of data from each feed of the instrument, starting and ending with calibration vane measurements (more on that in Section 3.3). These data are stored in level 1 files, together with pointing information and housekeeping data, as previously described.

The type of aforementioned pattern, followed by the telescope during a scan, has an impact on the resulting data and can take different forms. The factors to be considered while choosing a scanning strategy include telescope performance, integration efficiency (maximizing the coverage of the field and hitting each pixel as many times as possible), and cross-linking (observing each pixel from different directions to control the systematics). COMAP has been conducting observations employing three different scan types in the beginning, shown in Figure 3.6 – Lissajous, circular and constant elevation scan (CES). Different aspects of data analysis reveal which pattern is preferred (more on that in Part III of the thesis), but currently we switch mostly between Lissajous and CES. The former type tends to result in better crossing and observing efficiency. However, because of the complicated elevation dependence, Lissajous scans produce a varying

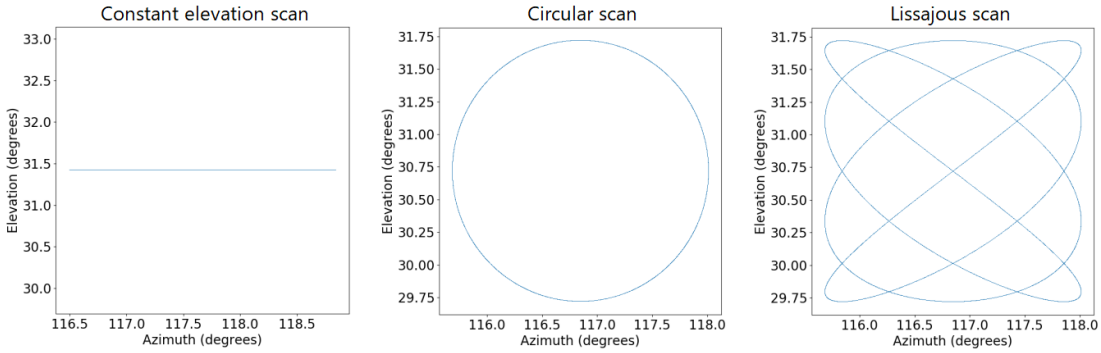

Figure 3.6: Types of scanning strategy employed in COMAP. Illustration shows tracks of constant elevation scan (CES), circular scan, and Lissajous scan as a function of azimuth and elevation for a radius of 1°. Adapted from S. Harper [58].

contribution from the atmosphere and the ground, which makes them more difficult to analyze than constant elevation scans.

While following each scanning pattern, the position of the telescope changes in time according to

$$\text{Azimuth}(t) = A\sin(at + \phi), \tag{3.5}$$
$$\text{Elevation}(t) = B\sin(bt), \tag{3.6}$$

where A and B are parameters defining the dimensions of the observed area, ϕ impacts the phase of the curve creating the scanning pattern, and the ratio between a and b determines its shape. The exact pattern depends on the combination of these parameters. We get a circular scan when $A = B$, $a/b = 1$, $\phi = \pi/2$, whereas a CES results from $b = 0$ (elevation is fixed, so the telescope just moves back and forth in azimuth). In the case of a Lissajous scan, the parameters vary, so that the same pattern is not repeated again and again, which increases the coverage of the observed field.

3.3 The CO Data Analysis Pipeline

The numerical analysis framework was created in order to convert raw data acquired by the instrument (level 1 data) into calibrated and filtered sky maps. The main steps of this pipeline are presented in Figure 3.7, where we show program modules and data files produced along the way. We will refer to this sequence of procedures as the *low-level* data analysis, in contrast to the *high-level* one, taking maps as input data and processing them based on cross spectrum methodology developed in this thesis (Part II). In this section, we will describe each step of the pipeline, explaining the ideas behind filters applied to suppress correlated noise, calibration (converting power readouts from detectors into brightness temperature), data selection, and finally, making maps.

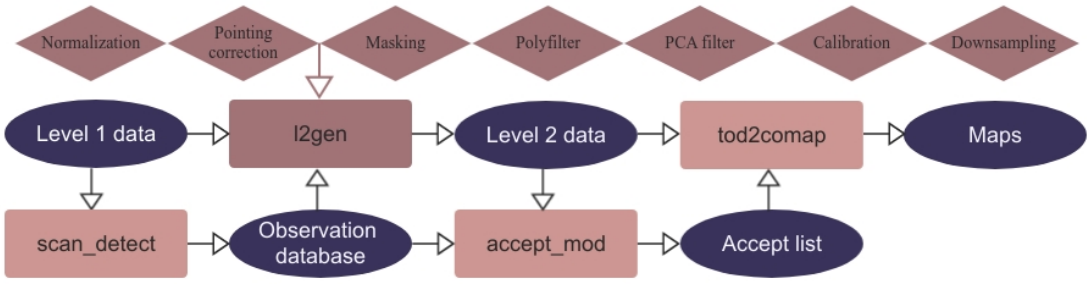

Figure 3.7: Flowchart of (low-level) CO data analysis pipeline – from detector readouts (in level 1 data) to sky maps. The rectangular boxes indicate program modules, whereas the ellipses enclose produced data files. The upper row of diamond-shaped boxes illustrates the stages of the `l2gen` module.

3.3.1 Classification of Level 1 data

As described earlier, each level 1 file contains a single observation (several consecutive scans) with about one hour of time-ordered data (TOD), given as detector readouts in arbitrary digital units. Nevertheless, the stability of associated parameters and effects contributing to the signal is higher in a shorter span of observational time. In addition, working with a smaller quantity of data is simply more efficient computationally. Therefore, we want to perform data analysis independently on each individual scan (3–10 min). The main goal of the first program module, `scan_detect`, is iterating through all level 1 files to classify data and split observations into scans (that are given their own identification number, adding a suffix to the associated ObsID). The output of this process is the *observation database*, sorting all the scans according to the observed target. It also includes additional information, like scanning strategy, pointing parameters, or the modified Julian date (MJD)[1] at the beginning and end of scans.

3.3.2 From Level 1 to Level 2 data

The next step is to convert raw level 1 files into calibrated and filtered level 2 data, using the information from the observation database (given as a *runlist*). This process takes place in the program module called `l2gen`, which also collects diagnostics used for assessing data quality. We will describe the evolution of the TOD as they go through various stages and filtering operations in `l2gen` leading to level 2 files.

Normalization

The level 1 TOD include raw measurements of the power readouts from detectors, P_{out}, described by Equation 3.2. The first procedure applied to these data is normalization of each frequency channel separately, according to

$$d_{\text{norm}} = \frac{P_{\text{out}}}{\langle P_{\text{out}} \rangle} - 1, \tag{3.7}$$

where $\langle P_{\text{out}} \rangle$ is the running mean. In order to compute it, we apply a lowpass filter, multiplying the TOD with the weight function, W, in Fourier space,

$$\langle P_{\text{out}} \rangle = \mathcal{F}^{-1}\{\mathcal{F}\{P_{\text{out}}\}W\}, \qquad W = \left[1 + \left(\frac{f}{f_{\text{knee}}}\right)^{\alpha}\right]^{-1}, \tag{3.8}$$

where $\mathcal{F}$ denotes the Fourier transform, f is the sampling rate (number of time samples per unit time), f_{knee} is the cutoff frequency, chosen to be 0.02 Hz, and $\alpha = 4$. As we can see from Equations 3.2 and 3.7, this process will cancel out both the gain, G, and the system temperature, T_{sys}. We are then left with the normalized data, d_{norm}, fluctuating around zero with the standard deviation given by the radiometer equation (Equation 3.4), $1/\sqrt{\tau\Delta\nu}$, where τ is the sampling period and $\Delta\nu$ is the bandwidth

[1] The modified Julian date (MJD) is a quite commonly used conventional time unit, measuring the number of days since midnight on 17th of November 1858.

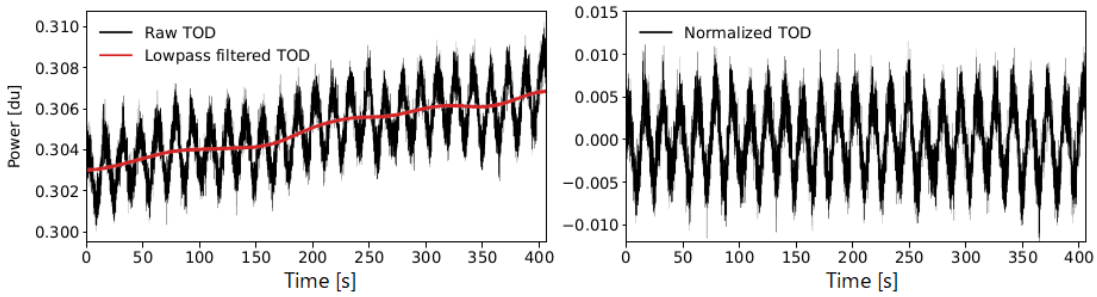

Figure 3.8: Time stream of data before (left panel) and after (right panel) performing the normalization in `l2gen`. Data taken from scan 14456.03, feed 5, at $\sim$ 27.673 GHz. Credit: J. Lunde [50].

of the frequency channel. The data time stream becomes flattened compared to the raw TOD, as can be seen in Figure 3.8. Because all the frequency channels within the sideband are now on the comparable level, it is easier to filter out similar unwanted contributions to the signal amplitude in the later steps.

Removing the pointing template

As described in Section 3.1.4, some signal contributions are correlated with the local coordinates of the target toward which the telescope is pointing. The azimuth position can be associated with the magnitude of the ground signal picked up by the sidelobes of the instrumental beam, whereas the elevation has a direct impact on the thickness of the atmosphere layer that needs to be traversed by the electromagnetic wave to reach the dish. This effect alters the brightness temperature contribution from the atmosphere, modeled as

$$T_{\text{atmosphere}} \approx T_0 \tau(\text{el}), \qquad \tau(\text{el}) = \frac{\tau_0}{\sin(\text{el})}, \tag{3.9}$$

where T_0 is the physical temperature of the atmosphere and $\tau(\text{el})$ is the optical depth of the atmosphere, which is elevation dependent and has value τ_0 at zenith (the point directly above, el $= 90°$). We want to address this problem as a next step after data normalization. Therefore, we fit a data model, incorporating the effects of azimuth and elevation correlated signals, separately for every frequency channel. It takes the following form:

$$d = \frac{g}{\sin(\text{el}(t))} + a\,\text{az}(t) + c + n, \tag{3.10}$$

where g, a, c are constants, with best-fit values determined using the least squares method, and n is Gaussian noise with a constant standard deviation. Thereafter, we remove the pointing template from the data it was fit to,

$$d_{\text{after}} = d_{\text{before}} - \frac{g}{\sin(\text{el}(t))} - a\,\text{az}(t) - \left\langle \frac{g}{\sin(\text{el}(t))} + a\,\text{az}(t) \right\rangle, \tag{3.11}$$

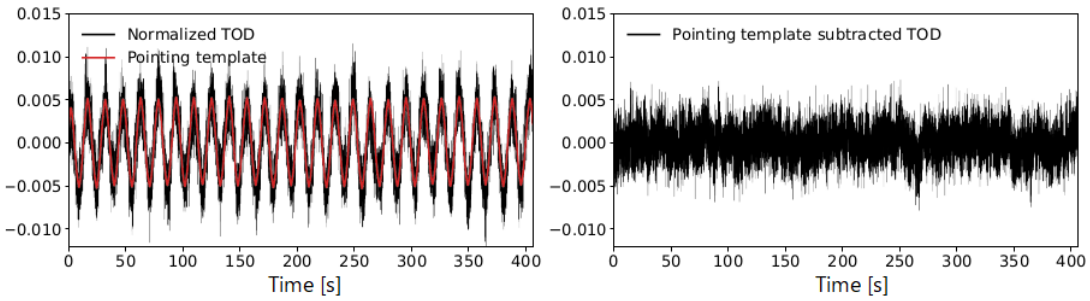

Figure 3.9: Time stream of data before (left panel) and after (right panel) removing the pointing template in `l2gen`. Data taken from scan 14456.03, feed 5, at $\sim$ 27.673 GHz. Credit: J. Lunde [50].

where the last part is the template time average in the given frequency channel, which has to be subtracted in order not to alter the mean of the TOD. The effect that the removal of the pointing template has on the data time stream can be seen in Figure 3.9.

Masking

So far, we have normalized the data and implemented the pointing template correction. It is important to note that at this point we make a copy of the TOD and perform the next stage, polynomial filtering, as well as the subsequent PCA filtering, on this copied set. After that, we use this completely filtered copy of the data to determine the frequency channels that still behave badly, in the sense that they show clear signs of the excess correlated noise. We use this information to mask these frequency channels in the original TOD so that they do not pollute our results, and apply polynomial and PCA filter again – this time to the original masked data set.

There are two strategies when it comes to identifying which frequency channels do not perform as expected and have to be masked out. The first approach is based on searching for the outliers that deviate from the anticipated characteristics of good data. To start with, we know that the polynomial filter introduces a specific form of correlation that needs to be subtracted. After that, we expect good data to exhibit the correlations similar to the ones between two independent Gaussian variables, given by $1/\sqrt{n_{\mathrm{samp}}}$, where n_{samp} is some large number of samples used in this calculation. We look through the correlation matrices for each band, like the one shown in Figure 3.10, and search for the groups of entries that on average differ from our expectations and need to be masked out.

The second method employs a set of diagnostics calculated individually for each frequency channel. We can then perform a comparison between the frequencies with respect to a given feature, searching for the substantial deviations that indicate the channels to be removed. However, if the overall quality of data is not so good, then the bad channels will not stand out as significant outliers to be masked out, which is a clear disadvantage of this approach.

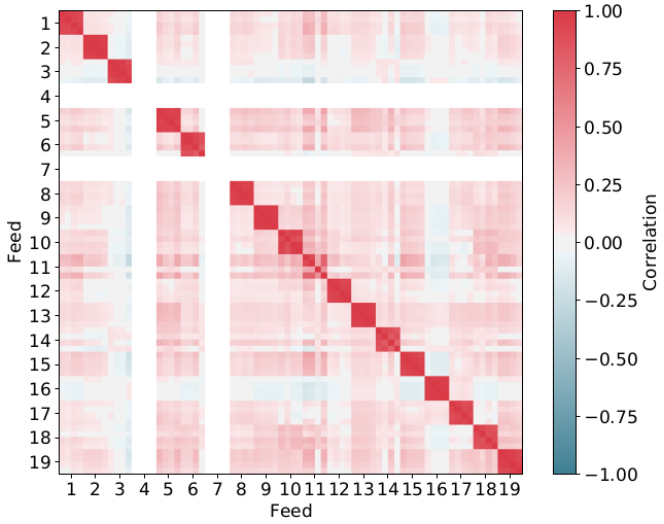

Figure 3.10: Correlation matrix of data from a single CES scan, averaged over a sideband. Credit: H. T. Ihle [47].

Additionally, we want to exclude from further analysis the frequencies largely affected by the so-called aliasing effect. This phenomenon occurs during the signal processing and induces *edge correlations* (the correlations between corresponding frequencies at the edges of sidebands), which also need to be masked out.

Polynomial filter

Now, the third filter can be applied to the original, masked TOD. This procedure is meant to remove the majority of correlated noise contributions that are common to all frequency channels within the sideband. That includes the effects of gain fluctuations in the instrument and varying temperature of the atmosphere, as well as any continuous foreground components. For each time step separately, we fit a model with frequency polynomial across every sideband,

$$d_\nu = a_0 + a_1\nu + a_2\nu^2 + ... + n, \tag{3.12}$$

where a_0, a_1, a_2 are constants found with the least squares approach (usually the polynomial ends up being linear), and n is Gaussian noise with a constant standard deviation. The polynomial fit is subsequently subtracted from the data,

$$d_\nu^{\text{after}} = d_\nu^{\text{before}} - \left(a_0 + a_1\nu + a_2\nu^2 + ...\right). \tag{3.13}$$

This filter has a big impact on the TOD (see Figure 3.11), leaving the data stream being close to white noise.

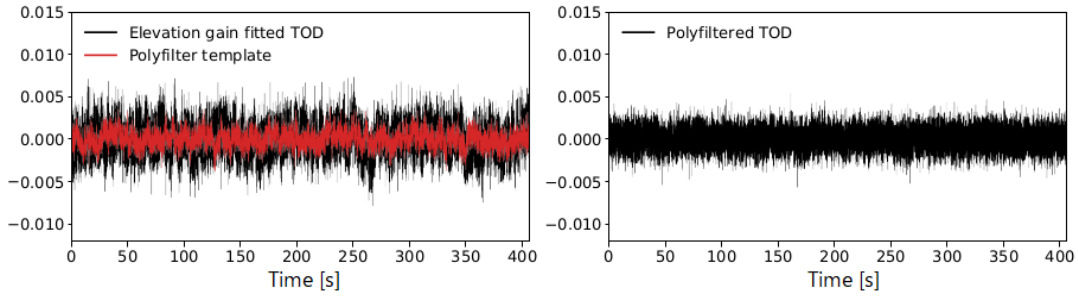

Figure 3.11: Time stream of data before (left panel) and after (right panel) applying the frequency polynomial filter in `l2gen`. Data taken from scan 14456.03, feed 5, at $\sim$ 27.673 GHz. Credit: J. Lunde [50].

As already mentioned, it removes the contributions from astrophysical foregrounds, which are quite stable in the frequency domain. On the other hand, the CO signal that we want to measure varies more rapidly within each sideband (the intrinsic width of CO(1-0) line is close to tens of MHz, which is the scale corresponding to our final frequency channels), so it remains mostly intact. The effect, that the polynomial filter (along with other steps of the pipeline) has on the targeted signal, will be estimated in a transfer function applied to the data in the last stages of the analysis (see Section 4.5.3).

PCA filter

The last filter is designed to suppress correlated noise contributions that are common to all the feeds in the focal plane. Such effects can be caused, for instance, as a result of standing waves forming in various parts of the instrument. In order to address this problem, we perform principal component analysis (PCA) on the entire data set within a given scan, forming a matrix $\mathbf{D}$. Each row in this matrix is then comprised of all the time samples within a single frequency channel, and each column consists of all the frequencies for one time sample. This way, the matrix $\mathbf{D}$ takes the following form:

$$\mathbf{D} = \begin{bmatrix} D_{11} & \dots & D_{1n_{\mathrm{samp}}} \\ \vdots & \ddots & \vdots \\ D_{n_{\mathrm{freq}}1} & \dots & D_{n_{\mathrm{freq}}n_{\mathrm{samp}}} \end{bmatrix}, \tag{3.14}$$

where n_{samp} is the number of time samples ($\sim$ 20 000 for an individual scan) and $n_{\mathrm{freq}} = n_{\mathrm{feeds}} \cdot n_{\mathrm{SB/feed}} \cdot n_{\mathrm{freq/SB}} = 77\,824$ is the total number of frequency channels in all the feeds ($n_{\mathrm{feeds}} = 19$ is the number of feeds, $n_{\mathrm{SB/feed}} = 4$ is the number of sidebands per feed, $n_{\mathrm{freq/SB}} = 1024$ is the number of frequency channels per sideband). We consider the columns of $\mathbf{D}$ (individual time samples) to form a set of random variables.

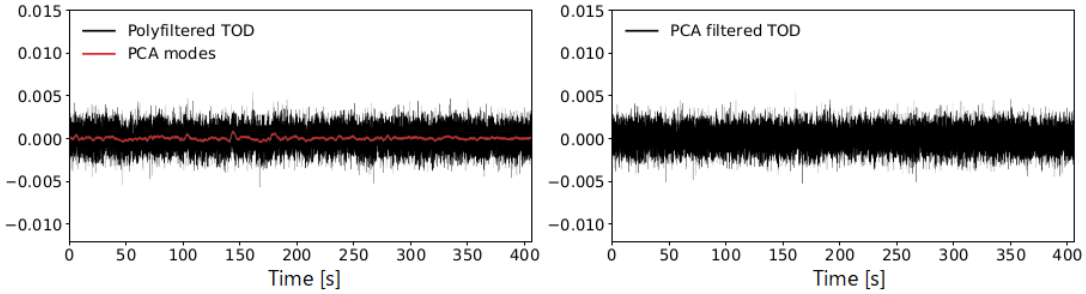

Figure 3.12: Time stream of data before (left panel) and after (right panel) applying the PCA filter in `l2gen`. Data taken from scan 14456.03, feed 5, at $\sim$ 27.673 GHz. Credit: J. Lunde [50].

Then, we can write their covariance matrix as

$$\mathbf{C} \propto \mathbf{D}^{\mathrm{T}}\mathbf{D} = \begin{bmatrix} C_{11} & \dots & C_{1n_{\mathrm{samp}}} \\ \vdots & \ddots & \vdots \\ C_{n_{\mathrm{samp}}1} & \dots & C_{n_{\mathrm{samp}}n_{\mathrm{samp}}} \end{bmatrix}, \tag{3.15}$$

which is subsequently used in the PCA filtering. The main step in this procedure is finding the leading PCA components (or modes), which are the normalized eigenvectors of matrix $\mathbf{C}$, corresponding to the highest eigenvalues, $\vec{v}_k = [v_k^1, v_k^2, ..., v_k^{n_{\mathrm{samp}}}]$. We then compute the PCA amplitudes for all determined PCA components in every frequency channel,

$$a_k = \vec{d} \cdot \vec{v}_k = \sum_{i=1}^{n_{\mathrm{samp}}} d_i v_k^i, \tag{3.16}$$

where $\vec{d} = [d_1, d_2, ..., d_{n_{\mathrm{samp}}}]$ is the vector of time samples within the given frequency channel, that has gone through all the previous stages of data processing (normalization, removal of poiniting template, and polyfilter). The leading PCA modes are some functions of time (each element corresponds to a single time sample), associated with most variance between all the frequencies. Therefore, we want to remove them from the data,

$$\vec{d}_{\mathrm{after}} = \vec{d}_{\mathrm{before}} - \sum_{i=1}^{n_{\mathrm{modes}}} a_k \vec{v}_k, \tag{3.17}$$

where n_{modes} is the number of leading PCA modes to subtract, being usually four. The impact of this filter on the TOD is shown in Figure 3.12. For consistency, we are using here the same data as in Figures 3.8-3.11, but the effect is more prominent in case of data time streams exhibiting stronger signs of standing waves, which are effectively removed by the PCA filter.

Calibration

After the TOD has gone through all the filtering procedures, we can assign specific values of brightness temperature to power readouts originally given by the detectors (in some digital units). This process is called the *calibration*. Due to the initial normalization of the data stream, the noise level in the cleaned TOD should equal $1/\sqrt{\tau\Delta\nu}$, which can be translated into physical units by multiplying with the system temperature, T_{sys} (Equation 3.4). In order to do that, we need to determine the value of T_{sys}. Our approach is based on comparing the power outputs between the measurements conducted with the so-called *hot load* and *cold load* in front of the telescope.

As already mentioned in Section 3.2.2, we start and finish every observation by moving the calibration vane in front of the feedhorn array. We know its temperature (equal to the ambient temperature), T_{hot}, so it can act as a reference hot load. On the other hand, the cold load corresponds to the observations of the sky, with the temperature of the CMB, $T_{\mathrm{cold}} = T_{\mathrm{CMB}}$. The power measurements taken by the telescope when looking consecutively at the hot load, P_{hot}, and the cold load, P_{cold}, can be modeled as in Equation 3.2, including only the contributions to the system temperature that are relevant during these observations. We can then derive the estimate of T_{sys} to be

$$T_{\mathrm{sys}} = (T_{\mathrm{hot}} - T_{\mathrm{CMB}}) \left(\frac{P_{\mathrm{hot}}}{P_{\mathrm{cold}}} - 1 \right)^{-1} . \tag{3.18}$$

For each frequency channel, we calculate T_{sys} from the equation above, interpolating the values of T_{hot} and P_{hot} (measured at the start and the end of the observation) to the time of the currently analyzed scan, and taking the mean power of the scan as P_{cold}. Then, the calibrated data time stream becomes

$$d_{\mathrm{after}} = d_{\mathrm{before}} T_{\mathrm{sys}}. \tag{3.19}$$

Another strategy of performing the calibration is using the astrophysical sources, like Cassiopeia A and Taurus A (or other objects mentioned in Section 3.2.1).

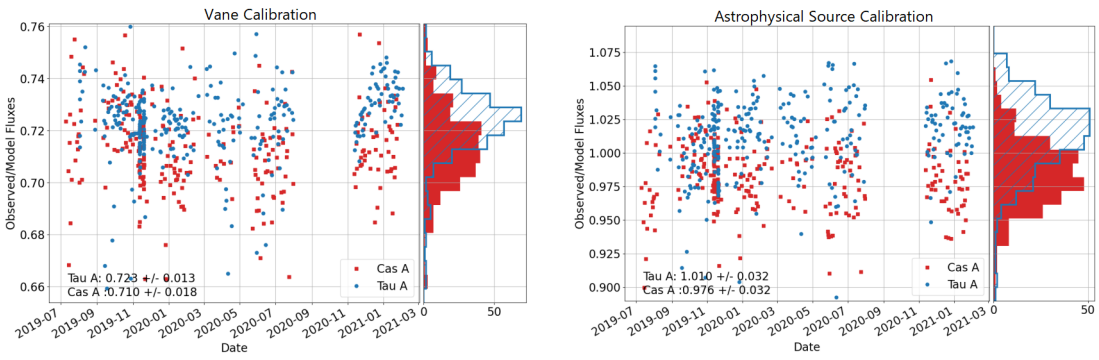

Figure 3.13: Ratios of the observed over expected flux densities for Cassiopeia A (red) and Taurus A (blue) using the vane calibration (left panel) and the astronomical calibration (right panel). Data taken from Feed 1. Credit: S. Harper [59].

We fit the observations into the seven-parameter model of antenna temperature [59], which can subsequently be converted into flux densities. Thereafter, these flux density spectra of bright sources are compared to some theoretical expectations. The ratio between observed and modeled values is used for deriving calibration factors. We employ this approach mostly as a consistency check and verification of the outcomes from the calibration vane measurements. The results associated with both calibration methods are shown in Figure 3.13. It is important to note that the visible difference between them is expected – the ratio of the observed over modeled flux density, determined using only the vane calibration will resemble the instrumental beam efficiency, η_B (see Section 3.1.2), estimated to be ~ 0.7 on average (from Tau A and Cas A observations).

Downsampling

All the above stages of filtering and calibration have been applied to data with full spectral resolution of ~ 2 MHz (1024 frequency channels within a single sideband with the width of 2 GHz). However, such high resolution is not needed for the final maps. Therefore, we want to reduce it, by co-adding several frequency channels together into a single wider channel. Typically, a set of $n = 16$ time streams from adjacent high-resolution frequency channels, $\{d_m^{\text{highres}}, d_{m+1}^{\text{highres}}, ...\}$, results in a single time stream corresponding to a low-resolution channel, d_i^{lowres}, with the 31.25 MHz ($\sim$ 2 MHz $\cdot$ 16) frequency bandwidth. We use the inverse-variance noise weighting in order to combine TOD from several frequency channels,

$$d_i^{\text{lowres}} = \frac{1}{\sum_m w_m} \sum_{m=(i-1)n+1}^{in} w_m d_m^{\text{highres}}, \tag{3.20}$$

where $w_m = \sigma_m^{-2}$ is the inverse variance of TOD in a high-resolution frequency channel m, which is zero if the given frequency happens to be masked out.

After this process, the entire data from the given scan is written to a single level 2 file, which can subsequently be used for mapmaking.

3.3.3 From Level 2 data to maps

Data selection

The output of `l2gen` is a collection of level 2 files with filtered and calibrated data, characterized by white noise properties to a very good extent. Nevertheless, even though we have already masked out some bad frequency channels in `l2gen`, only some portion of these data is accepted for mapmaking and qualifies for further analysis. We reject the parts that still exhibit a high level of systematics, applying data cuts in the program module called `accept_mod`. The output of this process is an *accept list*, indicating parts of the data that are successfully selected to be included in the final maps. Specifically, it is an array of dimensions $n_{\text{scan}} \times n_{\text{feed}} \times n_{\text{SB}}$ (number of scans $\times$ number of feeds $\times$ number of sidebands), with the boolean True or False for the accepted or rejected data, respectively. In addition, the `accept_mod` specifies various splits, distributing the

subsets of data among more maps in the mapmaking process. This is a very important aspect of the final data assessment during the high-level analysis, which will be thoroughly described in Part II.

The data selection is performed according to a large number of diagnostic variables gathered for each element of the accept list. Examples of such statistics include the mean elevation of a scan, the estimated probability of bad weather, or the number of spikes in the data. We set different thresholds for every variable and reject parts of the data that are not within the acceptable limits. These criteria are based on the experience gained throughout the first season of conducting observations and analyzing data. For instance, we decide to accept only observations taken between the elevation of 35° and 65° due to the signs of ground contamination seen in the data.

Mapmaking

Finally, the level 2 data that got through all the cuts can be processed in the mapmaker, `tod2comap`. The main idea behind this procedure is to convert the time-ordered data (TOD) into pixel-ordered data (with right ascension and declination coordinates), using the information about the pointing of the telescope. The time stream of accepted level 2 data can be written as a sum of the signal, $\mathbf{s}$, and the noise (assumed to be Gaussian), $\mathbf{n}$,

$$\mathbf{d} = \mathbf{P}\mathbf{s} + \mathbf{n}, \tag{3.21}$$

where $\mathbf{P}$ is the pointing matrix of dimensions $n_{\mathrm{samp}} \times n_{\mathrm{pix}}$ (number of time samples $\times$ number of pixels in the sky image). This matrix contains values of 1 as the entries for which the corresponding pixel has been observed during the corresponding time sample and zeros otherwise. Because the telescope repetitively scans the fields in an overlapping pattern, it hits the same pixels many times. The large number of hits, n_{hit}, directly translates to the higher total integration time per pixel, τ (n_{hit} multiplied with the duration of time samples), decreasing the noise level (Equations 3.4 and 3.24).

In order to estimate the signal, $\mathbf{s}$, we can write the log-likelihood of the noise component from Equation 3.21, $\mathbf{n} = \mathbf{d} - \mathbf{P}\mathbf{s}$, as

$$\log \mathcal{L} \propto (\mathbf{d} - \mathbf{P}\mathbf{s})^{\mathrm{T}} \mathbf{N}^{-1} (\mathbf{d} - \mathbf{P}\mathbf{s}), \tag{3.22}$$

where $\mathbf{N}$ is the noise covariance matrix. Now, we want to maximize the above expression by setting its derivative to zero and solve for the estimated signal, $\hat{\mathbf{s}}$,

$$\begin{aligned} 0 &= \frac{d}{d\mathbf{s}} (\log \mathcal{L}), \\ 0 &= \mathbf{P}^{\mathrm{T}}\mathbf{N}^{-1} (\mathbf{d} - \mathbf{P}\hat{\mathbf{s}}) + \mathbf{P}\mathbf{N}^{-1} (\mathbf{d} - \mathbf{P}\hat{\mathbf{s}})^{\mathrm{T}}, \\ \hat{\mathbf{s}} &= \left(\mathbf{P}^{\mathrm{T}}\mathbf{N}^{-1}\mathbf{P}\right)^{-1} \mathbf{P}^{\mathrm{T}}\mathbf{N}^{-1}\mathbf{d}. \end{aligned} \tag{3.23}$$

We can assume that various filtering and masking procedures performed in the COMAP analysis pipeline until this point have left only uncorrelated white noise in the data. Therefore, $\mathbf{N}$ is a diagonal matrix, with entries on the diagonal equal to the values of

noise variance corresponding to different time samples, σ_t^2. The signal, $\hat{s}_{\rm pix}$, and noise variance, $\sigma^2_{\rm pix}$, for a single pixel are then given by

$$\hat{\mathbf{s}}_{\rm pix} = \sigma^2_{\rm pix} \sum_{t=0}^{n_{\rm hit}} \sigma_t^{-2} d_t, \qquad \sigma^2_{\rm pix} = \left(\sum_{t=0}^{n_{\rm hit}} \frac{1}{\sigma_t^2} \right)^{-1}, \tag{3.24}$$

where we sum over all the time samples, d_t, connected to the given pixel. Because of such inverse-variance weighting, we put less weight on the samples with a higher noise level.

The end products are the three-dimensional maps of brightness temperature for each of the three science fields. We show a single frequency slice of such maps, containing all the accepted data, in Figure 3.14. We can see that they are dominated by white noise (our observing strategy yields a larger number of pixel hits in central regions, so the fluctuations there are closer to zero than at the edges).

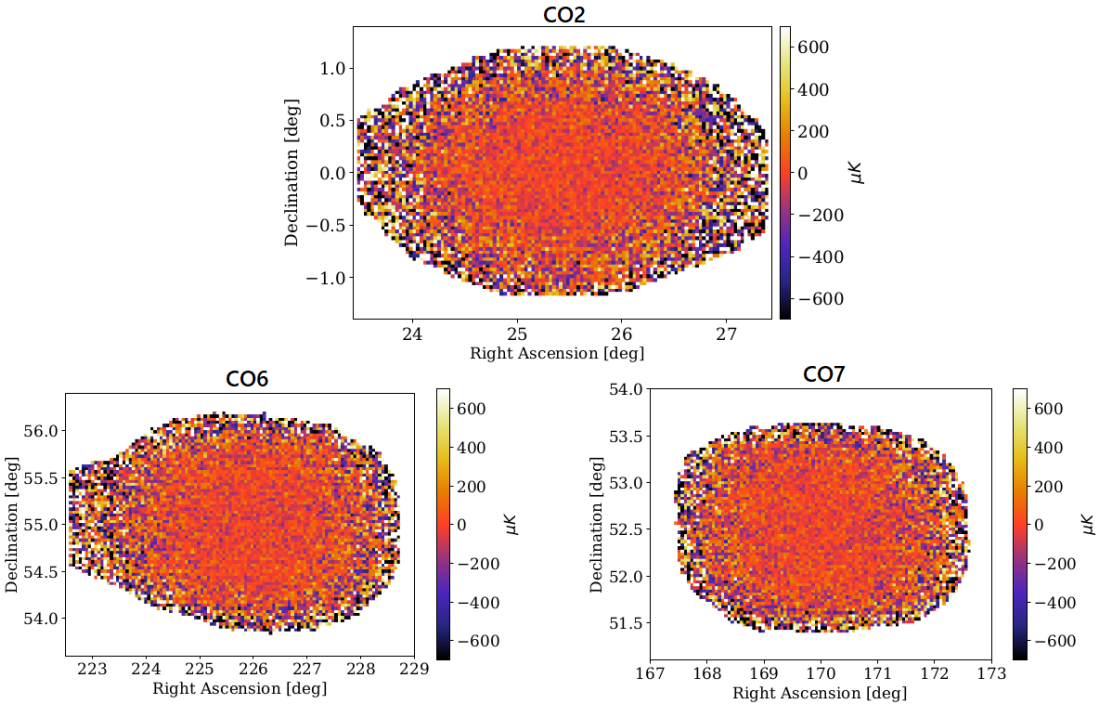

Figure 3.14: Maps of three main science fields – CO2 (top), CO6 (bottom left), and CO7 (bottom right). These maps correspond to a single frequency at 32 GHz (with the bandwidth of 31.25 MHz) and contain all the accepted data that are subsequently averaged over the feeds. Credit: N. Stutzer.

Part II

Methods

Chapter 4

High-level data analysis

Signal estimation and data quality assessment with cross spectra

The COMAP analysis pipeline, presented in the previous chapter, performs the low level data processing, producing sky maps out of raw data provided by the instrument. Currently, our maps are white noise dominated (see Figure 3.14), but the end goal is to detect the signal fluctuations of CO line emission. A simulation, showing how a map of this kind may look like, is illustrated in Figure 4.1. It is important to be able to interpret such line intensity maps in order to extract cosmological and astrophysical information. We have presented this concept in Section 2.4, where we introduced two quantities that can be used to characterize the statistical properties of the observed field – the power spectrum and the voxel intensity distribution (VID). The primary observable used in COMAP is the power spectrum. At the current stage of the experiment, it is a very useful tool for assessing the quality of data, in addition to estimating the signal amplitude

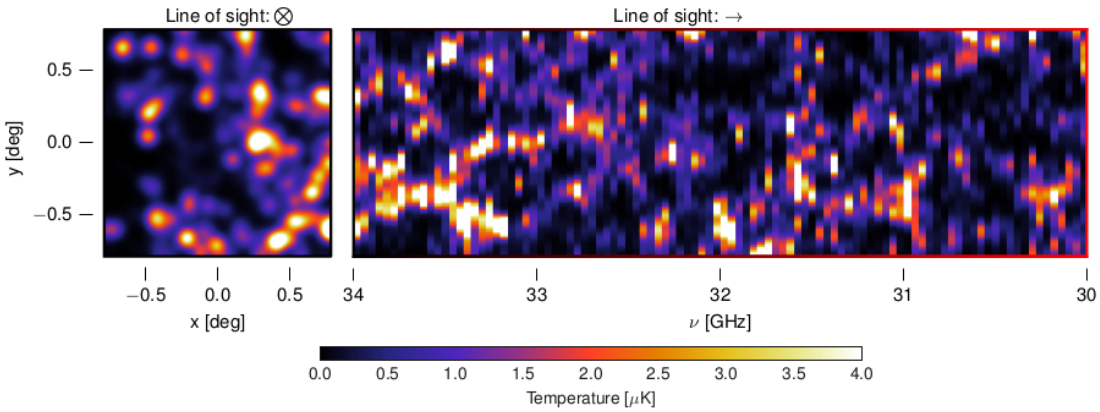

Figure 4.1: CO intensity map obtained from simulations, where the front view in the highest frequency slice is shown on the left image and the side view across the frequencies between 34 and 30 GHz (or redshifts $\sim$ 2.4–2.8), on the right. Adapted from [42].

from the maps and comparing with various theoretical predictions. In this chapter, we will describe the numerical framework developed for these applications, illustrated in Figure 4.2. We will explain how we account for the signal modification caused by low-level data processing and instrumental effects (transfer functions), in addition to presenting the ideas and motivation behind the cross spectrum methodology, which is the foundation of high-level data analysis in COMAP. Most of the theoretical information provided here is also covered in our article to be published as a part of the series associated with the first season of COMAP's operations [60].

4.1 Power Spectrum

In order to describe the statistical properties of the observed field, we can compute its power spectrum, $P(\vec{k})$, which indicates the spread in the corresponding distribution. Specifically, it measures the amplitude of fluctuations as a function of physical length scale, $L \approx 2\pi/k$, where $k = |\vec{k}|$ is the comoving wave number. If there are strong variations in the given region, the value of power spectrum is large, whereas if the field is smooth, the power spectrum is small [13, 14]. Even for the fields that are not perfectly Gaussian, it provides a lot of valuable information of cosmological and astrophysical importance (see Section 2.4). The power spectrum of our maps can be compared to various theoretical models in order to extract this information. These models do not predict the specific locations of CO emitters, but the general statistical features of their distribution. A given CO intensity map is then only a single realization of the field characterized by its power spectrum. In addition, computing $P(\vec{k})$ reduces the content of the maps to some small number of data points, which makes them easier to interpret.

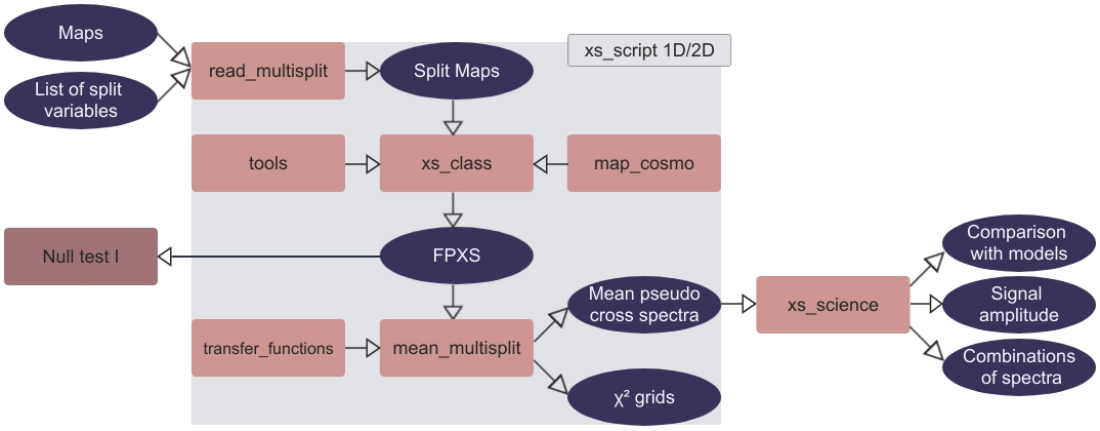

Figure 4.2: Flowchart of the cross spectrum pipeline – from maps to cross spectra averaged over many split maps used for inference. The rectangular boxes indicate program modules, whereas the ellipses contain their products. The gray area encloses the steps performed within a single run of the `xs_script`, importing different modules and producing either 2D or spherically averaged 1D spectra.

4.1.1 Conventions

The spherically averaged power spectrum of a three-dimensional map can be calculated as

$$P(\vec{k}) = \frac{V_{\rm vox}}{N_{\rm vox}} \langle |f_{\vec{k}}|^2 \rangle, \tag{4.1}$$

where $V_{\rm vox}$ is the volume of a single voxel in the map, $N_{\rm vox}$ is the total number of voxels, and $\vec{k}$ is the wave vector corresponding to a Fourier mode $f_{\vec{k}}$. The calculation of Fourier components follows the standard convention of the three-dimensional discrete Fourier transform,

$$f_{\vec{k}} = \sum_{\vec{n}=0}^{\vec{N}-1} x_{\vec{n}} \exp\left(-i2\pi\vec{k}\cdot\frac{\vec{n}}{\vec{N}}\right), \qquad \begin{aligned} \vec{k} &= [k_x, k_y, k_z], \\ \vec{n} &= [n_x, n_y, n_z], \\ \vec{N}-1 &= [N_x-1, N_y-1, N_z-1], \end{aligned} \tag{4.2}$$

where $x_{\vec{n}}$ gives the value assigned to a voxel of the map in real space, with indices $\vec{n} = [n_x, n_y, n_z]$, and $\vec{N}$ gives the number of voxels in each direction, so that $N_x N_y N_z = N_{\rm vox}$ is the total number of voxels in the map ($120 \cdot 120 \cdot 256$ in our maps). The physical components of the wave vector are then defined as

$$k_x \equiv \frac{2\pi M_x}{\Delta x N_x}, \qquad M_x \in \{-N_x/2, ..., -1, 0, 1, ..., N_x/2\}, \tag{4.3}$$

where Δx is the size of a single voxel in x-direction, so that its comoving volume is $\Delta x \Delta y \Delta z = V_{\rm vox}$ ($\sim$ 56 Mpc^3 in our maps). We calculate the remaining components (k_y, k_z) analogously. When we are looking at the spherically averaged power spectrum in one dimension, the magnitude of wave vector (wave number) becomes $k \equiv \sqrt{k_x^2 + k_y^2 + k_z^2}$. Nevertheless, usually we want to distinguish between the angular directions of the map (x and y coordinates) and the line-of-sight direction, established through frequency dependence (z coordinate). Therefore, the power spectrum is typically given in terms of perpendicular modes, $k_\perp$, and parallel modes, $k_\parallel$, where

$$k_\perp \equiv \sqrt{k_x^2 + k_y^2}, \qquad k_\parallel \equiv |k_z|. \tag{4.4}$$

4.1.2 Auto spectrum versus cross spectrum

Equation 4.1 gives the variance of Fourier components of a single map, which is called the *auto spectrum*. On the other hand, the covariance between the Fourier components of two different maps is quantified by the *cross spectrum*. It takes the following form:

$$C(\vec{k}) = \frac{V_{\rm vox}}{N_{\rm vox}} \Big\langle {\rm Re}\{f^*_{1,\vec{k}} f_{2,\vec{k}}\} \Big\rangle, \tag{4.5}$$

where $f_{1,\vec{k}}$ and $f_{2,\vec{k}}$ are the Fourier components of the two maps, * indicates the complex conjugate, and Re{} denotes the real part. The conventions introduced in Section 4.1.1

hold here as well. We can see that if the two maps are the same, the form of the equation above becomes identical to the auto spectrum.

We based the high-level data analysis in COMAP on the methodology associated with the cross spectrum, not the auto spectrum. In order to explain the motivation behind that, we first write the auto spectrum of a given map as a sum of two components – signal and noise,

$$P(\vec{k}) = P_{\text{signal}}(\vec{k}) + P_{\text{noise}}(\vec{k}). \tag{4.6}$$

Since we are interested in extracting the signal component from the computed power spectrum, we first need to know how to effectively find the estimate of the noise. In order to make this task easier, we can neglect the contributions from foregrounds and correlated noise, which are assumed to be insignificant due to masking and filtering procedures applied during the low-level data processing. Then, the noise level in each voxel can be modeled as uncorrelated white noise,

$$P'_{\text{noise}} = V_{\text{vox}}\sigma_N^2, \tag{4.7}$$

where σ_N is the standard deviation given by the previously introduced radiometer equation (Equation 3.4). Here, we have also assumed that the noise is uniform over the entire map, so that the above power spectrum component does not depend on $\vec{k}$. With the noise estimate, we can rewrite Equation 4.6 to extract the signal from the measured power spectrum,

$$P_{\text{signal}}(\vec{k}) \approx P(\vec{k}) - P'_{\text{noise}}. \tag{4.8}$$

However, all of the applied simplifications make the noise estimate quite uncertain. Even if the model includes more complicated effects and assumptions, it has to be extremely precise since every error will directly pollute the estimate of the signal. This task may be very challenging, especially because the targeted signal is so weak ($\sim \mu$K) and sensitive to such effects.

Nevertheless, this problem can be avoided with the cross spectrum methodology if we only make sure that any residual systematics have independent contributions to the maps. When we use two independent maps in the calculations (Equation 4.5), their random noise content cancels out in the cross spectrum (uncorrelated components do not contribute to the mean), leaving only the common factors, which ideally include purely the signal component,

$$C(\vec{k}) = P_{\text{signal}}(\vec{k}). \tag{4.9}$$

Therefore, we do not have to estimate the noise in order to extract the signal power spectrum. The noise content of the maps is still important since it contributes to the variance of cross spectrum measurement. However, the evaluation of this effect requires less precision than in the case of auto spectrum analysis because it does not directly impact the signal estimation, only its uncertainty.

Despite the big advantage of excluding the noise component from precision analysis, the cross spectrum methodology has its own challenges. The main problem is that we lose some of the intrinsic sensitivity compared to the auto spectrum since the whole data set has to be split into two maps to be used for cross-correlation. We can, however,

suppress this effect by splitting data into even more independent maps, computing the cross spectra of all possible combinations of map pairs, and averaging them at the end (which is the idea behind the feed-feed pseudo cross spectrum method, described in Section 4.4). In general, the sensitivity of cross spectrum derived this way depends on the number of split maps, N_{split},

$$\sigma_c(N_{\text{split}}) \geq \sqrt{\frac{1}{1 - 1/N_{\text{split}}}}\sigma_P, \tag{4.10}$$

where σ_P is the sensitivity of the auto spectrum, computed from all the data (the equality holds if the field coverage of the maps is identical). From the above equation, we can see that when the number of splits goes to infinity, we approach the sensitivity associated with the auto spectrum. It is therefore beneficial to distribute data between many maps for the cross spectrum analysis. The additional advantages and criteria of this procedure will be discussed in the next section.

4.2 Map splits

In Section 3.3.3, we have briefly mentioned that the `accept_mod` specifies various criteria according to which the data are divided in the mapmaker called `tod2comap`. Specifically, the data set is split into two parts containing an equal number of scans, so that the mapmaking process is thereafter performed independently for each part. We can, for instance, separate Lissajous scans from constant elevation scans (CES), or the data acquired during the first half of the mission from the ones obtained during the second half of COMAP's operations. These examples, along with more variables that can be used for this purpose, are gathered in Table 4.1. The process of dividing data in this

Label	Description	Label	Description
`cesc`	Scanning strategy: Lissajous vs CES	`rise`	Field movement: setting vs rising
`elev`	Mean elevation: lower vs higher	`half`	Half-mission: 1st vs 2nd half of operations
`ambt`	Ambient Temperature: lower vs higher	`odde`	ObsID: odd vs even number
`wind`	Wind speed: lower vs higher	`fpol`	Cutoff frequnecy in polyfilter: higher vs lower value
`wint`	Season: closer vs further from winter	`dayn`	Time of day: day vs night (closer to 2 AM)

Table 4.1: Examples of variables according to which the data set may be split into more maps.

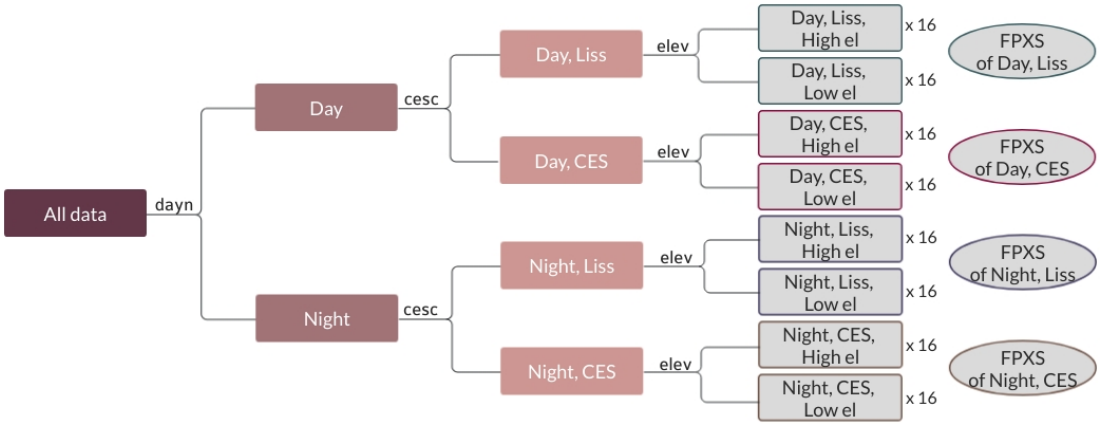

Figure 4.3: Example of splitting data into several maps with `dayn` as test variable, `cesc` as control variable, and `elev` as both control and cross variable. Every final pair consists of two sets of 16 maps (one map per unmasked feed), whose combinations are used to compute feed-feed pseudo cross spectra (FPXS).

way can be conducted multiple times. The output from the mapmaker is then a multidimensional array, containing maps made out of data split according to various variables. An array of dimensions $8 \times 19 \times 4 \times 64 \times 120 \times 120$ is then the product of splitting data in half three times prior to mapmaking ($2 \cdot 2 \cdot 2 = 8$), containing 19 feeds, each with 4 sidebands, each with 64 frequency channels, and $120 \cdot 120$ points on the spatial grid (in x and y direction).

In order to further process these maps, we need to know what kinds of variables have been used as criteria for splitting. Therefore, every multidimensional map enters the cross spectrum pipeline with an associated list of split variables, which is read and interpreted in the program module called `read_multisplit` (see Figure 4.2). Its goal is to identify the maps and redistribute them among subsets defined by different combinations of variables. The list gives all the variables in the proper order so that we can connect a particular split to the correct array dimension. In addition, the variables are assigned by a number to one of the two categories, determining the way we further process the maps. These categories include *test variables*, which do not mix with remaining variables of this kind (i.e. we only look at one of them at the time, while the rest is co-added), and *control variables*, for which we want to produce all the possible combinations with other variables (this is usually something that we always want to analyze separately, like data obtained using different scanning strategies). In addition, some features may be marked out to become *cross variables*. These are the factors that differ in the map pairs used for calculating the cross spectra (Equation 4.5). For instance, one map for which we calculate Fourier components, $f_{1,\vec{k}}$, might come from observations taken below the median elevation, and another map, giving $f_{2,\vec{k}}$, from observations conducted at higher elevations (so that the problematic elevation-correlated signal residuals, like ground pickup, cancel out in such computation).

The output products of `read_multisplit` contain properly formed maps with subsets of data that are processed independently through the next stages of the cross spectrum pipeline (for instance, in Figure 4.3 we have four of them – only daytime data with Lissajous scans, only daytime data with CES, only nighttime data with Lissajous scans, and only nighttime data with CES). This way, we can assess the quality of data and possibly identify some issues that are connected to the particular combination of variables. Every product is an array of dimensions $2 \times 19 \times 4 \times 64 \times 120 \times 120$, where the first dimension gives a pair of map sets divided according to a cross variable. Each of these two sets is then comprised of 19 maps (one map of dimensions $4 \times 64 \times 120 \times 120$ per feed).

4.3 From maps to pseudo cross spectra

The map pairs separated for cross-correlation are processed by the `xs_class`. Here, we will describe the stages of this computation, converting two maps into a single pseudo cross spectrum. The procedures analogous to the methods presented in this section can be applied also to the auto spectrum analysis (if we use two maps that are the same), for instance when we estimate transfer functions (more on that in Section 4.5).

4.3.1 Converting to a cosmological map grid

The first step is to create map objects out of both three-dimensional temperature maps given as an input. This process is conducted in the imported module called `map_cosmo`. At this point, both maps have the angular resolution of $\Delta\theta = 2'$ and the spectral resolution of $\Delta\nu = 31.25$ MHz. We want to convert these voxel dimensions into the comoving distances (with the units of Mpc) in perpendicular direction (Δx along right ascension and Δy along declination) and line-of-sight direction (Δz). First of all, we change the shape of the maps, going from four sidebands into a single frequency axis, so that we get a rectangular grid of dimensions $120 \times 120 \times 256$ ($N_x \times N_y \times N_z$). As already described in the previous chapter, our frequency coverage spans the range between 26 and 34 GHz. The light from CO(1-0) line, emitted in rest-frame at $\nu_0 \approx 115.27$, falls into this range from the redshift slice $z = 2.4 - 3.4$.

The comoving distance between two events happening at the same redshift z, but with an angular separation on the sky $\Delta\theta$, can be found as

$$\Delta D_\perp = \Delta\theta \, r(z) = \Delta\theta \int_0^z \frac{c \, dz'}{H(z')} \approx \Delta\theta \, r(z_{\mathrm{mid}}), \tag{4.11}$$

where c is the speed of light and $H(z')$ is the Hubble parameter at redshift z' [61]. We assume that all the voxels in the map have the same size as the middle one, so the above calculation is performed only for $z = z_{\mathrm{mid}} \approx 2.9$ in order to find the factor $r(z_{\mathrm{mid}})$, converting angular separation in degrees to comoving length in Mpc. We then

find the voxel dimensions in x and y direction to be

$$\begin{aligned}\Delta x &= \Delta\theta\; r(z_{\mathrm{mid}}) \cos\Big(\frac{\pi}{180^\circ}\langle \mathrm{DEC}\rangle\Big),\\ \Delta y &= \Delta\theta\; r(z_{\mathrm{mid}}),\end{aligned} \tag{4.12}$$

where the mean declination, $\langle \mathrm{DEC}\rangle$, is used to account for the effect of compression along the x direction as we move towards the poles (circles of latitude getting smaller).

When it comes to the line-of-sight direction, first we convert the frequency channels of width $\Delta\nu$ into the redshift intervals $\Delta z'$ (marked by $'$ to distinguish from the comoving length of voxels in z direction, Δz). We want to establish the small difference between some redshift z_1, for which the CO(1-0) line shifts the frequency from emitted ν_0 to observed ν_1, and redshift z_2, with the corresponding observed frequency ν_2. Using Equation 1.2, we find that it takes the following form (for $z_1 > z_2$):

$$\Delta z' = z_1 - z_2 = \frac{\nu_0}{\nu_1} - \frac{\nu_0}{\nu_2} \approx \frac{(1+z_{\mathrm{mid}})^2 \Delta\nu}{\nu_0}. \tag{4.13}$$

We then go from the frequency axis to the redshift axis, with values spaced equally by intervals $\Delta z'$ from $z_{\mathrm{mid}} - 256\Delta z'/2$ to $z_{\mathrm{mid}} + 256\Delta z'/2$ ($z \approx 2.4 - 3.4$). The comoving radial distance, travelled by light between redshifts z_1 and z_2, is

$$\Delta D_{\parallel} = \int_{z_2}^{z_1} \frac{c\,dz}{H(z)} \approx \frac{c\,\Delta z'}{H(z_{\mathrm{mid}})}, \tag{4.14}$$

which becomes the conversion factor between the redshift values and the comoving length of voxels along the line-of-sight direction.

Following this methodology (with the assumption that all the voxels are the same), the comoving volume of a single voxel in our three-dimensional maps becomes

$$V_{\mathrm{vox}} = \Delta x \Delta y \Delta z \approx 3.63\ \mathrm{Mpc} \cdot 3.63\ \mathrm{Mpc} \cdot 4.26\ \mathrm{Mpc} \approx 56.07\ \mathrm{Mpc}^3. \tag{4.15}$$

4.3.2 Computing pseudo cross spectrum

After the grids of both temperature maps, m_1 and m_2, got converted to physical comoving dimensions and became the objects of the `xs_class`, we can calculate the cross spectrum of them. As already mentioned (see Section 4.1.1), this result can be either spherically averaged to one dimension (so that $k = |\vec{k}|$) or decomposed into two dimensions (with $k_\perp$ and $k_\parallel$). We will follow the 1D methodology and notation, but the entire implementation is completely analogous in 2D.

We estimate the value of cross spectrum for a given set of k-bins, effectively degrading k-resolution to 14 logarithmically spaced intervals $\{k_i\}$ (in 2D we would define separate sets of $k_\perp$-bins and $k_\parallel$-bins). Equation 4.5 gets then translated to

$$C(k_i) \approx \frac{V_{\mathrm{vox}}}{N_{\mathrm{vox}} N_{\mathrm{modes}}} \sum_{j=1}^{N_{\mathrm{modes}}} \mathrm{Re}\{f^*_{1,k_j} f_{2,k_j}\} \equiv C_{k_i}, \tag{4.16}$$

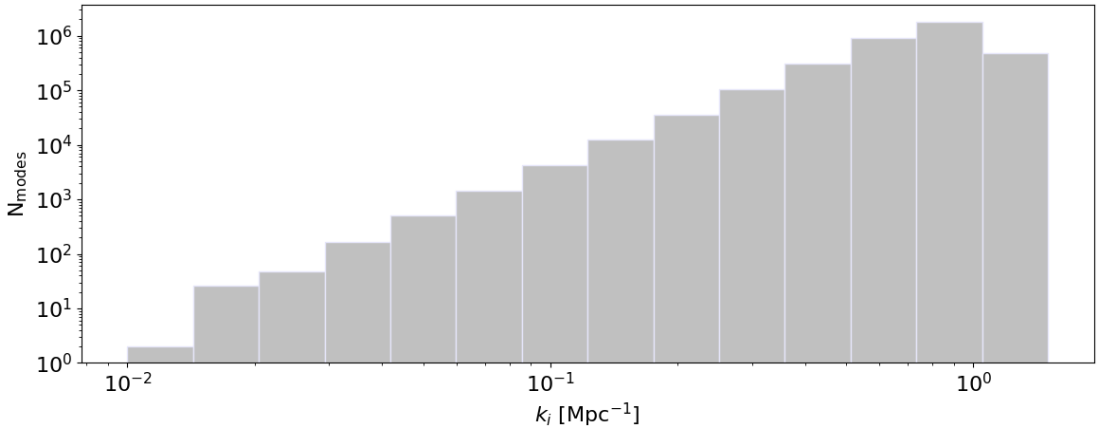

Figure 4.4: Histogram showing the number of Fourier modes, N_{modes}, in the set of 14 logarithmically spaced k-bins, $\{k_i\}$, used for pseudo cross spectrum calculation.

where N_{modes} is the number of Fourier components in the bin k_i and C_{k_i} is the estimated value of cross spectrum in that bin. The number of Fourier modes that can be computed from a given map is limited, and this becomes the intrinsic source of uncertainty, contributing to the total uncertainty of the signal measurement conducted based on a single map (auto spectrum) or a map pair (cross spectrum). This is called the sample variance and takes the following form:

$$\sigma_c^2(N_{\text{split}}) \geq \frac{1}{1 - 1/N_{\text{split}}} \sigma_P^2 = 2 \left\langle (P_{k_i} - P(k_i))^2 \right\rangle \approx 2 \frac{P(k_i)^2}{N_{\text{modes}}}, \tag{4.17}$$

where we used the relation between the sensitivity of the cross spectrum computed from the data set split into $N_{\text{split}} = 2$ maps and sensitivity of auto spectrum derived from the entire data set, as in Equation 4.10 (if the Fourier components are independent Gaussian variables, the last approximation becomes exact). The specific number of Fourier modes varies between the k-bins, as shown in Figure 4.4. Following [42], for a given bin, the number of modes depends on its width, Δk, and associated scale of fluctuations, k, but also on the volume of the field observed by the experiment, V_{surv},

$$N_{\text{modes}}(k, \Delta k) \approx \frac{k^2 \Delta k V_{\text{surv}}}{4\pi^2}. \tag{4.18}$$

This means that the obtainable number of modes can be increased if we observe larger areas of the sky, thereby reducing the uncertainty associated with the sample variance. However, for now, the instrumental noise is a more problematic contribution. That is why we choose to observe smaller fields but for a longer time, so that the instrumental noise can integrate down (Equation 3.4). As in the current phase of the project this source is clearly dominating, we also neglect the sample variance while estimating the error bars associated with the signal measurement.

The issue that we need to address, is the fact that the noise present in the maps is not uniformly distributed over the entire field. Some parts of the maps exhibit higher noise levels than the others and thus have a larger impact on the noise power spectrum. Therefore, we want to put less weight on the map areas with higher noise levels before computing the cross spectrum. We weight both maps with the same factor,

$$w_{1,2} = \mathcal{N}\frac{1}{\sigma_{m_1}\sigma_{m_2}}, \tag{4.19}$$

where σ_{m_1} and σ_{m_2} are noise level maps associated with both temperature maps (these are also the outputs of the mapmaker, computed following Equation 3.24), with some voxels having very high noise levels masked out by setting $1/\sigma_m$ to zero. The normalization constant, $\mathcal{N}$, is defined as

$$\mathcal{N} = \left(\left\langle \frac{1}{\sigma_{m_1}^2\sigma_{m_2}^2} \right\rangle\right)^{-1/2}, \tag{4.20}$$

where the average is taken over entire maps. The cross spectrum computed out of the weighted maps, $\widetilde{m}_1 = w_{1,2}m_1$ and $\widetilde{m}_2 = w_{1,2}m_2$, is called the pseudo cross spectrum, $\widetilde{C}_{k_i}$. We need to note that this process of weighting the maps leads to so-called *mode mixing*, which occurs when different Fourier components of the map leak to the wrong k-bins, so that the measured signal power spectrum slightly deviates from the true signal. Although this effect hinders comparison between our results and theoretical predictions, it can be estimated and taken into account if needed, since we exactly know how the maps were initially altered by the weighting procedure. For instance, we can examine the impact of mode mixing by generating many three-dimensional map simulations, containing only some modeled signal (more on that in Section 4.5.1), and then comparing their pseudo auto spectra to auto spectra calculated from maps that have not been noise-weighted.

4.3.3 Estimating the uncertainty

In addition to calculating the pseudo cross spectrum for the given pair of maps, $\widetilde{C}_{k_i}$, we want to assess its uncertainty in each k-bin, $\sigma_{\widetilde{C}_{k_i}}$. As mentioned previously (see Section 4.1.2), this is connected to estimating the spectrum of the noise content present in the maps. Due to employing the cross spectrum methodology, any error made during the noise evaluation will not directly impact the measured signal, only the error bars associated with this measurement. That is why the approach we take does not require extremely high precision. Again, we assume that all the correlated noise contributions have been sufficiently suppressed by the low-level data analysis, so that the maps contain only uncorrelated white noise. Our method is then based purely on simulations of such white Gaussian noise. The process goes as follows:

- We perform simulations of two maps, r_1 and r_2, with the same shapes as the original temperature maps for which we computed the pseudo cross spectrum, m_1 and m_2. The simulated maps are comprised only of random Gaussian noise.

Specifically, we draw random samples for each voxel in r_1 and r_2 from the Gaussian distribution with zero mean and the standard deviation given by the corresponding noise level maps (σ_{m_1} for r_1 and σ_{m_2} for r_2).

- We compute pseudo cross spectrum based on the simulated maps, which are weighted in the same way as the temperature maps, $\widetilde{r}_1 = w_{1,2} r_1$ and $\widetilde{r}_2 = w_{1,2} r_2$.
- The steps above are repeated N_{sim} times (currently we generate $N_{\mathrm{sim}} = 50$ simulations), gathering the results.
- We take the standard deviation in each k-bin of all pseudo cross spectra computed from the simulated maps, $\sigma_{\widetilde{C}_{k_i}}$. This results in 14 error bars (one per associated k-bin), representing the uncertainty of the signal pseudo power spectrum measurement, caused by the white noise contribution.

4.4 Combining pseudo cross spectra – FPXS method

Finally, we can incorporate all the procedures explained in the previous sections into one analysis framework called the *Feed-feed Pseudo CROSS Spectrum* (FPXS) method. This is the main approach used in COMAP to estimate the signal power spectrum from the three-dimensional temperature sky maps. As mentioned in Section 4.1.2, we can improve the sensitivity of this measurement by splitting the data set into more independent maps, computing pseudo cross spectra of all the combinations of map pairs, and finally combining them. In addition, this procedure lowers the susceptibility of our estimate to various experimental systematics. This is exactly the premise of the FPXS method.

Following the process of dividing data into many parts, described in Section 4.2, we get some subsets of data, which are treated independently moving forward. Each subset is represented by an array of dimensions $2 \times 19 \times 4 \times 64 \times 120 \times 120$, where the first index corresponds to the split in two according to some cross variable. For instance, this can be elevation, as shown in Figure 4.3. One set, S_a, contains then only data from observations taken at a lower elevation, and another set, S_b, has only higher elevation data. Each of these two disjoint sets comprises 19 maps (of dimensions $4 \times 64 \times 120 \times 120$), where every map is assigned to a single feed. In practice, we exclude three of the problematic detector chains from the analysis (feed 4, 6, and 7), so that we effectively have 16 independent maps per set. We find all the possible combinations between these feed-maps, giving $16 \cdot 16$ map pairs, where one map in each pair always comes from S_a and another map from S_b. Then, we compute pseudo cross spectra for every one of them, following the methods from Section 4.3. This process is parallelized so that the cross spectrum calculation happens simultaneously for some number of map pairs, which decreases the total time of computation.

After this operation is completed, we want to combine the produced pseudo cross spectra, which takes place in the program module called `mean_multisplit`. Nevertheless, not all of them are included in the mean. First of all, we reject all pseudo cross spectra computed from the map pairs for which both maps correspond to the same

feed. This way, we reduce the impact of instrumental systematics that are associated only with a given feed. Moreover, we want to exclude spectra that still exhibit some stronger residual correlations. This is assessed by computing the χ^2 statistic for each pseudo cross spectrum,

$$\chi^2 = \sum_{i=1}^{N_k} \left(\frac{\widetilde{C}_{k_i}}{\sigma_{\widetilde{C}_{k_i}}} \right)^2, \tag{4.21}$$

where N_k is the number of k-bins (in our case $N_k = 14$). At this stage of the experiment, we expect the pseudo cross spectrum to be distributed approximately as white noise so that

$$\frac{\chi^2 - N_k}{\sqrt{2N_k}} \sim \mathcal{N}(\mu = 0, \sigma^2 = 1). \tag{4.22}$$

We then want to reject all the spectra that show signs of excess power, significantly deviating from the white noise. Therefore, we compute the absolute value of the characteristic above and exclude all the feed combinations for which it is larger than 5. We can investigate further to find particular split maps or feed combinations that seem problematic, by performing principal component analysis (PCA) on the entire set of the computed feed-feed pseudo cross spectra (this work is currently led by N. Stutzer).

Thereafter, we want to average over the pseudo cross spectra from all the feed-map combinations (that made it through the cuts), where some map associated with feed $a \in \{1, 2, ..., 19\}\backslash\{4, 6, 7\}$ is from set S_a (lower elevation) and map corresponding to feed $b \in \{1, 2, ..., 19\}\backslash\{4, 6, 7\}$ from set S_b (higher elevation). We do this by using the inverse-variance noise weighting,

$$\widetilde{C}_{k_i}^{\mathrm{FPXS}} = \frac{1}{\sum\limits_{a \neq b} w_{ab}} \sum_{a \neq b} w_{ab} \widetilde{C}_{k_i}^{ab}, \tag{4.23}$$

where $w_{ab} = \sigma^{-2}_{\widetilde{C}_{k_i}^{ab}}$ is the inverse variance of the pseudo cross spectrum $\widetilde{C}_{k_i}^{ab}$, computed from feed-maps a and b. Assuming that all the co-added spectra are independent, the uncertainty associated with the averaged pseudo cross spectrum, $\widetilde{C}_{k_i}^{\mathrm{FPXS}}$, becomes

$$\sigma_{\widetilde{C}_{k_i}^{\mathrm{FPXS}}} = \sqrt{\frac{1}{\sum\limits_{a \neq b} w_{ab}}}. \tag{4.24}$$

4.5 Transfer functions and signal model

Following the analysis framework introduced until this point, we could expect that $\widetilde{C}_{k_i}^{\mathrm{FPXS}}$ is the final estimate of the signal pseudo cross spectrum, $\widetilde{P}_{\mathrm{signal}}(k_i)$. Nevertheless, there are some effects that bias the signal component present in the input maps. They can be taken into account by implementing so-called transfer functions, which quantify how large of a fraction of the original signal is still present in the maps, so that

$$\widetilde{C}_{k_i}^{\mathrm{FPXS}} \approx \widetilde{T}_{k_i} \widetilde{P}_{\mathrm{signal}}(k_i), \tag{4.25}$$

where $\widetilde{T}_{k_i}$ is the product of transfer functions associated with different effects, estimated using pseudo spectra. The *unbiased* signal pseudo spectrum measurement and the associated uncertainty are then given by

$$\widetilde{P}_{\mathrm{signal}}(k_i) \approx \frac{\widetilde{C}_{k_i}^{\mathrm{FPXS}}}{\widetilde{T}_{k_i}}, \qquad \sigma_{\widetilde{P}_{\mathrm{signal}}(k_i)} = \frac{\sigma_{\widetilde{C}_{k_i}^{\mathrm{FPXS}}}}{\widetilde{T}_{k_i}}. \tag{4.26}$$

We want to break down the full transfer function into the components representing different effects and estimate them independently from each other. Specifically, we consider three elements,

$$\widetilde{T}_{k_i} = \widetilde{T}_{k_i}^{\mathrm{beam}} \cdot \widetilde{T}_{k_i}^{\mathrm{freq}} \cdot \widetilde{T}_{k_i}^{\mathrm{pipeline}}, \tag{4.27}$$

where the first component represents the finite resolution in the angular dimension due to instrumental beam smoothing out the signal, the second one corresponds to the smearing in the line-of-sight direction (derived from frequency dependence), and the third one is associated with different procedures attenuating the signal during the low level data analysis. In order to estimate these transfer functions, we need to examine their impact on some simulated three-dimensional intensity maps containing the CO signal that we eventually intend to measure. In this section, we will first provide a description of the model used to generate these simulations and thereafter characterize each transfer function separately.

4.5.1 Signal modeling

There are many different studies focusing on modeling the CO signal expected from intensity maps. In COMAP, until recently we have been using the fiducial model of Li et al. [42] from 2016, whose product is the map shown in Figure 4.1. Nevertheless, later measurements conducted by experiments like the CO Luminosity Density at High Redshift survey (COLDz) and the CO Power Spectrum Survey (COPSS) have provided valuable insights that should be taken into account. Therefore, the model was enriched and modified with the new way of parametrization. In this section, we will briefly

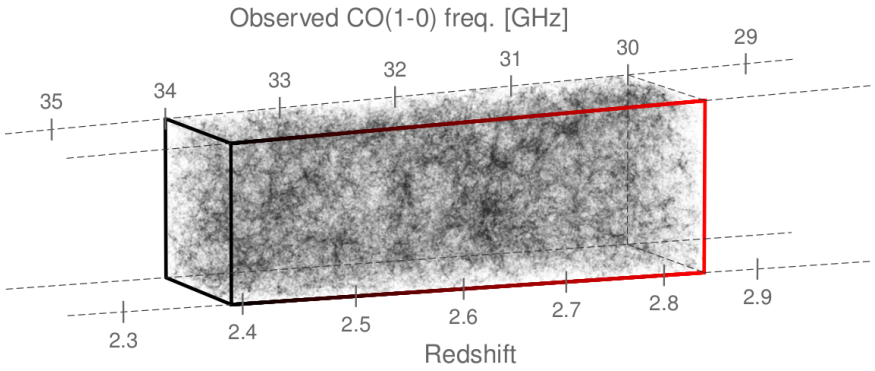

Figure 4.5: Dark matter halos in the 3D space. The frequencies of redshifted CO(1-0) line, together with associated redshift values, are marked along the line of sight [42].

describe the modeling procedure (as in [62, 63]), which is used to generate map simulations needed for estimating the transfer functions, as well as inferring the cosmological information from the data.

The modeling process starts with a lightcone volume containing dark matter halos (illustrated in Figure 4.5), generated from the snapshots of a cosmological N-body dark matter simulation. We then assume that massive halos (with masses $M_h > 10^{10} M_\odot$) host CO-emitting galaxies and want to connect the halo mass to the CO luminosity through several scaling relations. All the intermediate steps can be summarized in the double power-law model, taking the following form:

$$\frac{L'_{\mathrm{CO}}(M_h)}{\mathrm{K\,km\,s^{-1}\,pc^2}} = \frac{C}{(M_h/M_1)^A + (M_h/M_1)^B}, \tag{4.28}$$

where A, B, C and M_1 are some parameters, whose values we want to establish. In addition, we introduce a log-normal scatter, σ_L, associated with the uncertainty of the above relation (which is the average at fixed M_h). The result can then be converted to the units of solar luminosity via

$$\frac{L_{\mathrm{CO}}}{L_\odot} = 4.9 \times 10^{-5} \left(\frac{L'_{\mathrm{CO}}(M_h)}{\mathrm{K\,km\,s^{-1}\,pc^2}} \right). \tag{4.29}$$

We want to infer the best-fit values of all the five parameters of interest at $z \approx 2.4$. The results can then be applied also to the higher redshifts within COMAP's range, since any difference between the outcomes would be below the modeling uncertainties (due to rather depleted information about the CO(1-0) emission at high redshifts). First of all, we adapt initial priors on all the five parameters, combining the insights from Li et al. [42] and information about parameters associated with star formation rate from the UniverseMachine by Behroozi et al. [64]. Then, we form a likelihood function based on the constraints provided by COLDz and use the Markov Chain Monte Carlo (MCMC) approach to obtain the posterior distribution. The resulting set of parameters becomes:

$$\begin{aligned} A &= -2.75, \\ B &= 0.05, \\ \log C &= 10.6, \\ \log(M_1/M_\odot) &= 12.3, \\ \sigma_L &= 0.42. \end{aligned} \tag{4.30}$$

We present the 90% MCMC interval, together with the relation between CO luminosity and halo mass based on the values above in Figure 4.6 (left panel). The same Figure (right panel) shows the power spectrum prediction from our model, compared to the one from Li et al. We can see, that the clustering component of the power spectrum associated with this new model is lower than in Li et al., whereas the shot noise is higher.

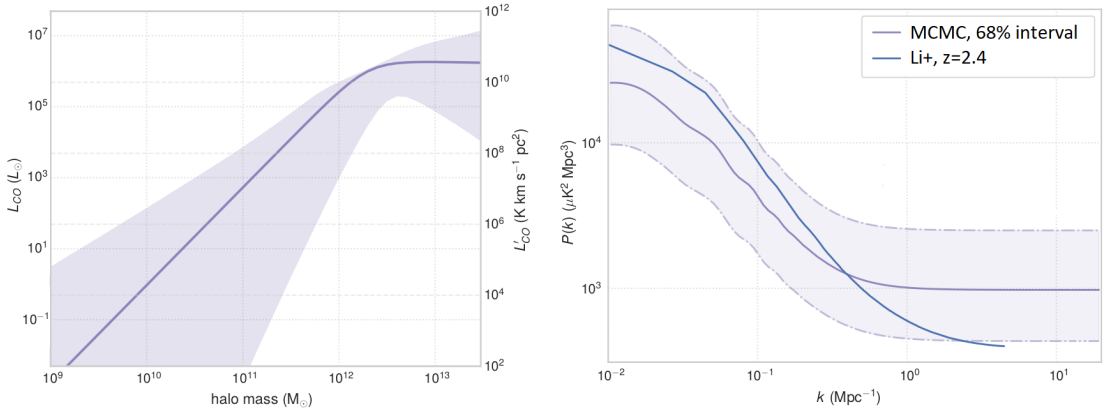

Figure 4.6: Model of CO(1-0) line emission at $z \sim 3$ used in COMAP, obtained from MCMC inference. Left panel shows the 90% interval for the relation between CO luminosity and halo mass, with the curve corresponding to the values of parameters given by Equation 4.30. Right panel illustrates the predicted power spectrum with 68% interval, compared to the model from Li et al. [42] at $z = 2.4$. Adapted from [63].

The parameter posteriors can be used to generate different realizations of the three-dimensional intensity maps. In order to do this, we pick a random distribution from halo catalogues and connect it with the luminosity of CO(1-0) line through the relation $L_{\mathrm{CO}}(M_h)$, with the established set of parameters (Equation 4.30). Thereafter, we convert the CO luminosity to the brightness temperature according to the expression in the Rayleigh-Jeans limit,

$$T_b = \frac{I(z)c^2}{2k_{\mathrm{B}}\nu_{\mathrm{obs}}^2}, \tag{4.31}$$

where c is the speed of light, k_{B} is the Boltzmann constant, ν_{obs} is the observed frequency of the redshifted line, and $I(z)$ is its intensity, given by

$$I(z) = \frac{L_{\mathrm{CO}}(M_h)}{4\pi D_L^2(z)\Delta\nu}, \tag{4.32}$$

where $\Delta\nu$ is the frequency resolution of the maps and $D_L(z)$ is the luminosity distance, related to the comoving distance, $r(z)$ (in Equation 4.11), as $D_L(z) = r(z)(1+z)$ [61]. Then, we connect the temperature values to the particular map voxels, staying in agreement with map characteristics corresponding to the COMAP experiment (like volume or resolution). Based on these simulated maps, we can compute the pseudo power spectra associated with the expected signal, which are needed in the process of estimating the transfer functions.

4.5.2 The effects of limited resolution and line broadening

First of all, we will consider the transfer functions associated with the limited resolution of the instrument in the angular direction, $T^{\mathrm{beam}}(\vec{k})$, and the finite spectral resolution

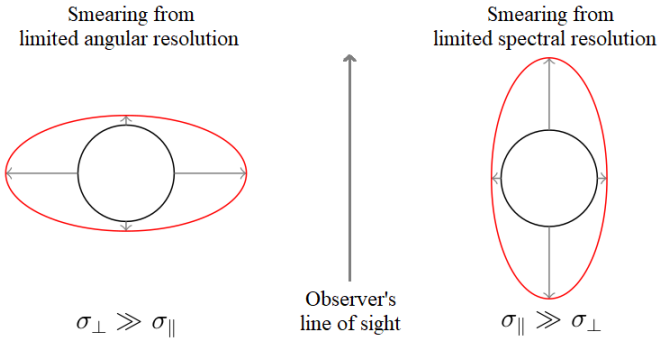

Figure 4.7: Effect of instrumental smearing from limited angular resolution (left panel) and limited spectral resolution (right panel). The black circles illustrate the original image, whereas the red ellipses indicate how it gets distorted. Adapted from [65].

of the maps, $T^{\text{freq}}(\vec{k})$. We generalize the notation from this point, but the exact same procedures apply to our case with the pseudo power spectrum in k-bins (spherically averaged spectrum) or $k_\parallel$-bins and $k_\perp$-bins (2D spectrum).

The finite instrumental resolution affects the signal measurement, distorting the true image of the observed line-intensity field on small scales (high-k modes), as can be seen in Figure 4.7. Effectively, the features that are smaller in angular dimension than the beam width (see Section 3.1.2 for the beam description) or smaller in line-of-sight direction than the width of a frequency channel, will get smoothed out. We can quantify the simplified form of this effect if we approximate the beam profile to be Gaussian with standard deviation σ_{beam} and assume the frequency response to be also Gaussian with standard deviation σ_ν. Then, the smoothed temperature field, that we observe, becomes some distorted version of the field with much higher resolution, convolved with a Gaussian in all dimensions. Since the convolution in real space is just multiplication in Fourier space, the Fourier transform of the smoothed map can be written as

$$\mathcal{F}\{T_{\text{smooth}}(\vec{k})\} = \mathcal{F}\{T(\vec{k})\}\, e^{-\left(\sigma_\perp^2 k_\perp^2 + \sigma_\parallel^2 k_\parallel^2\right)/2}, \tag{4.33}$$

where $\mathcal{F}\{T(\vec{k})\}$ is the Fourier transform of the fine-resolution map and the standard deviations in comoving space can be defined theoretically as

$$\sigma_\perp = r(z)\sigma_{\text{beam}}, \qquad \sigma_\parallel = \frac{c}{H(z)}\,\frac{\sigma_\nu(1+z)}{\nu_{\text{obs}}}, \tag{4.34}$$

where all the parameters follow the same notation as before [42, 65]. The expressions above quantify the comoving distances corresponding to the broadening of the beam profile and frequency response as a function of redshift – we can see the resemblance comparing to Equation 4.11 and Equation 4.14, respectively. In the COMAP experiment, the beam has a full-width-half-maximum (FWHM) of about 4 arcmin, which is equivalent to $\sqrt{8\ln 2}\,\sigma_{\text{beam}}$, so that it can be translated to $\sigma_\perp = 3.1$ Mpc. When it comes to the line-of-sight smoothing, we get $\sigma_\parallel < 1.8$ Mpc, but we need to remember that the

COMAP spectrometer is able to provide higher resolution than the width of frequency channels in the final maps, $\Delta\nu = \sqrt{8\ln 2}\,\sigma_\nu = 31.25$ MHz (since we downgrade the frequency resolution at the end of low-level data analysis), so we essentially account for our choice of the width of frequency channels, not the limitations of the instrument [65].

Angular resolution

We estimate the impact of these effects on the measured signal numerically, separating the analysis in angular direction from the one conducted for the line-of-sight direction. In the case of the instrumental beam transfer function, we start with generating some number of different map realizations, following the signal model and methods described in the previous section. We get two sets of maps. Maps in one set have an increased angular resolution (by a factor of 4), so that we can apply Gaussian beam smoothing to the angular dimensions, with the standard deviation given by

$$\sigma_{\perp,\mathrm{sim}} = \frac{\mathrm{FWHM}}{\sqrt{8\ln 2}\Delta\mathrm{pix}} = \frac{\sigma_{\mathrm{beam}}}{\Delta\mathrm{pix}}, \tag{4.35}$$

where Δpix is the pixel width of the simulated map with increased resolution (0.5 arcmin). The smoothed maps are thereafter downgraded in angular resolution to match the original one (by a factor of 4) and we calculate their pseudo power spectra, $\widetilde{P}_{\vec{k}}^{\mathrm{smooth}}$, for each map independently. The other set is kept without smoothing, with the associated pseudo power spectra, $\widetilde{P}_{\vec{k}}^{\mathrm{original}}$. Then, the transfer function we want to estimate can be calculated as the ratio of average spectra across many signal realizations,

$$\widetilde{T}^{\mathrm{beam}}(\vec{k}) \approx \frac{\left\langle \widetilde{P}_{\vec{k}}^{\mathrm{smooth}} \right\rangle}{\left\langle \widetilde{P}_{\vec{k}}^{\mathrm{original}} \right\rangle}. \tag{4.36}$$

It is worth noting, that even though no noise component is added to the map simulations, we still need noise level maps in order to perform the weighting procedure (as in Equation 4.19) that leads to pseudo cross spectra. For this purpose, we choose to use a noise level map associated with one of the temperature sky maps from the real observations that went through all of the stages of data processing.

Spectral resolution and the intrinsic line width

We use a similar approach for estimating the transfer function associated with spectral resolution of the maps. As mentioned earlier, the native resolution of the COMAP spectrometer is much finer ($\sim$ 2 MHz) than our choice of the final width of frequency channels, $\Delta\nu = 31.25$ MHz. This transfer function is then meant to assess the impact of our specific choice of the spectral resolution on the given set of k-bins, not the limitations of the instrument. In addition, we want to incorporate the effect of the intrinsic width of the CO line in the frequency domain. The spectral line emission cannot be treated

as a discrete spike in the line-of-sight direction (some delta function) but rather as an extended distribution, whose full-width-half-maximum, FWHM_ν, will be assumed to be 30 MHz (although in general it depends on the properties of the halos hosting the CO emitters, see Chung et al. [63] for details). We will then perform the Gaussian smoothing of the field to account for the line broadening, and compare the pseudo power spectra of maps with different spectral resolutions to account for our choice of frequency channels.

Again, we start with generating a number of different map realizations. This time we get two identical sets of maps, both of which are Gaussian smoothed in all the three directions. For angular smoothing we use $\sigma_{\perp,\mathrm{sim}}$, as before, and for the line-of-sight direction we find the following standard deviation associated with the line profile:

$$\sigma_{\parallel,\mathrm{sim}} = \frac{\mathrm{FWHM}_\nu}{\sqrt{8\ln 2}\Delta\mathrm{freq}}, \tag{4.37}$$

where Δfreq is the spectral resolution of simulated maps, which was increased for smoothing by a factor of 4 (~ 0.5 MHz). After smoothing, both sets are downgraded to the original resolution with voxel dimensions $2' \times 2' \times 2$ MHz. One set of maps is kept with such a high spectral resolution to calculate the corresponding pseudo power spectra, $\widetilde{P}^{\mathrm{high}}_{\vec{k}}$. Maps from the other set are downgraded by a factor of 16, to resemble the spectral resolution of the science maps in COMAP (where the width of frequency channels is $\Delta\nu = 31.25$ MHz). The corresponding pseudo power spectra are $\widetilde{P}^{\mathrm{low}}_{\vec{k}}$. Then, the frequency transfer function can be estimated as the ratio of average spectra across many signal realizations,

$$\widetilde{T}^{\mathrm{freq}}(\vec{k}) \approx \frac{\left\langle \widetilde{P}^{\mathrm{low}}_{\vec{k}} \right\rangle}{\left\langle \widetilde{P}^{\mathrm{high}}_{\vec{k}} \right\rangle}. \tag{4.38}$$

4.5.3 Pipeline transfer function

Another source of bias introduced to the final line intensity maps comes from various procedures applied during the low-level data analysis, like filtering, calibration, and mapmaking. The loss of the original CO signal can be quantified through the pipeline transfer function, $\widetilde{T}^{\mathrm{pipeline}}(\vec{k})$. In order to estimate this effect, we again employ the three-dimensional map simulations containing the signal modeled as in Section 4.5.1. Such map is then scanned using the information about pointing of the telescope, which results in a conversion from pixel-ordered data in temperature units to time-ordered data (TOD) in power units. This corresponds to the TOD of the signal we eventually want to measure, d_S, whereas at this stage of the experiment, the TOD obtained from the COMAP instrument is treated as pure noise, d_N. Both data streams are then added together (in power units), yielding d_{S+N}. The next stage is to perform the entire low level data analysis (from raw TOD to 3D maps) separately for d_N and d_{S+N}. Then, we compute the pseudo power spectra of the resulting maps and estimate the pipeline

transfer function as

$$\widetilde{T}^{\text{pipeline}}(\vec{k}) \approx \left\langle \frac{\widetilde{P}^{\text{S+N}}_{\vec{k}} - \widetilde{P}^{\text{N}}_{\vec{k}}}{\widetilde{P}^{\text{S}}_{\vec{k}}} \right\rangle, \tag{4.39}$$

where $\widetilde{P}^{\text{S+N}}_{\vec{k}}$ denotes the pseudo power spectrum of the map containing both simulated signal and noise (generated from d_{S+N}), $\widetilde{P}^{\text{N}}_{\vec{k}}$ corresponds to data from COMAP observations without added signal, d_N (treated as noise), and $\widetilde{P}^{\text{S}}_{\vec{k}}$ is the pseudo power spectrum of the original simulated map with modeled signal.

Typically, we perform the above analysis for the data volume of about 63 COMAP observations (63 ObsIDs), combining Lissajous scans with data from constant elevation scans. We can also separate data obtained using different scanning strategies. This way, we are able to estimate the transfer functions more accurately and apply them individually to the final pseudo spectra of the corresponding map splits. We can also study the impact of altering individual filters on the transfer function, for instance by changing the order of the frequency polynomial in polyfilter or switching the PCA filter on and off. The work focused around the pipeline transfer function is led by N. Stutzer.

4.6 Applications

4.6.1 Null tests

The main end products of the high-level data analysis described in this chapter are the mean pseudo cross spectra computed using the FPXS method. As previously explained, they are equivalent to unbiased estimates of the signal pseudo spectrum, $\widetilde{P}_{\text{signal}}(\vec{k})$, with some uncertainty $\sigma_{\widetilde{P}_{\text{signal}}(\vec{k})}$, and are obtained separately for various subsets of data. This way, we can assess the quality of data, focusing on specific combinations of split variables and identify possible sources of residual systematics. At this stage of the experiment, the resulting spectra are expected to be mostly flat, with some fluctuations around zero within the estimated white noise level. Such a result would indicate that we are able to suppress the contributions from systematics and correlated noise below the current magnitude of white noise. In order to examine if this is indeed the case, we perform so-called *null tests*. We have attempted to use two different approaches:

I **Difference between spectra**
In the first method, we employ a set of $16 \cdot 16$ pseudo cross spectra from all the possible pairs of feed maps, $\widetilde{C}^{ab}_{k_i}$, computed before combining them into a single FPXS estimate (as described in Section 4.4). We split this set into two parts, where we put all the spectra with feed numbers $a < 19 - b$ into one set, and spectra with $a > 19 - b$ into the other one (which corresponds to separating the spectra below and above diagonal of the $N_{\text{feeds}} \times N_{\text{feeds}}$ grid). Then, we combine spectra from these sets separately (using the inverse-variance weighting as usual), so that we get two values of the average pseudo cross spectra, $\widetilde{C}_{1,k_i}$ and $\widetilde{C}_{2,k_i}$ with uncertainties σ_{1,k_i} and σ_{2,k_i}, respectively. Finally, we compute

their difference, $\left(\widetilde{C}_{1,k_i} - \widetilde{C}_{2,k_i}\right)/2$, with associated uncertainty $\sqrt{\sigma^2_{1,k_i} + \sigma^2_{2,k_i}}/2$ (both of which are later divided by the product of transfer functions to obtain the unbiased estimates).

II **Difference between maps**
In the second approach, we calculate the difference already at the map level. Specifically, we start by dividing data in half according to various statistics (test variables) and then subtract the resulting split maps from one another (which is implemented as an option in the `read_multisplit` program module). For instance, in the example illustrated in Figure 4.3, we would subtract the Day map from the Night map (second column) and then continue with subsequent splits and feed-feed pseudo cross spectrum analysis. The same procedure can be performed independently with other types of test variables, like ambient temperature or wind speed (see Section 4.2 for other examples).

Either of these two methods should ideally lead to removing the entire common signal or systematic, leaving only random white noise. Such an outcome would provide a validation of the pipeline performance, whose major goal is suppressing correlated noise contributions through various filtering procedures. In addition, the second approach allows identifying particular sources of possible residual correlations – any sign of surviving signal present in the end results would be an indication of a systematic associated with the feature that was used to split the data set before calculating a given difference map.

4.6.2 Signal-to-noise ratio and signal amplitude estimation

Following most theoretical predictions, the CO signal is weaker than the current level of white noise in the COMAP experiment. However, as the observational data accumulates, it integrates down according to the radiometer equation (Equation 3.4). Eventually, we anticipate that when the white noise is sufficiently low, our signal-to-noise ratio (SNR) will be high enough to claim a detection. A typical minimum requirement for that is a so-called 3σ detection, which means that the measured signal is three times larger than the associated error bars. We can compute the theoretical SNR from the estimated pseudo spectrum of the signal as

$$\mathrm{SNR} = \sqrt{\sum_i \left(\frac{\widetilde{P}_{\mathrm{signal}}(k_i)}{\sigma_{\widetilde{P}_{\mathrm{signal}}(k_i)}}\right)^2}, \tag{4.40}$$

where we sum over all the k-bins [66]. Currently, the SNR is more or less consistent with zero and any deviations are attributable to some residual correlations leading to excess power.

Nevertheless, even now, with the significant presence of the random white noise, we can attempt to use our data to derive some constraints and possibly rule out some of the most optimistic predictions from modeling. We will take two different approaches

in order to estimate the amplitude of the CO power spectrum. The first one is based on the assumption that the measured spectrum is a sum of the constant CO signal amplitude, A_1, and some Gaussian random noise component,

$$\widetilde{P}_{\rm signal}(\vec{k}) = A_1 + {\rm Noise}, \qquad {\rm Noise} \sim \mathcal{N}\left(0, \sigma^2_{\widetilde{P}_{\rm signal}(\vec{k})}\right). \tag{4.41}$$

In order to estimate A_1 and its uncertainty, we use the inverse-variance noise weighting, co-adding over all k-bins (in practice, we exclude some bins outside of our main sensitivity range), so that

$$A_1 = \frac{1}{\sum\limits_i w_{k_i}} \sum_i w_{k_i} \widetilde{P}_{{\rm signal}(k_i)}, \qquad \sigma_{A_1} = \sqrt{\frac{1}{\sum\limits_i w_{k_i}}}, \tag{4.42}$$

where $w_{k_i} = \sigma^{-2}_{\widetilde{P}_{{\rm signal}(k_i)}}$. The other approach assumes a model-dependent estimate, A_2, where the measured spectrum can be written as

$$\widetilde{P}_{\rm signal}(\vec{k}) = A_2 P_{\rm theory}(\vec{k}) + {\rm Noise}, \tag{4.43}$$

with $P_{\rm theory}(\vec{k})$ being the power spectrum corresponding to the CO signal, obtained from the model described in Section 4.5.1. The above equation can then be rewritten as

$$\frac{\widetilde{P}_{\rm signal}(\vec{k})}{P_{\rm theory}(\vec{k})} = A_2 + {\rm Noise}', \qquad {\rm Noise}' \sim \mathcal{N}\left(0, \frac{\sigma^2_{\widetilde{P}_{\rm signal}(\vec{k})}}{P^2_{\rm theory}(\vec{k})}\right). \tag{4.44}$$

We can obtain the A_2 estimate similarly as before, but now making sure that the measured spectrum and its uncertainty are divided by the theory spectrum,

$$A_2 = \frac{1}{\sum\limits_i w'_{k_i}} \sum_i \frac{w'_{k_i} \widetilde{P}_{{\rm signal}(k_i)}}{P_{{\rm theory}(k_i)}}, \qquad \sigma_{A_2} = \sqrt{\frac{1}{\sum\limits_i w'_{k_i}}}, \tag{4.45}$$

where $w'_{k_i} = \left(\sigma_{\widetilde{P}_{{\rm signal}(k_i)}} / P_{{\rm theory}(k_i)}\right)^{-2}$. Since the final pseudo spectra obtained using different subsets of data can be combined (also using inverse-variance weighting), we can reject the parts of data that show signs of residual systematics and find a suitable signal measurement to perform reliable fits of A_1 or A_2.

Part III

Results

Chapter 5

Effects altering the signal

Transfer functions and mode mixing assessment

In this part of the thesis, we will present and discuss the results obtained by applying the methodology described in the preceding sections. First of all, the focus will be put on the effects that modify the signal measured based on the final three-dimensional temperature sky maps. This includes the smoothing of the smallest angular scales due to the finite resolution of the instrument, as well as the impact of the intrinsic line width and the limited spectral resolution of the maps. In addition, we will show how the signal is modified due to various procedures applied during the low-level data analysis, separating data obtained using the Lissajous scanning strategy from the constant elevation scans (CES). We will also combine these effects into a single transfer function, which will be applied to all the main Feed-feed Pseudo CROSS Spectrum (FPXS) results (presented in the next chapter), limiting the sensitivity of the experiment to a certain range of cosmological scales. Finally, we will perform an assessment of the mode mixing, arising due to the noise weighting of the maps, conducted prior to computing their power spectra. We will also discuss the possible solutions that can be incorporated into the analysis in order to undo this effect and obtain an unbiased measurement of the signal.

5.1 Transfer functions

We will begin by presenting the results connected to the transfer functions, which quantify the fraction of the signal that remains in the intensity maps after taking into account various effects. First, we will consider all the components separately – the instrumental beam transfer function, $\widetilde{T}^{\mathrm{beam}}(\vec{k})$, the transfer function linked to the spectral resolution of the maps, $\widetilde{T}^{\mathrm{freq}}(\vec{k})$, and the one related to the pipeline procedures, $\widetilde{T}^{\mathrm{pipeline}}(\vec{k})$. Thereafter, we will calculate their product, merging them together into a single transfer function, $\widetilde{T}^{\mathrm{total}}(\vec{k})$. The impact of every effect will be shown in the spherically averaged form (as a function of $k \equiv \sqrt{k_x^2 + k_y^2 + k_z^2}$), as well as in two dimensions (decomposed into parallel modes, $k_{\parallel} \equiv |k_z|$, and perpendicular modes, $k_{\perp} \equiv \sqrt{k_x^2 + k_y^2}$).

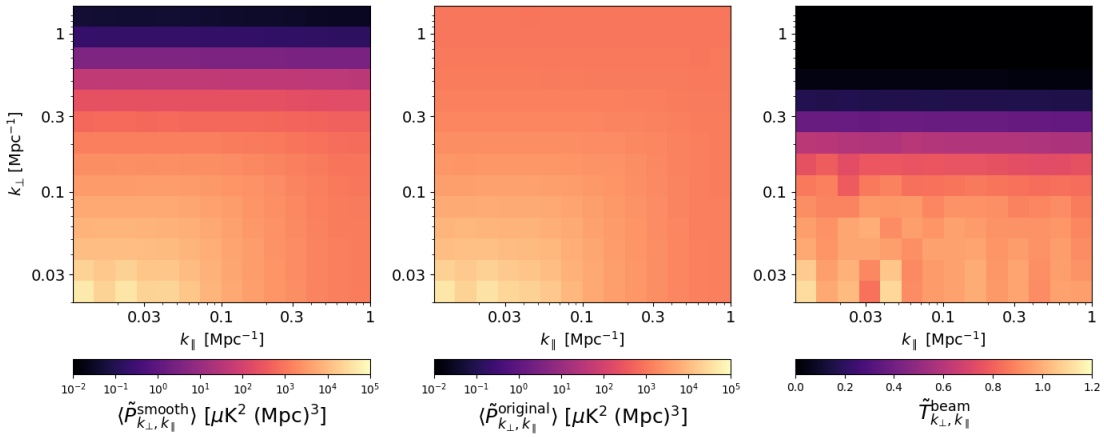

Figure 5.1: Instrumental beam transfer function decomposed into parallel modes, $k_\parallel$, and perpendicular modes, $k_\perp$ (right panel). We show the mean of pseudo power spectra from 100 signal realizations with applied Gaussian beam smoothing (left panel), and without smoothing (middle panel). The transfer function is defined as the ratio between them, $\widetilde{T}^{\rm beam}_{k_\perp,k_\parallel} = \langle \widetilde{P}^{\rm smooth}_{k_\perp,k_\parallel} \rangle / \langle \widetilde{P}^{\rm original}_{k_\perp,k_\parallel} \rangle$.

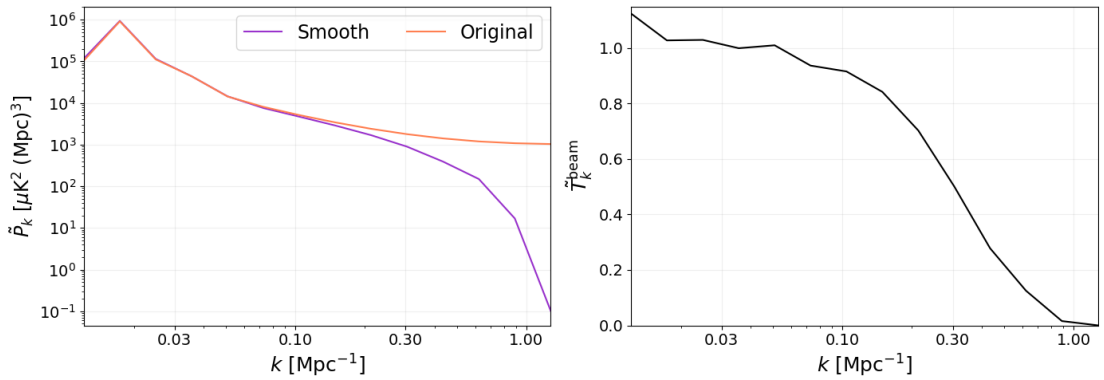

Figure 5.2: Spherically averaged beam transfer function (shown on the right panel). On the left, we plot the mean pseudo power spectra computed from 100 simulated maps with Gaussian beam smoothing applied to the angular dimensions (purple) and without beam smoothing (orange).

5.1.1 Angular resolution

First of all, we consider the instrumental beam transfer function, $\widetilde{T}^{\rm beam}(\vec{k})$. Following the methodology explained in Section 4.5.2, we generate two sets of 100 three-dimensional maps with different signal realizations (in agreement with our model). In order to account for the limited resolution of the telescope, we smooth maps from one

set along the angular dimensions. For now, it is assumed that the instrumental beam does not depend on frequency and can be approximated by a Gaussian with a full-width-half-maximum (FWHM) angle of 4 arcmin. Nevertheless, such a simplification implies that the beam efficiency is equal to one, so that the entire sky signal is contained within the main beam. In reality, the beam efficiency of COMAP antenna is closer to 0.7 (see Section 3.1.2), so that a considerable amount of power is picked up by the sidelobes. The consequence of not taking that effect into account is an overestimation of the pseudo power spectra derived from the smoothed maps – in reality, their value will be lower as not the entire signal is located in the main beam. The measured power of the signal is rather distributed among the parts of the beam pattern (which is more complicated than the Gaussian we assume). Nevertheless, despite the slight magnitude bias, our estimated instrumental beam transfer function can still be applied to the data used in the subsequent scientific analysis. It will be left for future work to implement a more realistic model of the beam pattern, increasing the precision of these calculations.

After generating the maps, we perform the noise weighting (using the noise levels from our observations) and calculate pseudo power spectra. Then, we take the mean across 100 signal realizations, separately for both sets – $\langle \widetilde{P}^{\mathrm{smooth}}(\vec{k}) \rangle$ associated with smoothed maps and $\langle \widetilde{P}^{\mathrm{original}}(\vec{k}) \rangle$ corresponding to fine-resolution maps (unsmoothed ones). According to Equation 4.36, the instrumental beam transfer function becomes the ratio of these. We present the results in the $k_\parallel - k_\perp$ plane in Figure 5.1 and the spherically averaged version in Figure 5.2. The assumed FWHM of the beam can be translated into the comoving distance of about 7.3 Mpc ($\sqrt{8 \ln 2}\,\sigma_\perp$, where $\sigma_\perp = 3.1$ Mpc), so that the angular scales that are strongly affected are $k_\perp \gtrsim 2\pi/(7.3 \text{ Mpc}) \approx 0.86 \text{ Mpc}^{-1}$. We can see the significant power suppression towards the small angular scales (high $k_\perp$ values) looking at the mean spectrum derived from the ensemble of smoothed maps (left panel in Figure 5.1) and the corresponding transfer function (right panel). This is also clear in the spherically averaged case (with $k \equiv \sqrt{k_\perp^2 + k_\parallel^2}$), where the measured spectra start to deviate from each other at $k \sim 0.2 \text{ Mpc}^{-1}$ (left panel in Figure 5.2). A steeper decrease of the smoothed spectrum can be observed at the very smallest scales, resulting in almost complete signal attenuation, $\widetilde{T}^{\mathrm{beam}}(k \gtrsim 0.9 \text{ Mpc}^{-1}) \approx 0$. This becomes the limiting factor for our observations, quantifying the comoving angular resolution of the instrument.

5.1.2 Spectral resolution

Next, we look into the impact of spectral resolution, quantified in the separate transfer function, $\widetilde{T}^{\mathrm{freq}}(\vec{k})$. As explained in Section 4.5.2, we do not examine the instrumental resolution (~ 2 MHz) but the width of frequency channels in the final intensity maps (31.25 MHz). This difference in magnitude is the result of downsampling of the time-ordered data (TOD) towards the end of the low-level data analysis (right before the mapmaking), as described in Section 3.3.2. We want to study how this procedure affects the signal measurement conducted based on the temperature sky maps.

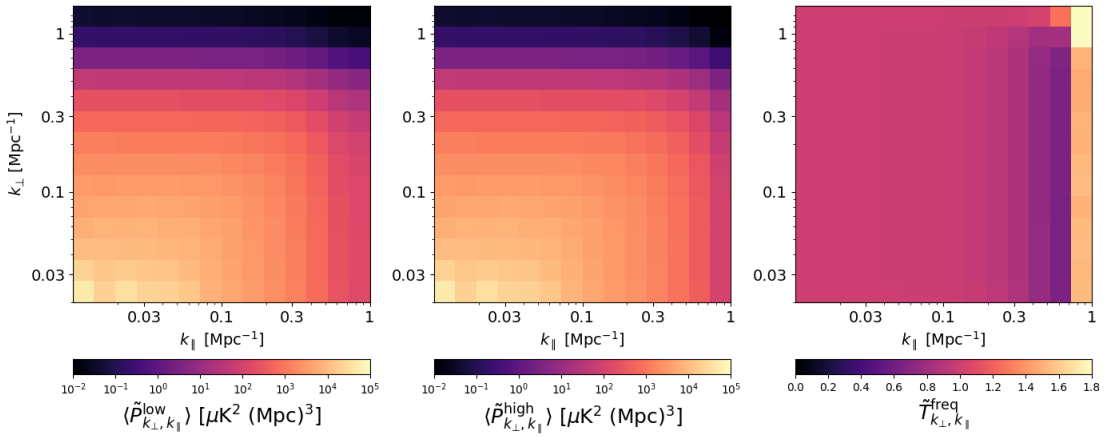

Figure 5.3: Transfer function associated with spectral resolution of the intensity maps in the $k_\parallel - k_\perp$ plane (right panel). We also show the mean of pseudo power spectra from 100 signal realizations with frequency resolution downgraded to 32 MHz (left panel), and with 16 times finer resolution (middle panel). Both results are derived from the maps smoothed in angular and line-of-sight direction. The transfer function is defined as the ratio between them, $\widetilde{T}^{\rm freq}_{k_\perp,k_\parallel} = \langle \widetilde{P}^{\rm low}_{k_\perp,k_\parallel} \rangle / \langle \widetilde{P}^{\rm high}_{k_\perp,k_\parallel} \rangle$.

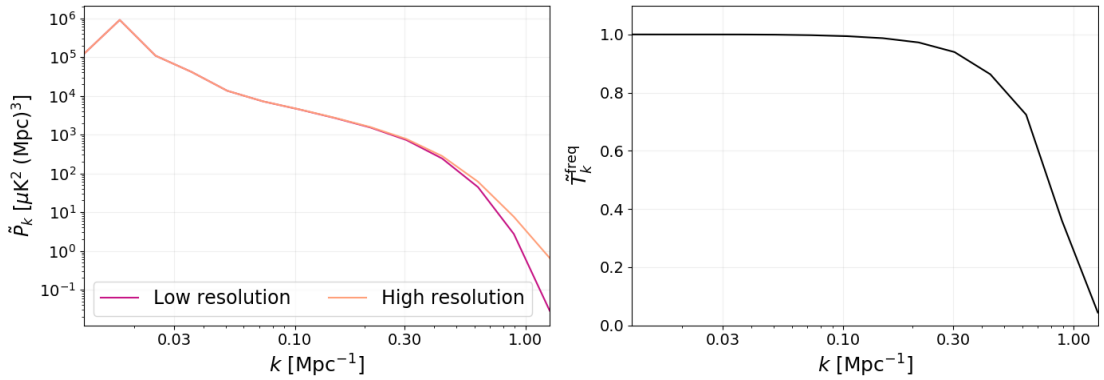

Figure 5.4: Spherically averaged transfer function associated with spectral resolution of the maps (shown on the right panel). On the left, we plot the mean pseudo power spectra computed from 100 simulated maps with low spectral resolution (pink) and with 16 times higher resolution (orange).

Again, we produce two sets of 100 three-dimensional maps with different signal realizations. As before, the maps are smoothed with a Gaussian beam in the angular dimension. In addition, we account for the intrinsic line profile by smoothing along the line-of-sight direction (since the CO line is a distribution in the frequency domain, not a discrete spike). These smoothing procedures blur the simulated maps to obtain a more

realistic view of the field, as seen by the telescope. Thereafter, the maps in one set are downgraded in spectral resolution (resulting in ∼32 MHz-wide channels, similar to the maps we get from COMAP observations) and the other set is kept in high resolution (∼ 2 MHz). We calculate pseudo power spectra based on the maps in both sets and take their averages – $\langle \widetilde{P}^{\rm low}(\vec{k})\rangle$ for maps with downgraded resolution and $\langle \widetilde{P}^{\rm high}(\vec{k})\rangle$ for fine-resolution maps. The frequency transfer function (or *pixel window*) becomes the ratio of these, as in Equation 4.38. It is worth noting that we need to compute the ratio of mean spectra (not the mean of individual ratios), only because the signal realizations in consecutive single maps from both sets are not identical (i.e. the map number $i \in \{1, 2, \ldots, 100\}$ from the low-resolution set does not exhibit the same signal realization as the map number $j = i$ from the high-resolution set). This concerns both the frequency transfer function and, previously shown, transfer function associated with a limited angular resolution of the instrumental beam.

We show the results decomposed into parallel modes, $k_\parallel$, and perpendicular modes, $k_\perp$, in Figure 5.3 and the spherically averaged version (function of k) in Figure 5.4. Looking at the spectra in two dimensions, we can see the clear power attenuation towards the high $k_\perp$ values, exactly as in Figure 5.1 (left panel). This is the result of the same beam smoothing applied to both sets of maps. In addition, we see decreasing power towards the small scales along the line of sight (high $k_\parallel$), which is the effect of the intrinsic line broadening. We assumed the line to have a Gaussian profile with $\mathrm{FWHM}_\nu = 30$ MHz. The corresponding comoving distance is ~ 4.2 Mpc ($\sqrt{8\ln 2}\,\sigma_\parallel$, where $\sigma_\parallel \approx 1.8$ Mpc), which translates to the complete smearing of the structures on the parallel scales similar to the depth of voxels in our maps ($k_\parallel \gtrsim 1.4$ Mpc^{-1}). This effect is studied in more detail by Chung et al. [63], where in general a $\sim 10\%$ attenuation of the spherically averaged spectrum is expected (on scales $k \approx 0.2 - 0.3$ Mpc^{-1}). Here, we focus on the difference between the results derived from low-resolution and high-resolution maps. In Figures 5.3 and 5.4, we can see that the low-resolution spectrum is similar to the high-resolution one for $k_\parallel \lesssim 0.3$ Mpc^{-1}, where $\widetilde{T}^{\rm freq}(k) \approx 1$. Then, the low-resolution spectrum starts to decrease more significantly, as we enter the regime where the downgrading of spectral resolution smears out the small scales. This trend continues until our last $k_\parallel$-bin, where the voxels in high-resolution maps are smoothed out anyway due to the intrinsic line width. Therefore, the high-resolution spectrum is now lower compared to the low-resolution one, and the transfer function exceeds 1. It is not visible in the spherically averaged case, where the perpendicular modes balance out this effect.

5.1.3 Low-level data analysis

Another effect that modifies the measured signal is the attenuation caused by various procedures performed during the low-level data analysis, which can be quantified in a separate transfer function, $\widetilde{T}^{\rm pipeline}(\vec{k})$. The credit for the work conducted in this regard goes to N. Stutzer, who provided the data that we present in Figures 5.5 and 5.6. Since it is an integral part of the full transfer function applied to our main cross spectrum results, we present its brief overview for completeness.

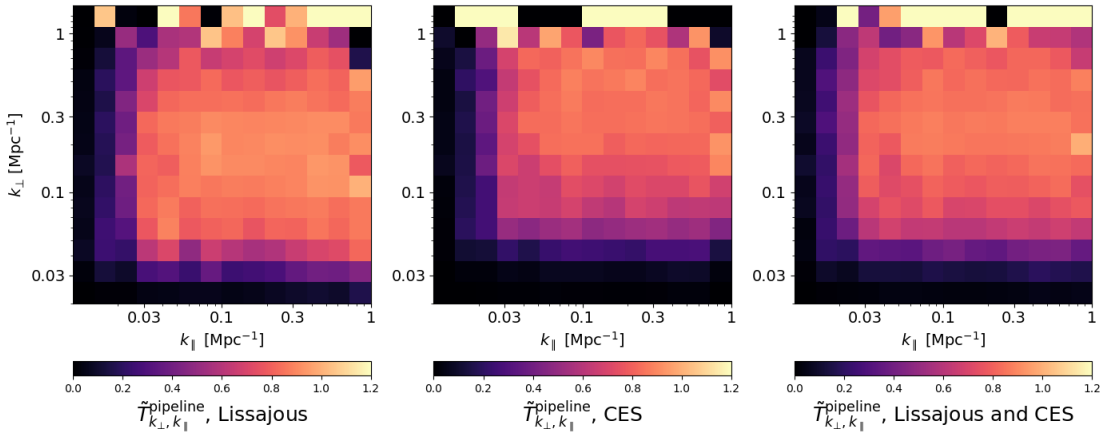

Figure 5.5: Pipeline transfer function associated with procedures applied during the low-level data analysis, shown in $k_\parallel - k_\perp$ plane. These estimates are obtained using the raw data containing only Lissajous scans (left panel), only constant elevation scans (middle panel), and the combination of both (right panel).

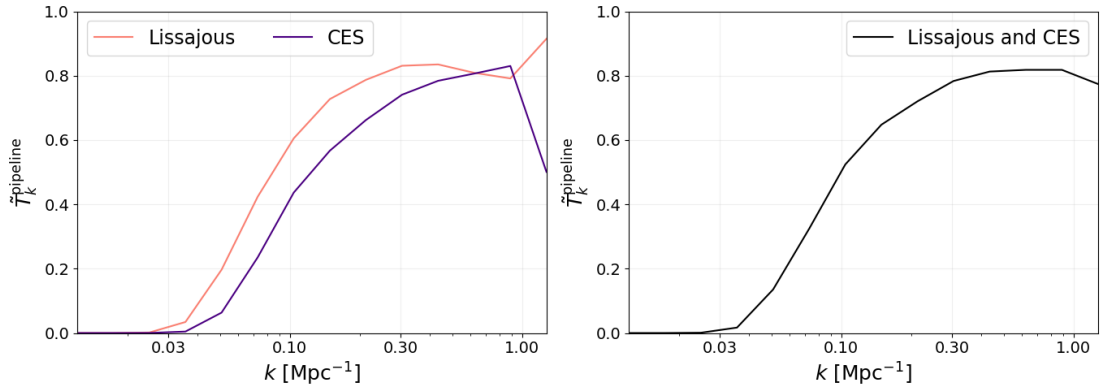

Figure 5.6: Spherically averaged version of the pipeline transfer function. On the left, we show the estimate obtained using data with only Lissajous scans (orange) and only constant elevation scans (purple). On the right, we show the transfer function associated with the combination of both scanning strategies used in COMAP.

As explained in Section 4.5.3, we process the sum of the simulated signal and the noise component (represented by our observations at this point of the experiment) through the entire low-level data analysis pipeline. We perform the same procedure for the data without added signal and calculate the difference of the corresponding pseudo power spectra. The transfer function is found by dividing with the spectrum associated with the pure simulated signal, according to Equation 4.39. For now, only three signal realizations are being used (as it is computationally expensive to process all the time-ordered data sets through the pipeline). We show the results in the $k_\parallel - k_\perp$ plane in

Figure 5.5, together with the spherically averaged version in Figure 5.6. The estimates are obtained for three types of raw data – the TOD containing only Lissajous scans, only constant elevation scans (CES), or the mix of both (in equal proportion). We use 63 observations ($\sim$ 63 hours) for the case with mixed scans and the smaller portion of data (3 observations) for the estimates employing individual scanning strategies.

As opposed to the previously shown transfer functions, this one mostly affects the large scales (both angular and line-of-sight direction), targeted by various filters. The spherically averaged results show nearly complete signal attenuation for $k \lesssim 0.03$ Mpc^{-1} (see Figure 5.6). We can notice that the Lissajous scanning strategy leads to a smaller signal loss than CES, as its transfer function is higher across almost the entire range of scales. This can be connected to a better sky coverage of Lissajous scans compared to CES (discussed in Section 3.2.2). The combination of different scan types exhibits the transfer function that resembles a mean between the two individual cases. This is also true for the results decomposed into parallel and perpendicular modes (Figure 5.5).

5.1.4 The full transfer function

Finally, we can combine the insights provided by the analysis of all the components described in the preceding sections into a single estimate of the full transfer function, $\widetilde{T}^{\text{total}}(\vec{k}) = \widetilde{T}^{\text{beam}}(\vec{k}) \cdot \widetilde{T}^{\text{freq}}(\vec{k}) \cdot \widetilde{T}^{\text{pipeline}}(\vec{k})$. This total transfer function will be subsequently applied to all the cross spectrum results shown in the following chapter (as in Equation 4.26). This correction to our measurement gives an unbiased estimate of the signal pseudo power spectrum. We show the total transfer function decomposed into parallel and perpendicular modes in Figure 5.7 and the corresponding spherically averaged version in Figure 5.8. As the pipeline component was assessed for the three different cases, we also separate Lissajous data from constant elevation scans, in addition to showing the result associated with the combination of both scanning strategies used in COMAP. In order to increase the precision of the final signal estimation, we will apply the appropriate version of the total transfer function to the results obtained for the subsets of maps containing only a single type of scan.

We can clearly see how the total transfer function limits the sensitivity of the experiment. Looking at Figure 5.7, we are easily able to recognize the contributions from particular components – the instrumental beam transfer function attenuating the signal on small angular scales (corresponding to high $k_\perp$ values), the pixel window affecting the small scales in the line-of-sight direction (high $k_\parallel$), and the pipeline processes impacting the large scales (low values of $k_\perp$ and $k_\parallel$). Most of the signal ($\gtrsim 50\%$) is retained in the region of the $k_\parallel - k_\perp$ plane extending between $k_\parallel = 0.03$ Mpc^{-1} and $k_\parallel = 0.4$ Mpc^{-1}, and angular scales $k_\perp = 0.05 - 0.2$ Mpc^{-1}. This varies depending on the strategy of scanning the sky – as we have seen, the Lissajous transfer function is in general higher, indicating that it is a more optimal type of scan in regards to the signal loss. This is also visible in the spherically averaged case (Figure 5.8), where the maximum sensitivity for the Lissajous transfer function corresponds to $\widetilde{T}^{\text{total}}(k \approx 0.15 \text{ Mpc}^{-1}) = 0.6$, whereas the transfer function of CES peaks with $\widetilde{T}^{\text{total}}(k \approx 0.15 \text{ Mpc}^{-1}) = 0.45$. The estimate for the combination of different scans is close to the mean of these two separate cases.

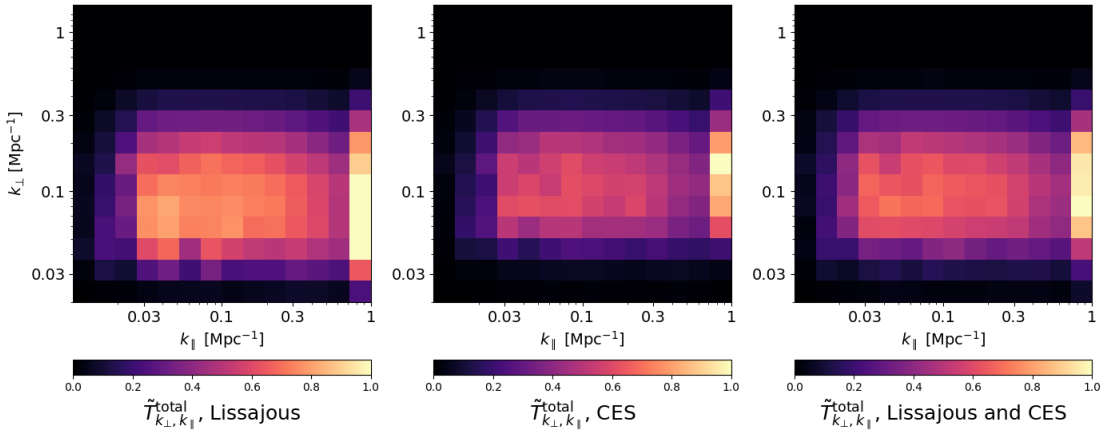

Figure 5.7: Total transfer function in the $k_\parallel - k_\perp$ plane, being the product of three components, $\widetilde{T}^{\rm total}_{k_\perp,k_\parallel} = \widetilde{T}^{\rm beam}_{k_\perp,k_\parallel} \cdot \widetilde{T}^{\rm freq}_{k_\perp,k_\parallel} \cdot \widetilde{T}^{\rm pipeline}_{k_\perp,k_\parallel}$ (the effects of limited angular and spectral resolution, as well as the impact of low-level data analysis). We separate the estimates including the pipeline transfer function derived for the Lissajous scans (left panel), constant elevation scans (middle), and the combination of both (right panel).

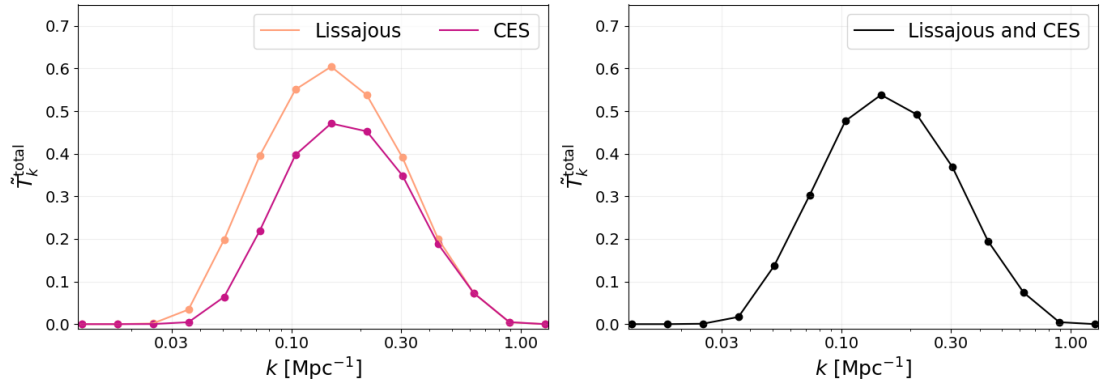

Figure 5.8: Spherically averaged total transfer function. On the left, we show the estimates including the pipeline transfer function derived separately for the Lissajous scans (orange) and constant elevation scans (pink). On the right, we show the case corresponding to the combination of both scanning strategies. The dots indicate the centers of k-bins.

In the subsequent analysis of the main results, we will exclude the k-bins for which the signal is almost completely suppressed. This concerns the four bins corresponding to the smallest k values and two of them with the highest k (in practice we divide the cross spectrum estimate and associated uncertainty by the full transfer function so that these points will lie outside the range of our plots, with extremely large error bars).

5.2 Mode mixing

Before we present the main pseudo cross spectrum results, we will carry out an assessment of the mode mixing effect (the Fourier modes binned to the wrong k-intervals). As explained in Section 4.3.2, we account for the noise fluctuations in the maps by performing inverse-variance noise weighting (prior to computing pseudo cross spectra). This process will inevitably bias the signal measurement conducted based on such noise-weighted maps. We want to evaluate the impact of this procedure on the resulting power spectrum of the signal. In order to do that, we generate 10 maps with different signal realizations (in agreement with our model). Thereafter, we use this map set to compute the spherically averaged auto spectra (without noise weighting), $P(k)$, and pseudo auto spectra (applying noise weighting), $\widetilde{P}(k)$. We show the mean ratio of these across the relevant range of cosmological scales in Figure 5.9. The error bars are the values of standard deviation across ten signal realizations in each corresponding k-bin. We can see, that in general the magnitude of the effect varies between $\sim 25\%$ on large scales ($k \approx 0.05$ Mpc^{-1}) and $\sim 5\%$ on smaller scales.

The statistical information provided by the unbiased auto spectrum and our pseudo spectrum is the same. However, an auto spectrum may be directly compared to various theoretical predictions, whereas the interpretation of a pseudo spectrum generally depends on the given experiment. For consistency between the signal simulations and our observations, we perform the same noise weighting on the maps created based on the signal model as is applied to the COMAP data (we do not add the noise component to the maps containing the simulated signal, only weight them appropriately). This concerns the entire transfer function analysis (where we used pseudo power spectra), as well as the estimation of the signal amplitude and comparison with the main theoretical model (more on that in Section 6.3.1).

Since we adjust the simulations with adequate noise weighting and the mode mixing effect is quite mild on most relevant cosmological scales, we will analyze the main cross spectrum results in the current form. Nevertheless, for the high precision analysis, it is advisable to undo the mode mixing effect in order to derive the unbiased signal estimate. This can be performed by computing and inverting the mode mixing matrix, $\mathbf{M}$, relating the pseudo spectrum to the auto spectrum by

$$\widetilde{P}(\vec{k}) = \sum_{\vec{k'}} P(\vec{k'}) M_{\vec{k},\vec{k'}}. \tag{5.1}$$

This procedure tends to be computationally expensive, as the mode-mode coupling has to be calculated for every combination between all the Fourier modes. A similar approach was originally developed and described by Hivon et al. [67] for the analysis of data from CMB experiments, where it is called the Monte Carlo Apodised Spherical Transform EstimatoR (MASTER) algorithm. We leave it for future work to implement an equivalent method (or some more computationally efficient approximation) to the COMAP data sets.

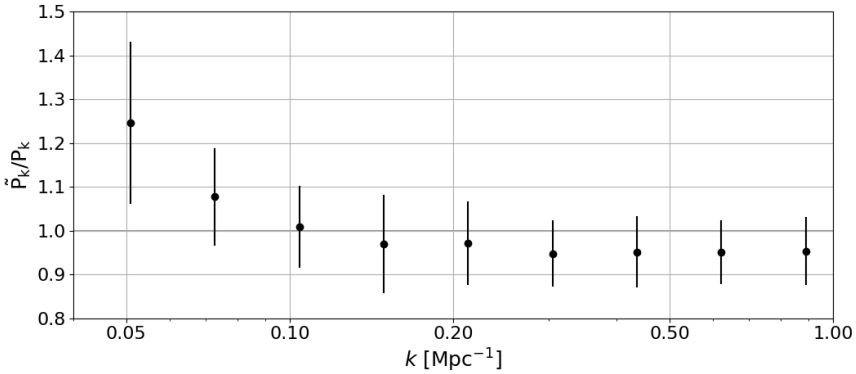

Figure 5.9: Average ratio between the spherically averaged pseudo auto spectra (derived from noise-weighted maps) and auto spectra (from maps without noise weighting). It is computed based on 10 different signal realizations, where the error bars represent the standard deviation across the entire map set in the corresponding k-bin.

Chapter 6

Feed-feed Pseudo CROSS Spectrum

Data quality assessment and signal estimation

During the low-level data analysis (illustrated in Figure 3.7), the raw time-ordered data are filtered, calibrated, and converted into the pixel-ordered data – the three-dimensional temperature sky maps. These maps are thereafter processed through our high-level pipeline (see Figure 4.2), based on the Feed-feed Pseudo CROSS Spectrum (FPXS) method. The process starts with dividing the data set into many three-dimensional sky maps, then we compute the pseudo cross spectra using all the possible map pairs, and finally, combine them into a single estimate of the signal pseudo spectrum. In this chapter, we will present and discuss the main results obtained through this approach. The method is devised in order to minimize the risk from misestimation of the noise component present in the maps (as it does not impact the signal measurement, only the associated uncertainty), increase the sensitivity of the calculation (compared to a single data-split necessary to cross-correlate two maps), and lower the susceptibility to residual systematic errors (associated mainly with the statistic with respect to which the data are split). In order to derive an unbiased estimate of the signal pseudo spectrum, all results will be corrected with the total transfer function described in the previous chapter (taking into account the limited angular and spectral resolution, as well as the large-scale signal attenuation caused by the low-level data analysis).

At this point, we will present the pseudo cross spectra and demonstrate the most important applications of these results. First and foremost, they will be used to assess if the procedures applied during the low-level analysis were able to successfully suppress the contributions from correlated noise. In addition, we will find the estimates of the signal amplitude (using two different approaches), compare our results to theoretical predictions from signal modeling, and show the expectations for the future.

Since we split data in many different ways, we choose to show only some of the selected examples representing various types of the obtained results. Specifically, we will use elevation as the cross variable in all the main results, show a selection of the null tests, and present the analysis of the CO amplitude estimation for the combination of best-behaved pseudo cross spectra. For those interested, the compilation of more different results can be found here: `tsih3.uio.no/www_cmb/comap/jowita_xs`.

6.1 Main results

To start with, we will focus on the main results of the FPXS method, which are the mean pseudo cross spectra. These will be shown separately for every science field that is observed by the COMAP telescope – CO2, CO6, CO7 (more on the selection and location of the fields in Section 3.2.1). As described in Section 4.4, the essential step of the process is splitting the data sets into many maps. First of all, we separate all the observations with respect to scanning strategy (this is a control variable), because CES and Lissajous scans have their own specific characteristics and are associated with different systematics. In addition, we need a cross variable, which will be used to divide data into two disjoint sets, comprised of 16 feed-maps (one map corresponding to each feed included in the current analysis). We choose the elevation statistic for this purpose, as it is associated with one of the most problematic systematics in the COMAP experiment – the ground contamination (arising as a result of beam sidelobes hitting the ground and picking up some contribution to the signal). All the pseudo cross spectra will be derived from a map pair, where one map always contains observations taken at lower elevations and the other map includes only high-elevation data. This way, most of the residual signal from ground pickup will not be common between the cross-correlated maps and will cancel out in the resulting pseudo cross spectrum.

The split maps are processed separately for all the considered subsets of data (CO2 CES, CO2 Lissajous, CO6 CES, CO6 Lissajous, CO7 CES, CO7 Lissajous), undergoing several stages of the high-level analysis pipeline. The operations described in Section 4.3 are performed on every possible combination of feed-maps from low-elevation set and high-elevation set. This involves converting to cosmological map grids, weighting with noise level maps, computing the pseudo cross spectrum, binning the Fourier modes, and generating white noise simulations to find the associated uncertainty. Thereafter, each set comprised of $16 \cdot 16$ pseudo cross spectra is examined with the χ^2 statistic, and only the spectra not exhibiting the signs of high excess power are co-added into the mean estimate. We will present the analysis of this data selection procedure in Section 6.1.1, before proceeding to the mean spectra in Section 6.1.2. The results will be shown for the spherically averaged case (spectra as a function of $k \equiv \sqrt{k_x^2 + k_y^2 + k_z^2}$), as well as in two dimensions (decomposed into parallel modes, $k_\parallel \equiv |k_z|$, and perpendicular modes, $k_\perp \equiv \sqrt{k_x^2 + k_y^2}$).

6.1.1 Final data selection

Following all the filtering procedures and data selection performed during the low-level analysis, we expect the noise component of the maps to follow the distribution of uncorrelated Gaussian noise. In order to assess if this is the case, we compute the χ^2 statistic (according to Equation 4.22) for every single pseudo cross spectrum derived from pairs of feed-maps. The results of this process for each analyzed subset of data are presented in Figure 6.1. These grids show the signs of any residual excess power, indicating deviations from the expected white uncorrelated noise. Here, we also multiply

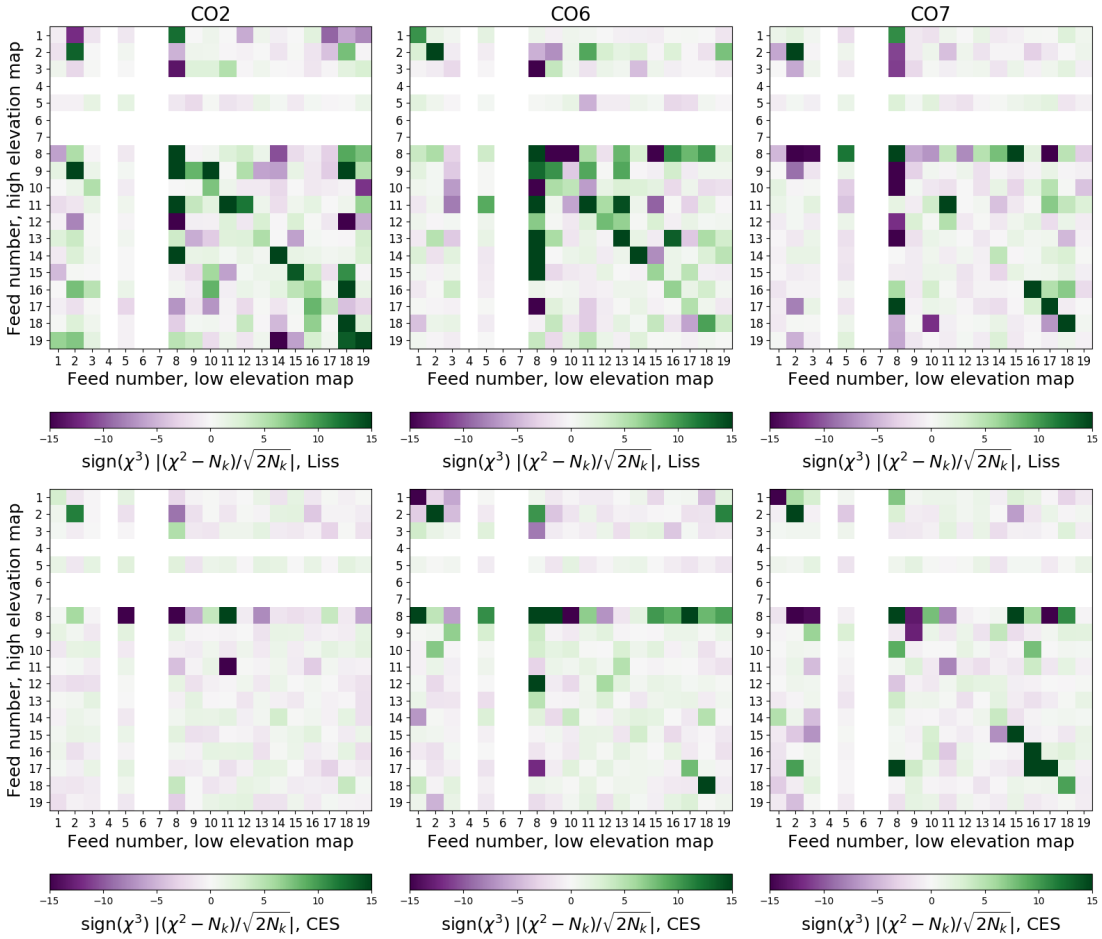

Figure 6.1: Grids showing deviations from white noise of the pseudo cross spectra corresponding to particular pairs of feed-maps (taken from two disjoint data sets, split according to elevation). We show the data from Lissajous scans only (upper row) and constant elevation scans (lower row), separately for each science field – CO2 (left), CO6 (middle), CO7 (right). Three feeds are excluded from the analysis (4, 6, 7).

↓ Scanning strategy	Field →	CO2	CO6	CO7
Lissajous scans		79.2%	83.3%	86.3%
Constant elevation scans		96.7%	90.0%	91.3%

Table 6.1: Fraction of the feed-feed pseudo cross spectra (FPXS) that passes through the 5 sigma cut (after excluding the identical-feed pairs) and can be co-added into the mean spectrum of the corresponding field and scanning strategy.

with the sign of χ^3 characteristic (computed as in Equation 4.21, but being cubed instead of squared), in order to show if the correlation is positive or negative. Such analysis can verify if the previous phase of the data selection (`accept_mod`) was sufficiently strict or if it could be revisited in order to include more data in this final stage of the analysis (which could improve the sensitivity of the measurement). We can see that most of the spectra from CES do not exhibit signs of excess power, with the cleanest data corresponding to the CO2 field. Nevertheless, we notice a clear presence of residual systematics in the Lissajous spectra, especially for the CO2 and CO6 fields. This might be associated with the effects that have not been sufficiently suppressed in the low-level data analysis, for instance, the atmospheric contributions to the signal. Such components vary more significantly when the telescope is changing the pointing coordinates to scan the sky following the Lissajous pattern than in the case of the constant-elevation motion.

We want the final mean pseudo cross spectrum estimate to be as robust to the correlated noise residuals as possible. In order to minimize the instrumental systematics associated only with a single detector chain, we exclude all the feed pairs for which both maps correspond to the same feed (this way we reject the spectra enhancing the factors common only between the maps from the given feed). In addition, we discard the feed-feed pseudo cross spectra for which the absolute value of χ^2 statistic exceeds 5 sigma. Table 6.1 gathers the results from this cut and summarizes our observations from the analysis of the grids in Figure 6.1. We can see that $\sim 3-10\%$ of the CES and $\sim 14-21\%$ of the Lissajous spectra are removed in this process.

6.1.2 Mean pseudo cross spectra

Finally, all the feed-feed pseudo cross spectra that have survived the cut described above can be co-added into a single mean estimate according to Equation 4.23, with the associated uncertainty in each k-bin computed as in Equation 4.24. Thereafter, the mean is divided by the full transfer function in order to obtain the unbiased pseudo spectrum (Equation 4.26). We perform this procedure separately for both scanning strategies and all three science fields.

The results associated with the CES data are shown in Figure 6.2 (spherically averaged) and Figure 6.3 (decomposed into parallel and perpendicular modes). Looking at the spherically averaged case, we can see that the spectra appear to be mostly flat, with some fluctuations around zero that are generally in agreement with our uncertainty estimates derived from the white noise simulations. This is evident from the lower panel of the plot, which shows the mean pseudo cross spectrum divided by the standard deviation in each k-bin (the power measurement in units of standard deviations), varying only up to 2 sigma. It is also supported by the two-dimensional spectra (we note that the range of cosmological scales in these 2D plots is not reduced to our main sensitivity coverage – the regions of high excess power arise after applying the total transfer function and are not included in the science analysis). Such outcome shows that we are, in fact, successfully suppressing the contributions from experimental systematics and correlated noise below the current level of white noise in the COMAP experiment.

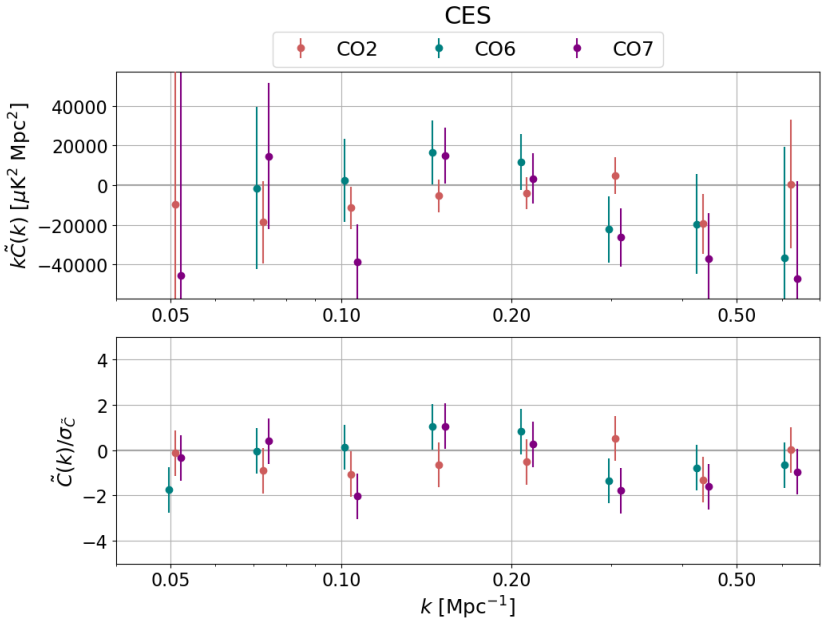

Figure 6.2: Spherically averaged mean pseudo cross spectra for the constant elevation scans (CES) of three science fields – CO2 (red), CO6 (blue), and CO7 (purple) – plotted with a slight k-offset (centered about the CO2 data points). The lower panel shows the spectrum estimate divided by its uncertainty in each k-bin (significance).

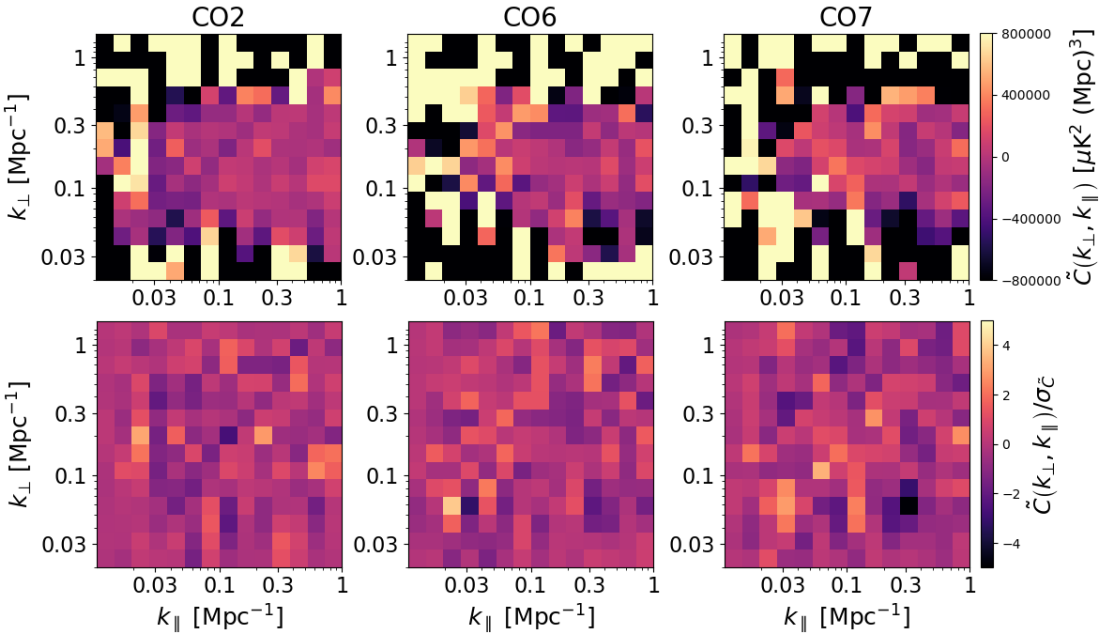

Figure 6.3: Mean pseudo cross spectra in the $k_\parallel - k_\perp$ plane for the constant elevation scans (CES) of three science fields – CO2 (left), CO6 (middle), and CO7 (right). The bottom row shows the spectrum estimate divided by its uncertainty.

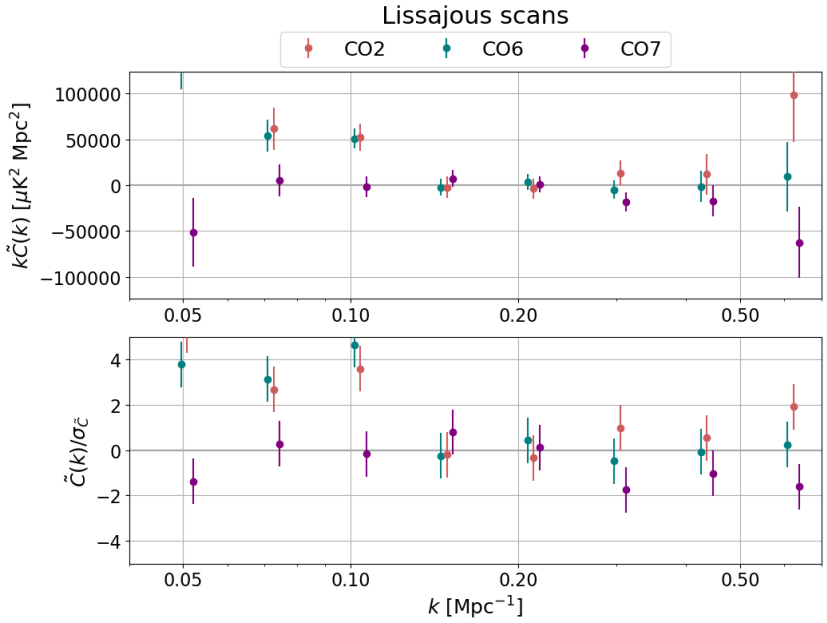

Figure 6.4: Spherically averaged mean pseudo cross spectra for the Lissajous scans of three science fields – CO2 (red), CO6 (blue), and CO7 (purple) – plotted with a slight k-offset (centered about the CO2 data points). The lower panel shows the spectrum estimate divided by its uncertainty in each k-bin (significance of the measurement).

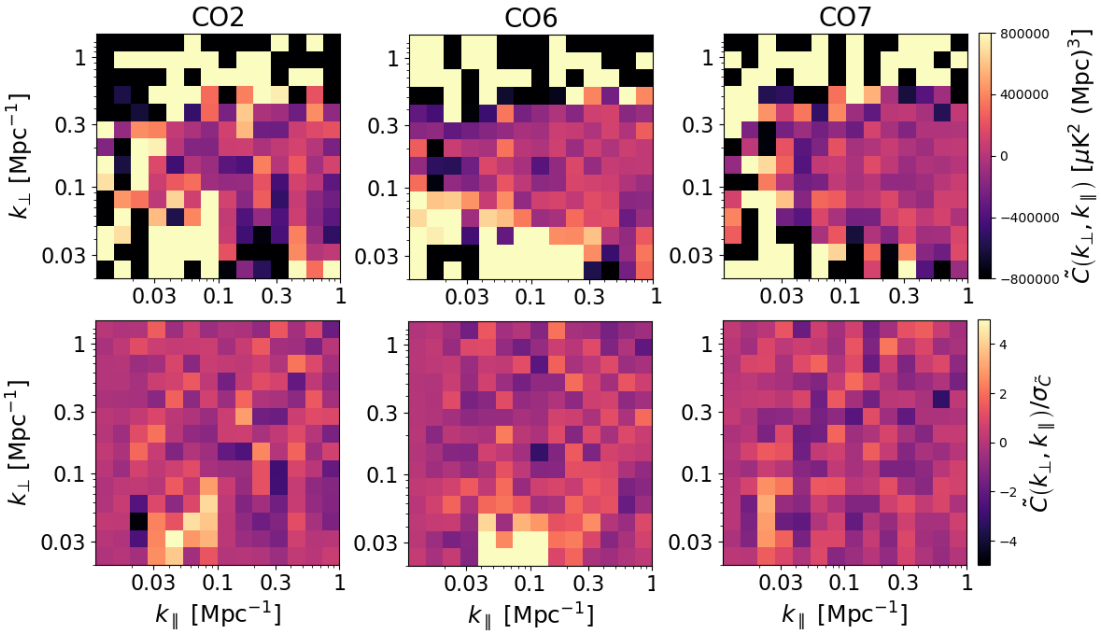

Figure 6.5: Mean pseudo cross spectra in the $k_\parallel - k_\perp$ plane for the Lissajous scans of three science fields – CO2 (left), CO6 (middle), and CO7 (right). The bottom row shows the spectrum estimate divided by its uncertainty.

The results associated with Lissajous scans are shown in Figure 6.4 (spherically averaged) and Figure 6.5 (in the $k_{\parallel} - k_{\perp}$ plane). We can see that these are not as well-behaved as the CES data. In the top panel of the spherically averaged plot, we notice clear signs of excess power at larger scales for CO2 and CO6 fields (it needs to be pointed out that the limits of y-axis are significantly larger here than for the corresponding CES plot). The lower panel of the figure – the significance plot – shows even 4 sigma deviations for CO6 and CO7 at $k \approx 0.05 - 01$ Mpc^{-1}. The corresponding effect is represented by the bright regions in the bottom row of 2D results in Figure 6.5, extending throughout the largest angular scales ($k_{\perp} < 0.1$ Mpc^{-1}) and $k_{\parallel} \approx 0.03 - 0.1$ Mpc^{-1}. However, the observations associated with the CO7 field appear to be an exemption.

These main results of the mean pseudo cross spectra continue the trend that we have seen during the analysis of χ^2 grids. The FPXS from constant elevation scans were mostly clean and resembled the white noise distribution quite well, whereas a higher fraction of the Lissajous data exceeded the maximum threshold of 5 sigma and had to be excluded from the final estimate. Nevertheless, even after applying this cut we still see some signs of excess power in the Lissajous results. They might arise due to previously discussed effects correlated with the pointing of the telescope (that changes more significantly for this type of scanning pattern), like varying power contributions from the atmosphere or from the beam sidelobes.

6.2 Null tests

An important application of the FPXS method is performing the null tests. At this point of the experiment, they can be conducted in order to provide some further verification of the consistency of the main results and unravel more information about the excess power seen in the Lissajous spectra. Again, we analyze the six considered data sets separately (CO2 CES, CO2 Lissajous, CO6 CES, CO6 Lissajous, CO7 CES, CO7 Lissajous). Each of them is additionally split in two according to various test variables and then the difference between these halves is computed. Maps that are the outcome of such subtraction are processed through all the stages of the FPXS method, exactly as the main results. We expect that this procedure will cancel out any common factors between the two disjoint map sets that have been subtracted from each other, leaving only random white noise, and the final spectra will be statistically consistent with zero (hence the name *null* tests). Any deviations from this prediction will pinpoint the systematic that is connected to the test variable used to derive the corresponding difference map.

In Figure 6.6, we show the spherically averaged mean pseudo cross spectra associated with six different types of difference maps, where we split data with respect to time of day (night data being closer to 2 AM), ambient temperature, wind speed, season (closer to winter or summer), half of the mission, and observation ID (even or odd number). We can see that most results are in agreement with our expectations and appear largely consistent with white noise. This is the case even for the Lissajous data, which exhibit clear signs of residual systematics in the main results. Such outcome of the null tests indicates that sources of excess power impact all the data, and the effect is therefore

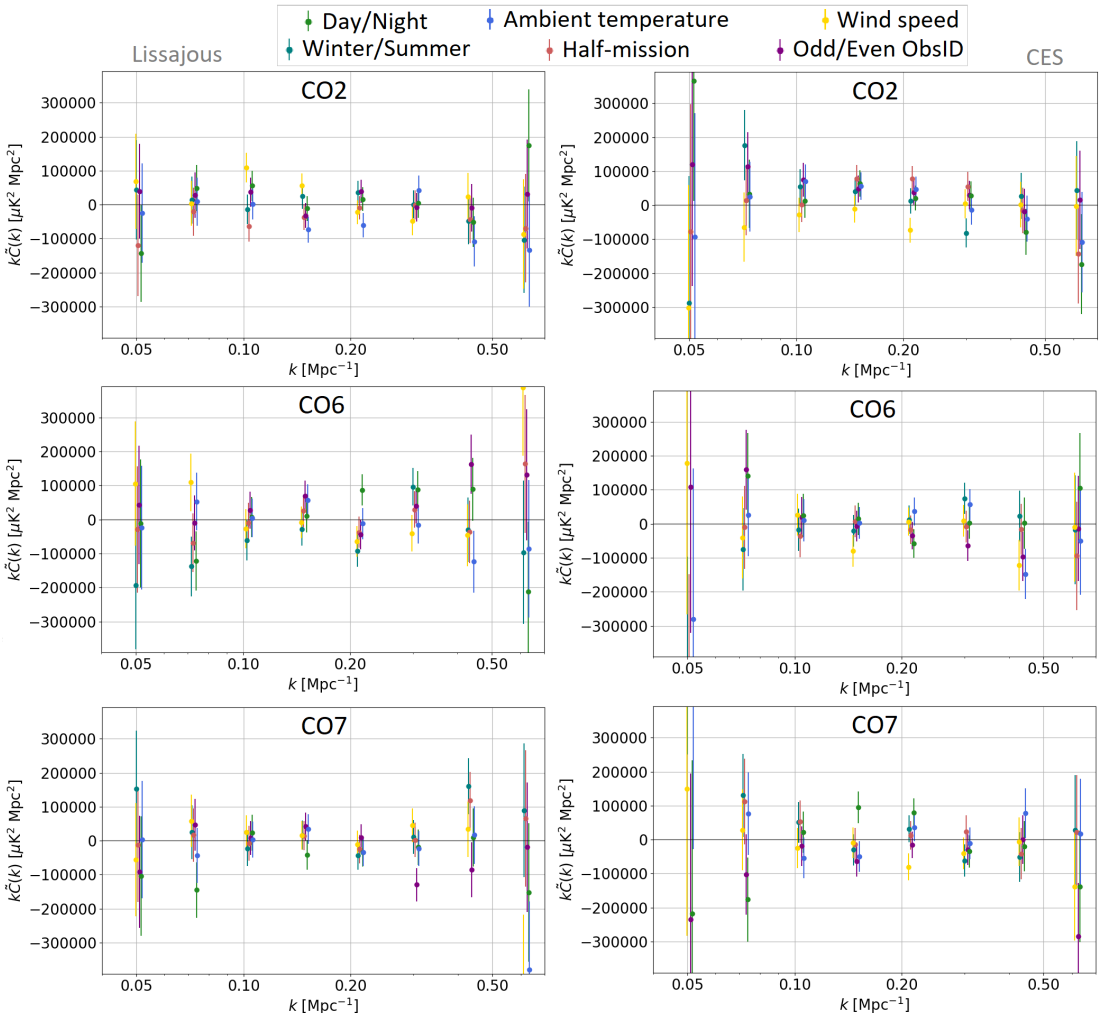

Figure 6.6: Spherically averaged mean pseudo cross spectra of the difference maps with data from Lissajous scans (left column) and constant elevation scans (right column), shown for all three science fields – CO2 (upper row), CO6 (middle row), and CO7 (bottom row). These mean spectra are plotted with a slight k-offset about the bin centers and are derived from the maps that represent the difference between data split according to test variables like time of day (green), ambient temperature (blue), wind speed (yellow), season (teal), half-mission (red), and ObsID number (purple).

canceled in all the difference maps as the common factor. The most problematic systematics might thus not be identified in this null test approach.

We select the split with respect to time of day as an example to be shown in two dimensions, included in Figure 6.7. Looking at the regions in the $k_{\parallel} - k_{\perp}$ plane where the COMAP experiment is most sensitive, we can see that these spectra support the results obtained for the spherically averaged case. We notice a slight positive bias for the CO2 CES data (present also in the 1D plot), but it corresponds to rather low significance.

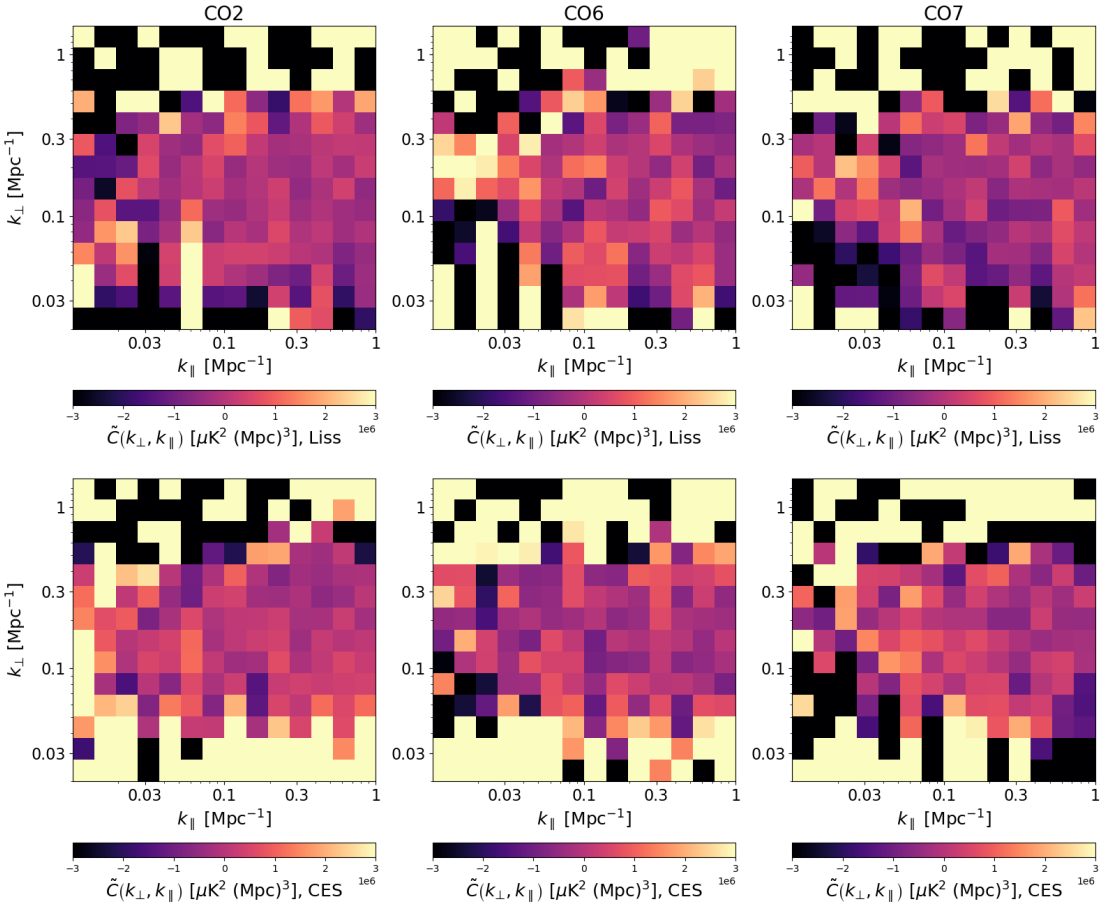

Figure 6.7: Mean pseudo cross spectra of the difference maps associated with day/night split, shown in the $k_\parallel - k_\perp$ plane. The results are obtained from Lissajous data (upper row) and constant elevation scans (bottom row), for three science fields – CO2 (left), CO6 (middle), and CO7 (right).

6.3 Inference from the data

At this point of the experiment (after one year of gathering observational data), the white noise fluctuations we see in the results associated with CES are anticipated. Such an outcome confirms that we are able to suppress the contributions from experimental systematics and correlated noise below the current magnitude of white noise. Because this component is random, we already see that it is integrating down with the accumulation of data, following the radiometer equation (Equation 3.4). However, since its level is still quite high (see the maps in Figure 3.14) compared to the CO line emission signal ($\sim$ few microkelvins), we need to wait for more data from observations, which will eventually increase our sensitivity to be good enough to claim a detection.

In this section, we will already show how to extract information about the amplitude of the CO signal employing our 1-year data set. We will combine the mean spectra from constant elevation scans, which performed best in the FPXS analysis, and use them to derive two types of estimates. Thereafter, we will discuss the current and projected future limits introduced by these data, and compare them to various models.

6.3.1 Signal amplitude estimation

Now, we will show the results associated with the signal amplitude estimates derived from the mean pseudo cross spectra. We will employ the data that appeared cleanest in the preceding analysis, that is constant elevation scans. The mean spectra from all the fields are combined using the inverse-variance noise weighting (analogously to Equation 4.23 and Equation 4.24). The resulting spectrum is presented in Figure 6.8, together with the significance of the measurement (lower panel). In addition, we plot the spectra associated with our fiducial model (described in Section 4.5.1), comparing the auto spectrum to the pseudo spectrum (obtained from noise-weighted maps), as well as to the pseudo spectrum computed from maps smoothed only in the line-of-sight direction (to account for the intrinsic CO line width), which is best suited to our observations.

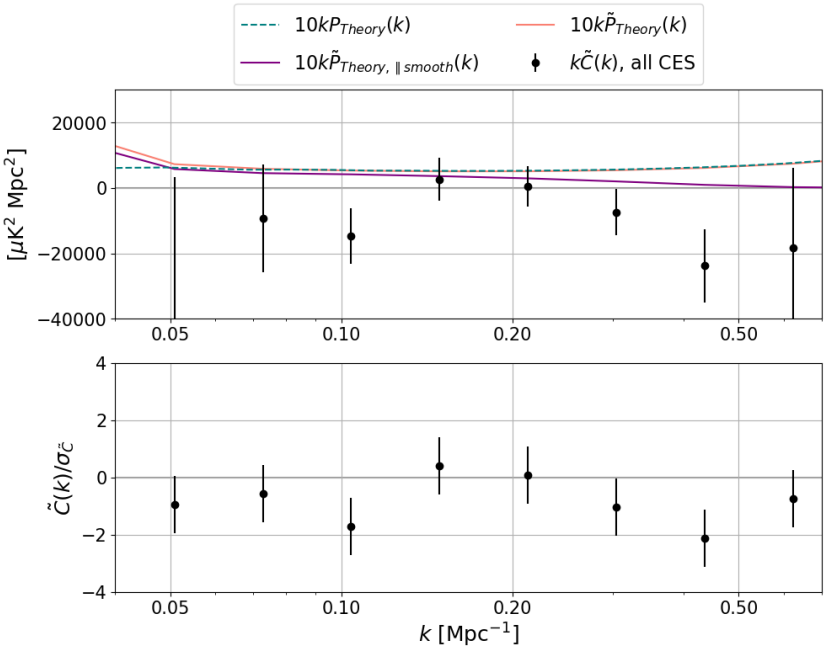

Figure 6.8: Mean pseudo cross spectrum associated with the combination of CES data from all three science fields. The lower panel shows the spectrum estimate divided by its uncertainty in each k-bin. We compare the data points to results derived from the maps generated based on our fiducial model – the auto spectrum (teal dashed curve), the pseudo spectrum (orange), and the pseudo spectrum of the maps smoothed in the line-of-sight direction to account for the effect of line broadening (purple).

We can see that the pseudo spectrum slightly deviates from the auto spectrum but almost exclusively on the largest scales. Furthermore, the pseudo spectrum associated with the smoothed maps is generally lower, which becomes very clear on small scales (attenuation caused by the line broadening). We notice that the data points in the middle region, where we have the highest sensitivity, are generally in agreement with the model within the corresponding error bars. There are two points that are slightly more negatively biased (at $k \approx 0.1$ Mpc^{-1} and $k \approx 0.4$ Mpc^{-1}).

The CES-combination is used to derive the estimates described in Section 4.6.2. We co-add data points over all k-bins within our highest sensitivity coverage to obtain the scale-independent A_1 estimate (Equation 4.42) and perform a similar procedure, dividing by the theory spectrum, $\widetilde{P}_{\mathrm{Theory},\parallel\,\mathrm{smooth}}(k)$, to compute the model-dependent A_2 (Equation 4.45). The resulting values are $A_1 = -26366 \pm 13799$ μK^{2}Mpc^3 and $A_2 = -12.8 \pm 10.3$, as presented in Figure 6.9 (where we mark only the data points that are included in the estimation). Since some points are slightly negatively biased, so is the outcome of this fitting process. At the current stage of the experiment this is somewhat dependent on the data sets we choose (generally, the more data sets we combine, the lower uncertainty we get). Overall, our amplitude fits remain statistically consistent with zero.

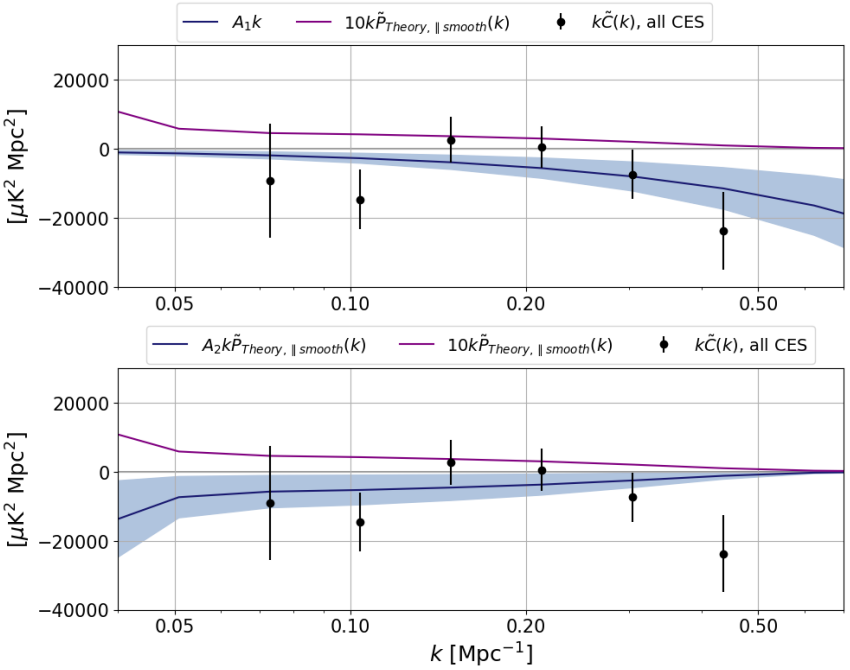

Figure 6.9: Results of the CO signal amplitude estimation, derived from the combination of mean pseudo cross spectra corresponding to CES data from all three science fields (black dots). We compare the outcomes, $A_1 = -26366 \pm 13799$ μK^{2}Mpc^3 (upper panel, blue) and $A_2 = -12.8 \pm 10.3$ (lower panel, blue), to the pseudo spectrum computed based on our fiducial model (purple).

6.3.2 Comparison with models and future expectations

Finally, we will discuss the modeling constraints that can at this point be inferred from the data (after 1 year of observing the sky), as well as the projected forecasts associated with 4 more years of observations. In this analysis, we will use our cleanest data set, corresponding to the CES combination. In Figure 6.10, we compare our measurement and fiducial model (UM+COLDz, which stands for priors based on the modeling from the UniverseMachine [64] and constraints from the COLDz galaxy survey, as explained in Section 4.5.1) to some other theoretical predictions, which employ different priors and observational constraints. This includes the model of H. Padmanabhan [68] (using constraints from COLDz, COPSS, and galaxy observations), Pullen et al. [69], and previously mentioned Li et al. [42]. We also plot the measurement from COPSS [70], as well as the best-fit shot noise power spectrum and upper limit on the clustering component of the spectrum derived from the COPSS and mmIME experiments [71].

In the left panel of the figure, we can see that our current upper limit already rules out two of the most optimistic models at 95% confidence. With data from further years of observations, we predict a total signal-to-noise (summed over all k-bins, as in Equation 4.40) of 2–8 sigma for our fiducial model. We have mentioned the possibility of cross-correlation with the HETDEX galaxy survey, which would additionally increase the significance of such detection. The forecast we discuss is based on the current sensitivity of the experiment, as well as some improvements to be introduced to the pipeline and the observing strategy (like more precise beam and ground modeling, including all the feeds in the analysis, or favoring CES over Lissajous scanning strategy).

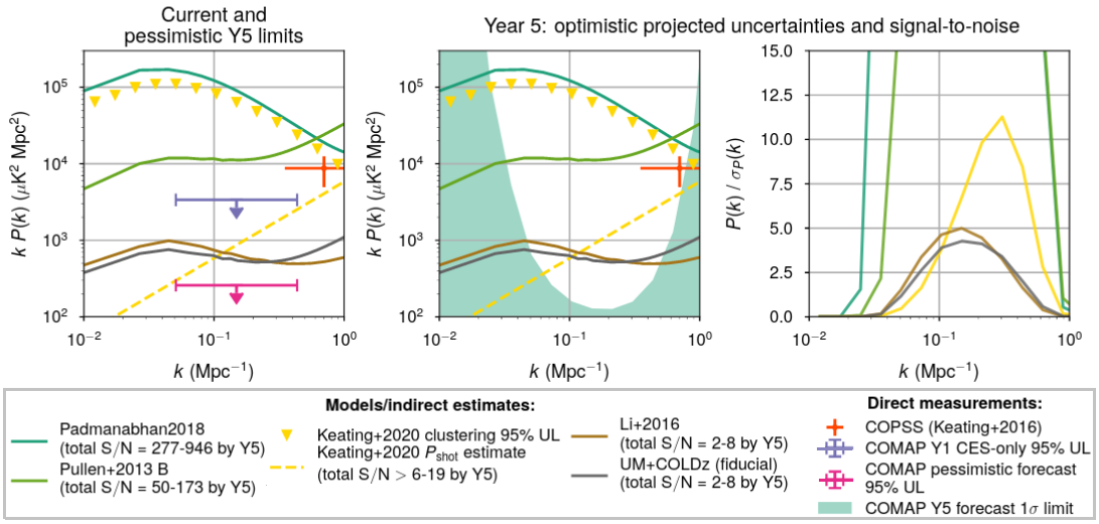

Figure 6.10: Constraints from the current CES data set compared to other measurements and theoretical predictions (left panel). We also show the forecast for results obtained after 5 years of observations (middle panel), along with the signal-to-noise predictions (right panel). Credit: D. Chung.

Chapter 7

Conclusion and Outlook

The summary of conducted work and future prospects

In this thesis, we have presented the low-level COMAP data analysis pipeline, producing filtered and calibrated temperature sky maps, and developed an efficient way of performing the high-level analysis, extracting the signal pseudo power spectrum from these three-dimensional maps. We have also estimated the impact of various effects modifying the signal measurement, conducted null tests, and compared the information inferred from the first-year data set to theoretical predictions from signal modeling.

7.1 Conclusion

The Feed-feed Pseudo CROSS Spectrum (FPXS) method has been devised to provide a robust way of extracting the signal spectrum from the intensity maps. The main advantages of our design are three-fold. First of all, by using cleverly chosen split variables, we are able to strongly suppress signal contributions from several sources of residual systematic errors that are currently critical, including the ground contamination and standing waves. Secondly, employing the cross spectrum instead of the auto spectrum reduces the susceptibility to possible noise modeling errors, because any misestimation impacts only the uncertainty of the signal measurement, not the signal estimate itself. Lastly, by splitting data into more independent maps and computing the average spectrum of all combinations of them, we increase the sensitivity of our measurement compared to a single data-split (which is a minimum requirement for cross-correlation).

In order to obtain an unbiased estimate of the signal pseudo spectrum, we have also analyzed the impact of various effects suppressing the signal measured by the detectors (using the simulations based on our fiducial signal model) and introduced appropriate corrections in this regard. We have seen that the limited angular resolution due to the (simplified) form of the instrumental beam attenuates the measured signal at small angular scales (especially affecting $k_\perp \gtrsim 0.3$ Mpc^{-1}). We have also studied the consequences of our choice of the spectral resolution of the final maps, showing its impact on the smallest scales in the line-of-sight dimension (mostly on $k_\parallel \gtrsim 0.4$ Mpc^{-1}). Moreover,

we have seen that the procedures applied during the low-level data processing suppress the signal on large scales in both directions ($k_{\parallel}, k_{\perp} \lesssim 0.05$ Mpc^{-1}), and that this effect is different depending on the type of scanning strategy. The combination of insights provided by this research resulted in the total transfer function, limiting the overall sensitivity of the COMAP experiment to spherically averaged $k \approx 0.05 - 0.5$ Mpc^{-1} (the clustering component of the power spectrum).

The results derived using the FPXS method have shown that the CES data are largely consistent with white noise after the first year of observations and that we are able to effectively suppress the contributions from various systematics for this type of scan. Already at the current stage of the experiment, our cleanest data (combination of CES from all three science fields) provide one of the strongest constraints from CO intensity mapping, with an upper limit excluding two of the considered signal models at 95% confidence. However, the Lissajous data exhibit some clear signs of excess power and will thus require a more sophisticated treatment in the future, especially when it comes to the effects correlated with the pointing of the telescope (like the ground pickup and the atmospheric contributions).

7.2 The outlook on future work

Throughout the discussion of our results, we have already highlighted some points with room for improvement. Firstly, during the analysis of the instrumental beam transfer function, we have adopted a simplified beam model, assuming that all the sky power is contained within the main beam (beam efficiency equal to one). However, nearly 30% of the power enters the instrument through sidelobes. This effect needs to be taken into account, implementing a more realistic model of the beam pattern, which will indicate a further attenuation of the measured signal (the corresponding transfer function will be lower). Secondly, our estimate (the pseudo cross spectrum) is currently biased by the mode mixing effect. We have assessed that its impact is not very severe over the range of cosmological scales where we have the highest sensitivity ($\sim 5 - 25\%$), but it will be essential to undo this bias for the precise science analysis in the future.

In the wider perspective, it is important to consider the lessons learned from the analysis of the first year of observational data. Some major takeaways are associated with increasing the observing efficiency, which currently is $\sim 10\%$ due to quite conservative cuts that had to be introduced. Henceforth, the observations will be conducted only at elevations between 35° and 65° (reducing the ground contamination), all the 19 feeds will be operational, and we will favor the CES over the Lissajous scanning strategy, which turned out to be more prone to residual systematics. On the data analysis side, we are working on the ground modeling, an upgraded frequency filter, as well as implementing a baseline destriper into the mapmaker (now we are using a simple binned mapmaker), which will maximize the associated transfer function. Integrating these actions into COMAP operations will optimistically increase the future observing efficiency to $\sim 37\%$ [50]. This will directly impact the results seen in our high-level FPXS analysis, significantly improving the sensitivity of the obtained signal measurement.

COMAP Pathfinder is currently underway a 2-year campaign, which is about to end in August 2021. Taking into account all the aforementioned improvements, we expect that the additional 3 years of gathering observational data will yield a total detection significance of 8 sigma for our fiducial model. Such a detection will pinpoint the clustering component of the CO power spectrum at $z \sim 3$ and characterize the properties of galaxies at the Epoch of Galaxy Assembly. In the upcoming phase of the experiment, we plan to introduce an extra receiver at a lower frequency band, which will be sensitive to the CO(1-0) signal from the Epoch of Reionization. A cross-correlation of these observations with data from the ongoing survey, which, in addition to the main CO(1-0) signal from $z \sim 3$, also covers a fainter CO(2-1) contribution from the Epoch of Reionization ($z \sim 7$), will provide an invaluable insight into this under-explored period in cosmic history. The plans for a more distant future include a further array expansion (adding more dishes and detector chains to the science analysis) and possibly a CO intensity mapping satellite, which will enable studying the structure of huge volumes of the observable Universe.

Techniques of line intensity mapping are still under development and the field is only emerging compared to more mature complementary methods, like galaxy surveys or CMB experiments. Nevertheless, we have seen its rapid development in recent years, with projects like COMAP and a variety of other experiments targeting different spectral lines and redshifts. The line intensity mapping has many crucial scientific advantages and a potential to bring us one step further towards understanding the mysteries of the Universe.

Bibliography

[1] ESA. A history of astrometry, 2019. https://sci.esa.int/web/gaia/-/53196-the-oldest-sky-maps. Accessed: 22 February 2021.

[2] Robert Millikan. *Evolution in Science and Religion, The Terry Lectures for 1927.* Yale University Press, 1927.

[3] Carlos Martins. *The Universe Today. Our Current Understanding and How It Was Achieved.* Springer, 2020.

[4] Kenneth R Lang. *A Brief History of Astronomy and Astrophysics.* World Scientific, 2018.

[5] Tony Phillips. Einstein's Eclipse, 2021. https://spaceweatherarchive.com/2021/03/22/einsteins-eclipse/?fbclid=IwAR13Yn_OJa8OpRGJ1pS1M6LbY-M_je-cp80IECqFVAL9w-oWaVnmZrPQDQU. Accessed: 27 March 2021.

[6] Albert Einstein. *Cosmological Considerations of the General Theory of Relativity.* Königlich Preußische Akademie der Wissenschaften (Berlin). Sitzungsberichte (1917): 142-152. English translation in: *The Collected Papers of Albert Einstein*, Vol. 6: The Berlin years/ Writings 1914-1917. https://einsteinpapers.press.princeton.edu/vol6-trans/433. Accessed: 30 May 2021.

[7] Øyvind Grøn and Øystein Elgarøy. Is space expanding in the Friedmann universe models? *American Journal of Physics*, 75(2):151–157, Feb 2007. arXiv: 0603162 [astro-ph].

[8] Georges Lemaître. The Beginning of the World From the Point of View of Quantum Theory. *Nature*, 127/3210:706, 1931.

[9] Ralph A. Alpher and Robert C. Herman. Evolution of the Universe. *Nature*, 162:774–775, 1948.

[10] George F. Smoot. COBE observations and results. *Conference on 3K cosmology*, 1999. arXiv: 9902027 [astro-ph].

[11] ESA. The history of the Universe, 2015. http://www.esa.int/ESA_Multimedia/Images/2015/02/The_history_of_the_Universe. Accessed: 28 February 2021.

[12] Oliver Piattella. Lecture Notes in Cosmology. *UNITEXT for Physics*, 2018. arXiv: 1803.00070 [astro-ph.CO].

[13] Peter Schneider. *Extragalactic Astronomy and Cosmology, An Introduction.* Springer, 2006.

[14] Scott Dodelson. *Modern Cosmology.* Academic Press, 2003.

[15] NASA. What is the Inflation Theory?, 2010. `https://wmap.gsfc.nasa.gov/universe/bb_cosmo_infl.html`. Accessed: 31 May 2021.

[16] David H. Lyth. *The History of the Universe.* Springer, 2016.

[17] J. Miralda-Escude. The Dark Age of the Universe. *Science*, 300(5627):1904–1909, Jun 2003. arXiv: 0307396 [astro-ph].

[18] NASA, ESA, Lavochkin Association, HESS Collaboration, Salt Foundation, Rick Peterson/WMKO, Germini Observatory/AURA, CARMA team, and NRAO/AUI. Observatories Across the Electromagnetic Spectrum, 2013. `https://imagine.gsfc.nasa.gov/science/toolbox/emspectrum_observatories1.html`. Accessed: 08 March 2021.

[19] Paula Chadwick. Mapping the gamma-ray sky. *Astronomy and Geophysics*, 46/6, 2005.

[20] Ely D. Kovetz, Patrick C. Breysse, Adam Lidz, Jamie Bock, Charles M. Bradford, Tzu-Ching Chang, Simon Foreman, Hamsa Padmanabhan, Anthony Pullen, Dominik Riechers, Marta B. Silva, and Eric Switzer. Astro2020 Science White Paper: Astrophysics and Cosmology with Line-Intensity Mapping, 2019. arXiv: 1903.04496 [astro-ph.CO].

[21] Matthew Colless and the 2dFGRS Team. The 2dF Galaxy Redshift Survey, 2003. `http://www.2dfgrs.net/`. Accessed: 6 March 2021.

[22] Donnacha Kirk, Ofer Lahav, Sarah Bridle, Stephanie Jouvel, Filipe B. Abdalla, and Joshua A. Frieman. Optimizing spectroscopic and photometric galaxy surveys: same-sky benefits for dark energy and modified gravity. *Monthly Notices of the Royal Astronomical Society*, 451(4):4424–4444, Jul 2015. arXiv: 1307.8062 [astro-ph.CO].

[23] Alberto Fernandez-Soto, Kenneth M. Lanzetta, Hsiao-Wen Chen, Sebastian M. Pascarelle, and Noriaki Yahata. On the compared accuracy and reliability of spectroscopic and photometric redshift measurements. *The Astrophysical Journal Supplement Series*, 135(1):41–61, Jul 2001. arXiv: 0007447 [astro-ph].

[24] Ruth Durrer. The cosmic microwave background: the history of its experimental investigation and its significance for cosmology. *Classical and Quantum Gravity*, 32(12):124007, Jun 2015. arXiv: 1506.01907 [astro-ph.CO].

[25] NASA, JPL-Caltech, and ESA. Cosmic Microwave Background (CMB), 2013. https://lambda.gsfc.nasa.gov/education/graphic_history/microwaves.cfm. Accessed: 28 February 2021.

[26] NASA. Cosmic Background Explorer, 2008. https://lambda.gsfc.nasa.gov/product/cobe/. Accessed: 10 March 2021.

[27] NASA. Wilkinson Microwave Anisotropy probe, 2017. https://map.gsfc.nasa.gov/. Accessed: 13 March 2021.

[28] Planck Collaboration: Aghanim, N., Akrami, Y., Arroja, F., Ashdown, M., Aumont, J., Baccigalupi, C., Ballardini, M., Banday, A. J., Barreiro, R. B., Bartolo, N., Basak, S., Battye, R., Benabed, K., Bernard, J.-P., Bersanelli, M., Bielewicz, P., Bock, J. J., Bond, J. R., Borrill, J., Bouchet, F. R., Boulanger, F., Bucher, M., Burigana, C., Butler, R. C., Calabrese, E., Cardoso, J.-F., Carron, J., Casaponsa, B., Challinor, A., Chiang, H. C., Colombo, L. P. L., Combet, C., Contreras, D., Crill, B. P., Cuttaia, F., de Bernardis, P., de Zotti, G., Delabrouille, J., Delouis, J.-M., Désert, F.-X., Di Valentino, E., Dickinson, C., Diego, J. M., Donzelli, S., Doré, O., Douspis, M., Ducout, A., Dupac, X., Efstathiou, G., Elsner, F., Enßlin, T. A., Eriksen, H. K., Falgarone, E., Fantaye, Y., Fergusson, J., Fernandez-Cobos, R., Finelli, F., Forastieri, F., Frailis, M., Franceschi, E., Frolov, A., Galeotta, S., Galli, S., Ganga, K., Génova-Santos, R. T., Gerbino, M., Ghosh, T., González-Nuevo, J., Górski, K. M., Gratton, S., Gruppuso, A., Gudmundsson, J. E., Hamann, J., Handley, W., Hansen, F. K., Helou, G., Herranz, D., Hildebrandt, S. R., Hivon, E., Huang, Z., Jaffe, A. H., Jones, W. C., Karakci, A., Keihänen, E., Keskitalo, R., Kiiveri, K., Kim, J., Kisner, T. S., Knox, L., Krachmalnicoff, N., Kunz, M., Kurki-Suonio, H., Lagache, G., Lamarre, J.-M., Langer, M., Lasenby, A., Lattanzi, M., Lawrence, C. R., Le Jeune, M., Leahy, J. P., Lesgourgues, J., Levrier, F., Lewis, A., Liguori, M., Lilje, P. B., Lilley, M., Lindholm, V., López-Caniego, M., Lubin, P. M., Ma, Y.-Z., Macías-Pérez, J. F., Maggio, G., Maino, D., Mandolesi, N., Mangilli, A., Marcos-Caballero, A., Maris, M., Martin, P. G., Martinelli, M., Martínez-González, E., Matarrese, S., Mauri, N., McEwen, J. D., Meerburg, P. D., Meinhold, P. R., Melchiorri, A., Mennella, A., Migliaccio, M., Millea, M., Mitra, S., Miville-Deschênes, M.-A., Molinari, D., Moneti, A., Montier, L., Morgante, G., Moss, A., Mottet, S., Münchmeyer, M., Natoli, P., Nørgaard-Nielsen, H. U., Oxborrow, C. A., Pagano, L., Paoletti, D., Partridge, B., Patanchon, G., Pearson, T. J., Peel, M., Peiris, H. V., Perrotta, F., Pettorino, V., Piacentini, F., Polastri, L., Polenta, G., Puget, J.-L., Rachen, J. P., Reinecke, M., Remazeilles, M., Renault, C., Renzi, A., Rocha, G., Rosset, C., Roudier, G., Rubiño-Martín, J. A., Ruiz-Granados, B., Salvati, L., Sandri, M., Savelainen, M., Scott, D., Shellard, E. P. S., Shiraishi, M., Sirignano, C., Sirri, G., Spencer, L. D., Sunyaev, R., Suur-Uski, A.-S., Tauber, J. A., Tavagnacco, D., Tenti, M., Terenzi, L., Toffolatti, L., Tomasi, M., Trombetti, T., Valiviita, J., Van Tent, B., Vibert, L., Vielva, P., Villa, F., Vittorio, N., Wandelt, B. D., Wehus, I. K., White, M., White, S. D. M., Zacchei,

A., and Zonca, A. Planck 2018 results - I. Overview and the cosmological legacy of Planck. *A&A*, 641:A1, 2020. arXiv: 1807.06205 [astro-ph.CO].

[29] LIGO Collaboration and Virgo Collaboration. Observation of Gravitational Waves from a Binary Black Hole Merger. *Physical Review Letters*, 116(6), Feb 2016. arXiv: 1602.03837 [gr-qc].

[30] Andrzej Królak and Mandar Patil. The First Detection of Gravitational Waves. *Universe*, 3(3):59, Jul 2017. arXiv: 1708.00918 [gr-qc].

[31] Jack Kwok, King Lau, Edward Young, and Kenneth Young. What is the B mode in CMB polarization?, 2019. arXiv: 1911.12488 [gr-qc].

[32] Marc Kamionkowski and Ely D. Kovetz. The Quest for B Modes from Inflationary Gravitational Waves. *Annual Review of Astronomy and Astrophysics*, 54(1):227–269, 2016. arXiv: 1510.06042 [astro-ph.CO].

[33] Alexey Boyarsky, Steen Hannestad, Marek Kowalski, Julien Lesgourgues, Luis Labarga, Susanne Mertens, and Mikhail Shaposhnikov. Nautrinos and the Universe. *Neutrino Town Meeting - Panel*, 2018.

[34] IceCube Collaboration. IceCube - Science (Research Highlights and Detector Construction). `https://icecube.wisc.edu/science`. Accessed: 20 March 2021.

[35] Fermi National Accelerator Laboratory. All Things Neutrino. `https://neutrinos.fnal.gov`. Accessed: 20 March 2021.

[36] Péter Mészáros, Derek B. Fox, Chad Hanna, and Kohta Murase. Multi-messenger astrophysics. *Nature Reviews Physics*, 1(10):585–599, Oct 2019. arXiv: 1906.10212 [astro-ph.HE].

[37] Stephen Cass. The IceCube Neutrino Detector at the South Pole Hits Paydirt, 2018. `https://spectrum.ieee.org/tech-talk/aerospace/astrophysics/the-icecube-neutrino-detector-at-the-south-pole-hits-paydirt`. Accessed: 27 March 2021.

[38] S. Noll, D. Burgarella, E. Giovannoli, V. Buat, D. Marcillac, and J. C. Muñoz-Mateos. Analysis of galaxy spectral energy distributions from far-UV to far-IR with CIGALE: studying a SINGS test sample. *Astronomy Astrophysics*, 507(3):1793–1813, Sep 2009. arXiv: 0909.5439 [astro-ph.CO].

[39] Karen Olsen. *Observing and Simulating Galaxy Evolution – from X-ray to millimeter wavelengths*. PhD thesis, University of Copenhagen, 2015.

[40] José Fonseca, Marta B. Silva, Mário G. Santos, and Asantha Cooray. Cosmology with intensity mapping techniques using atomic and molecular lines. *Monthly Notices of the Royal Astronomical Society*, 464(2):1948–1965, Sep 2016. arXiv: 1607.05288 [astro-ph.CO].

[41] Ely D. Kovetz, Marco P. Viero, Adam Lidz, Laura Newburgh, Mubdi Rahman, Eric Switzer, Marc Kamionkowski, James Aguirre, Marcelo Alvarez, James Bock, J. Richard Bond, Goeffry Bower, C. Matt Bradford, Patrick C. Breysse, Philip Bull, Tzu-Ching Chang, Yun-Ting Cheng, Dongwoo Chung, Kieran Cleary, Asantha Corray, Abigail Crites, Rupert Croft, Olivier Doré, Michael Eastwood, Andrea Ferrara, José Fonseca, Daniel Jacobs, Garrett K. Keating, Guilaine Lagache, Gunjan Lakhlani, Adrian Liu, Kavilan Moodley, Norm Murray, Aurélie Pénin, Gergö Popping, Anthony Pullen, Dominik Reichers, Shun Saito, Ben Saliwanchik, Mario Santos, Rachel Somerville, Gordon Stacey, George Stein, Francesco Villaescusa-Navarro, Eli Visbal, Amanda Weltman, Laura Wolz, and Micheal Zemcov. Line-intensity mapping: 2017 status report, 2017. arXiv: 1709.09066 [astro-ph.CO].

[42] Tony Y. Li, Risa H. Wechsler, Kiruthika Devaraj, and Sarah E. Church. Connecting CO Intensity Mapping to Molecular Gas and Star Formation in the Epoch of Galaxy Assembly. *The Astrophysical Journal*, 817(2):169, Jan 2016. arXiv: 1503.08833 [astro-ph.CO].

[43] James J. Condon and Scott M. Ransom. *Essential Radio Astronomy*. Princeton University Press, 2016.

[44] Martin Harwit. *Astrophysical Concepts*. Springer, 2006.

[45] Christopher Hirata. Notes on Atomic Structure, 2011. `http://www.tapir.caltech.edu/~chirata/ay102/Atomic.pdf`. Accessed: 5 April 2021.

[46] Patrick C. Breysse, Ely D. Kovetz, Peter S. Behroozi, Liang Dai, and Marc Kamionkowski. Insights from probability distribution functions of intensity maps. *Monthly Notices of the Royal Astronomical Society*, Jan 2017. arXiv: 1609.01728 [astro-ph.CO].

[47] Håvard Tveit Ihle. *Bayesian Data Analaysis for Intensity Mapping and CMB Experiments*. PhD thesis, University of Oslo, 2021.

[48] H. T. Ihle, D. Chung, G. Stein, M. Alvarez, J. R. Bond, P. C. Breysse, K. A. Cleary, H. K. Eriksen, M. K. Foss, J. O. Gundersen, S. Harper, N. Murray, H. Padmanabhan, M. P. Viero, and I. K. Wehus. Joint Power Spectrum and Voxel Intensity Distribution Forecast on the CO Luminosity Function with COMAP. *The Astrophysical Journal*, 871(1):75, Jan 2019. arXiv: 1808.07487 [astro-ph.CO].

[49] The COMAP Collaboration. CO Mapping Array Pathfinder (COMAP) Wiki, 2021. `https://sites.astro.caltech.edu/CRAL1-wiki/index.php/Main_Page`. Accessed: 10 April 2021.

[50] Marie K. Foss, Håvard T. Ihle, Jowita Borowska, Morgan Catha, Kieran A. Cleary, Hans Kristian Eriksen, Stuart Harper, James W. Lamb, Jonas G. S. Lunde, Nils-Ole Stutzer, Duncan J. Watts, Ingunn K. Wehus, David P. Woody, and The COMAP Collaboration. First Season COMAP Results: CO Data Processing, 2021. To be submitted.

[51] Maren Rasmussen. Data Selection for intensity mapping experiments using machine learning. Master's thesis, University of Oslo, 2020.

[52] Erik Alexander Levén. Line-Intensity Mapping with COMAP. Master's thesis, University of Oslo, 2019.

[53] Sebastian Kiehlmann. The History of OVRO, 2018. `https://www.ovro.caltech.edu/index.php?page=history`. Accessed: 12 April 2021.

[54] V. Zúñiga, N. Haridas, A. Erdogan, and T. Arslan. Effect of a Central Antenna Element on the Directivity, Half-Power Beamwidth and Side-Lobe Level of Circular Antenna Arrays. *2009 NASA/ESA Conference on Adaptive Hardware and Systems*, pages 252–256, 2009.

[55] Robert B. Leighton. A 10-Meter Telescope for Millimeter and Sub-Millimeter Astronomy, 1977. `https://authors.library.caltech.edu/35046/1/Leighton_Robert-AST_73-04908.pdf`. Accessed: 12 April 2021.

[56] Jacob W. M. Baars and Hans J. Kärcher. *Radio Telescope Reflectors. Historical Development of Design and Construction.* Springer, 2018.

[57] Dongwoo T. Chung, Marco P. Viero, Sarah E. Church, Risa H. Wechsler, Marcelo A. Alvarez, J. Richard Bond, Patrick C. Breysse, Kieran A. Cleary, Hans K. Eriksen, Marie K. Foss, Joshua O. Gundersen, Stuart E. Harper, Håvard T. Ihle, Laura C. Keating, Norman Murray, Hamsa Padmanabhan, George F. Stein, and Ingunn K. Wehus. Cross-correlating Carbon Monoxide Line-intensity Maps with Spectroscopic and Photometric Galaxy Surveys. *The Astrophysical Journal*, 872(2):186, Feb 2019. arXiv: 1809.04550 [astro-ph.GA].

[58] Stuart Harper. COMAP Scan Strategies II, June 2018. `https://sites.astro.caltech.edu/CRAL1-wiki/images/5/58/Scan_strategies_II.pdf`. Accessed: 30 May 2021.

[59] Stuart Harper, Clive Dickinson, and Thomas Rennie. COMAP Astronomical Calibration, March 2021. `https://sites.astro.caltech.edu/CRAL1-wiki/images/9/92/Comap_cal.pdf`. Accessed: 30 May 2021.

[60] Håvard T. Ihle, Jowita Borowska, Nils-Ole Stutzer, and The COMAP Collaboration. First Season COMAP Results: Power spectrum methodology and preliminary data quality assessment, 2021. To be submitted.

[61] David W. Hogg. Distance measures in cosmology, 1999. `https://cds.cern.ch/record/387177/files/9905116.pdf`. Accessed: 26 April 2021.

[62] Dongwoo T. Chung, Patrick C. Breysse, Kieran Cleary, Håvard Tveit Ihle, Hamsa Padmanabhan, and Marta B. Silva. Early Science Results from the CO Mapping Array Project Pathfinder: V. CO Emission Models at z $\sim$ 3. To be submitted.

[63] Dongwoo T. Chung, Patrick C. Breysse, Håvard Tveit Ihle, Hamsa Padmanabhan, Marta B. Silva, J. Richard Bond, Jowita Borowska, Kieran A. Cleary, Hans Kristian Eriksen, Marie Kristine Foss, Joshua Ott Gundersen, Laura C. Keating, Jonas Gahr Sturtzel Lunde, Nils-Ole Stutzer, Marco P. Viero, Duncan J. Watts, and Ingunn Kathrine Wehus. A model of spectral line broadening in signal forecasts for line-intensity mapping experiments, 2021. arXiv: 2104.11171[astro-ph.CO].

[64] Peter Behroozi, Risa H Wechsler, Andrew P Hearin, and Charlie Conroy. UniverseMachine: The correlation between galaxy growth and dark matter halo assembly from z = 0-10. *Monthly Notices of the Royal Astronomical Society*, 488(3):3143–3194, May 2019. arXiv: 1806.07893 [astro-ph.GA].

[65] Dongwoo T. Chung. A Partial Inventory of Observational Anisotropies in Single-dish Line-intensity Mapping. *The Astrophysical Journal*, 881(2):149, Aug 2019. arXiv: 1905.00209 [astro-ph.CO].

[66] Yun-Ting Cheng, Tzu-Ching Chang, James Bock, C. Matt Bradford, and Asantha Cooray. Spectral line de-confusion in an intensity mapping survey. *The Astrophysical Journal*, 832(2):165, Nov 2016. arXiv: 1604.07833 [astro-ph.CO].

[67] Eric Hivon, Krzysztof M. Górski, C. Barth Netterfield, Brendan P. Crill, Simon Prunet, and Frode Hansen. MASTER of the Cosmic Microwave Background Anisotropy Power Spectrum: A Fast Method for Statistical Analysis of Large and Complex Cosmic Microwave Background Data Sets. *The Astrophysical Journal*, 567(1):2–17, Mar 2002. arXiv: 0105302 [astro-ph].

[68] Hamsa Padmanabhan. Constraining the CO intensity mapping power spectrum at intermediate redshifts. *Monthly Notices of the Royal Astronomical Society*, 475(2):1477–1484, Dec 2017. arXiv: 1706.01471 [astro-ph.GA].

[69] Anthony R. Pullen, Tzu-Ching Chang, Olivier Doré, and Adam Lidz. Cross-correlations as a cosmological carbon monoxide detector. *The Astrophysical Journal*, 768(1):15, Apr 2013. arXiv: 1211.1397 [astro-ph.CO].

[70] Garrett K. Keating, Daniel P. Marrone, Geoffrey C. Bower, Erik Leitch, John E. Carlstrom, and David R. DeBoer. COPSS ii: The Molecular Gas Content of Ten Million Cubic Megaparsecs at $z \sim 3$. *The Astrophysical Journal*, 830(1):34, Oct 2016. arXiv: 1605.03971 [astro-ph.GA].

[71] Garrett K. Keating, Daniel P. Marrone, Geoffrey C. Bower, and Ryan P. Keenan. An Intensity Mapping Detection of Aggregate CO Line Emission at 3 mm. *The Astrophysical Journal*, 901(2):141, Oct 2020. arXiv: 2008.08087 [astro-ph.GA].